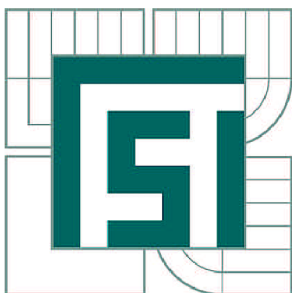# VYSOKÉ UČENÍ TECHNICKÉ V BRNĚ

BRNO UNIVERSITY OF TECHNOLOGY

FAKULTA STROJNÍHO INŽENÝRSTVÍ
ÚSTAV MATERIÁLOVÝCH VĚD A INŽENÝRSTVÍ

FACULTY OF MECHANICAL ENGINEERING
INSTITUTE OF MATERIALS SCIENCE AND ENGINEERING

EARLY STAGES OF FATIGUE DAMAGE OF STEELS FOR FUSION ENERGETICS

POČÁTEČNÍ STADIA ÚNAVOVÉHO POŠKOZENÍ U OCELÍ PRO FÚZNÍ ENERGETIKU

DIZERTAČNÍ PRÁCE
DOCTORAL THESIS

AUTOR PRÁCE   Ing. IVO KUBĚNA
AUTHOR

VEDOUCÍ PRÁCE   prof. Mgr. TOMÁŠ KRUML, CSc.
SUPERVISOR

BRNO 2012

Abstract: The main aim of the thesis is to explain fatigue behaviour of the ODS Eurofer steel, 14Cr ODS ferritic steel produced in the CEA (Commissariat à l'énergie atomique, Saclay, France) and 14Cr ODS ferritic steel produced in the EPFL (École Polytechnique Fédérale de Laussane, Switzerland). The results are compared with non–ODS variant of Eurofer steel, if possible. This work is part of a wide collaboration coordinated by the EFDA (European Fusion Development Agreement) on development of structural materials for future fusion reactors.

The following experiments were carried out:
• Standard fatigue experiments were performed at room temperature, at 650 ℃ and at 750 ℃. Cyclic hardening/softening curves, cyclic deformation stress–strain curves, Coffin–Manson curves and Wöhler curves were measured. Detailed analysis of hysteresis loops was performed.
• The microstructure of the as–received state was studied by TEM and compared with the microstructure after fatigue loading in order to reveal microstructural changes due to fatigue loading.
• Surface roughening due to cyclic plastic localisation was observed. Crack initiation sites were detected and the mechanism of crack initiation was analysed.
• Kinetics of small fatigue crack growth was measured.

It was found that fine oxide dispersion strengthens studied materials significantly, reduces cyclic softening and stabilises the microstructure in the whole range of testing temperatures. The maximum application temperature is increased. Significant differences in fatigue life of the ODS steels were found and explained by differences in crack initiation mechanisms and small fatigue crack growth rate.

Key words: low cycle fatigue, ODS steels, surface relief evolution, small crack growth rate, fatigue life estimation.

Abstrakt: Hlavním cílem této práce bylo vysvětlit únavové chování ocelí ODS Eurofer, 14Cr ODS feritické oceli vyráběné v CEA (Commissariat à l'énergie atomique, Saclay, France) a 14Cr ODS feritické oceli vyráběné v EPFL (École Polytechnique Fédérale de Laussane, Switzerland). Pokud to bylo možné byly získané výsledky porovnány s ocel Eurofer 97. Tato práce je součástí široké spolupráce, která je zaměřena na vývoj konstrukčních materiálů pro fuzní reaktory.

V průběhu práce byly provedeny následující experimenty:
• Standardní únavové zkoušky za pokojové teploty, při 650 a 750 ℃. Byly získány křivky cyklického zpevnění/změkčení, cyklické deformační křivky, Coffinovy–Mansonovy a Wöhlerovi křivky. Hysterezní smyčky byly detailně analyzovány.
• Pozorování mikrostruktury výchozího stavu pomocí TEM a porovnání s mikrostrukturou po cyklickém zatížení.
• Pozorování povrchového reliéfu, který vznikl díky lokalizaci cyklické plastické deformace - byla odhalena místa iniciace únavových trhlin a byl analyzován mechanismus jejich vzniku.
• Měření kinetiky krátkých únavových trhlin.

Oxidická disperse značně zpevňuje materiály, redukuje cyklické změkčení a stabilizuje mikro–strukturu v celém rozsahu teplot. Byly nalezeny velk´ rozdíly v životnosti jednotlivých ocelí. Ty byly vysvětleny pomocí rozdílných mechanismů iniciace trhlin a jejich různou rychlostí.

Klíčová slova: nízkocyklová únava, ODS oceli, vývoj povrchového reliéfu, rychlost únavových trhlin, odhad únavové životnosti.

Bibliography of the Thesis

KUBĚNA, I. Early stages of fatigue damage of steels for fusion energetics. Brno: University of Technology Brno, Faculty of mechanical engineering, 2012. 130 p. Supervisor: Prof. Mgr. Tomáš Kruml, CSc, Supervisor–specialist: Ass.–Prof. Ing. Libor Pantělejev PhD.

Declaration

I declare that my doctoral thesis "Early stages of fatigue damage of steels for fusion energetics" was written by my own under the supervision of prof. Tomáš Kruml and Ass.–Prof. Libor Pantělejev. All information sources are given in section literature at the end of the thesis.

Brno, 31.10.2012: ....
signature

Acknowledgement

Author of the Thesis thanks to Prof. Mgr. Tomáš Kruml, CSc for his supervising during whole doctoral study and for his willingness to consult whatever was necessary during whole study. Further thanks belong to prof. Jaroslav Polák for discussion of obtained results and to Ass.–Prof. Libor Pantělejev for valuable remarks and hints. Last but not the least, I would like to thank to my colleagues from the Institute of Physics of Materials for opportunity to work with experimental devices and for their valuable advices not only connected with thesis.

My wife Lenka and my parents deserve special thanks for their support and patience during whole study, especially in last weeks before submitting of thesis.

Contents

1 Introduction and main goals

Fossil fuel is going to be exhausted, and its massive usage has very negative environmental effects, thus it is necessary to look for new sources of electric power. One of the promising sources of electrical energy is the thermonuclear fusion. It is the same reaction as running on the Sun and thanks to this energy life on the Earth can exist.

The temperature at the surface of the Sun (figure 1) is 6 000 °C, and in its core about 15 million °C. Temperature combines with very high pressure in the Sun's core to create the conditions necessary to keep the fusion reaction. Much higher temperatures are necessary in the laboratory to ignite the fusion reaction since there is no way to pressurise strongly the burning plasma. In the ITER (International Thermonuclear Experimental Reactor) tokamak, temperatures will reach 150 million °C which is ten times higher temperature than at the core of our Sun [1].

This technology appears to be the environmentally friendly because products from fusion reaction do not include harmful components such as CO_2 and NO_2 which are produced in thermal power plants. The fusion equation chosen for the ITER is:

$$T + D = He + n + 17.6 MeV \qquad (1)$$
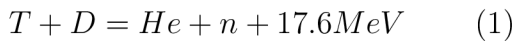
where T (tritium ${}_1^3H$) and D (deuterium ${}_1^2H$) are hydrogen isotopes and n is a free neutron particle.

The development of this complicated technology is coordinated on the European level by EDFA (European fusion Development Agreement). Nowadays, the ITER reactor is under construction in Cadarache in France. The austenitic steel 316L was chosen as the main structural material for the ITER. Un-

Figure 1: The Sun - The biggest source of fusion energy in our solar system [1]

fortunately, the properties of this steel under intense irradiation are not satisfactory, therefore new materials must be developed for the next planned experimental reactor DEMO.

The development of materials must be optimised for wide spectrum of loading parameters including heat and irradiation. The requirements on these materials are good mechanical properties (tensile, fracture, fatigue, creep) in combination with high irradiation resistance and low residual activation. Therefore, materials which are considered to be structural material for future fusion reactors have to be intensively tested. Moreover, the simulations of neutron damage must be performed because of determination of residual activation.

This work is focused on fatigue properties of two 14Cr ODS (oxide dispersion strengthened) ferritic steels and the ODS Eurofer steel.

Main goals

This work is focused on fatigue properties of two 14Cr ODS ferritic steels and the ODS Eurofer steel. Main goals can be specified as:

- Determination of basic fatigue life curves, Manson - Coffin and Wöhler curves at room and elevated temperatures.

- Determination of cyclic hardening/softening curves at room and elevated temperatures.

- Specimen surfaces observation for detection short crack initiation sites.

- Measurement of fatigue crack growth rate.

- Transmission electron microscopy observation for determination of microstructure evolution.

- Explanation of fatigue behaviour of studied ODS steel in relation to the microstructure.

2 Current state of knowledge

2.1 Fusion energy

In this section, the history and present fusion strategy in Europe are described. The timetable of the development of this complicated technology is shown. Then the selected parts of fusion reactor (divertor, coolant system and breeding blanket) are described.

2.1.1 History

The particle accelerator in Cambridge was used for the first thermonuclear fusion reaction by Rutherford et al. in year 1934. In this case, deuterium particles were fused into helium atoms. The idea that the amount of power which is necessary to launch up thermonuclear fusion is always higher than the power which is obtained by its reaction was generally accepted, even by Rutherford. Therefore, particles accelerators were abandoned for these applications. The first TOKAMAK (from Russian: TOroidalnaja KAmera i MAgnitnyje Katuški) was designed by Sacharov in the year 1951. The basic principle of the tokamak is holding of plasma using magnetic field (magnetic holding). Unfortunately, the military activities were a motivation of fusion research at that time. It was demonstrated by the USA in island Elugelab where a hydrogen bomb was launched. The first tokamak "TMP" was constructed in the year 1955, which was composed from a torus with magnetic field and ceramic vacuum vessel. The organisation EURATOM was established in the year 1957 and USA and SSSR began official cooperation one year later. The term "inertial holding" was assessed in the year 1961, which was a new solution of fusion reaction executing. This method does not use any external field for reaction holding. In fact, it is a small controlled explosion of hydrogen bomb. In this case, the start up is accomplished by a strong laser. The problem is that input energy of lasers is higher than economically acceptable value. For that reason, the effort was shifted to tokamaks. Several big tokamaks were built: TFTR (USA), JT-60 (Japan) T-15 (Soviet Union) and the biggest one JET in Culham in United Kingdom. The construction of JET started in the year 1978 and first results were acquired from this device in the year 1991 and the first significant amount of controlled fusion power was produced, when plasma contained 11 % of tritium in deuterium with the gain Q = 0.12. Q is defined by equation:

$$Q = \frac{P_{fusion}}{P_{in}} \tag{2}$$

where P_{fusion} is performance of fusion reaction and P_{in} is power needed for start up of reaction. In the second part of experiments, the quasi steady-state was obtained with fusion power 4 MW for 4s and Q = 0.62. For more information about JET see [2]. In the year 1985, the Soviet Union, France and the USA agreed on the next step in fusion energy, to build a fusion reactor ITER which should have Q = 10, and it is the second most expensive international research project after ISS (International Space Station) until now. The European Union, Japan and Canada joined this project after a short time. The USA left this project in the year 1998 because of financial support reduction for research in this area, nevertheless, the USA rejoined project in the year 2003 together with China and Korea. Nowadays, the ITER construction and other activities are covered by EDFA.

2.1.2   Present fusion strategy

At first, it must be said that the fusion strategy schedule and the material selection is changing very quickly. The situation is described as appeared in the literature in the moment of writing of this chapter.

Recently, two important milestones have been assessed. The first milestone is a demonstration of the feasibility of a fusion power plant. The workable solutions for all critical physics and technology questions must be demonstrated. Moreover, the real assessment of the economy profit must be provided for taking into account the fusion power plant such as a reliable and economically allowable source in long-term energy planning. The success of the first milestone would allow shift from abundant but polluting technologies such as coal burning, to cleaner but scarcer resources, such as gas. A second milestone will be the first delivery of electrical power to the grid, which is planned for the experimental reactor the ITER. The start up of the ITER is not, of course, an end of the development stage of fusion power. In fact, the development will continue even after the start up first generation fusion power plants for increasing thermal efficiency, which has a straight influence on an economical profit [4]. The commercial effectiveness is necessary to accept fusion as relevant source of electricity. Therefore, the achievement of the milestones defined previously must be as fast as possible.

The most of physical and structural problems should be solved in the ITER. According to previous schedule shown in figure 2 the ITER should start the operation at 2012, but some delay in the construction appeared. The construction of the main tokamak building started in August 2010 and the date of the first fusion reaction is expected in the year 2020 [1]. The ITER should serve for experiments of the test blanket modules (TBMs), tritium self-sufficiency breeding module, colling systems and many another technological problems. The test blanket modules (TBMs) should start immediately after the launch of

Milestones:	FIRST PLASMA	Full field, current, and H/CD power	Short DT burn	Q = 10 500 MW	Q = 10 500 MW 400 s	Full non-inductive current drive

	2014	2015	2016	2017	2018	2019	2020	2021	2022	2023	2024	2025
PLASMA AND PERFORMANCE	Integrated Commissioning		Commission machine with plasma. Heating and CD Expts. Reference scenarios in H. H Plasma			Commission with neutrons. Reference scenarios in D. Short DT burn D Plasma		Develop full DT high Q. Develop non-inductive aimed at Q = 5. Low duty. DT Plasma			Improve operation. High duty.	
Equivalent accumulated nominal burn pulses						1	750	1750	3250	5750	8750	11750
BLANKET TESTING			System checkout and characterisation					Performance Test				
			Electromagnetics Hydraulics.		Neutronics Validate			Short-term T breeding. Thermo-mechanics				

Nominal burn: 400 s/500 MW / 0.77 MWm^{-2} on outboard surface
Neutron fluence: 0.12 MWam^{-2} for the first 10 years ➜ Tritium consumption: 4.7 kg
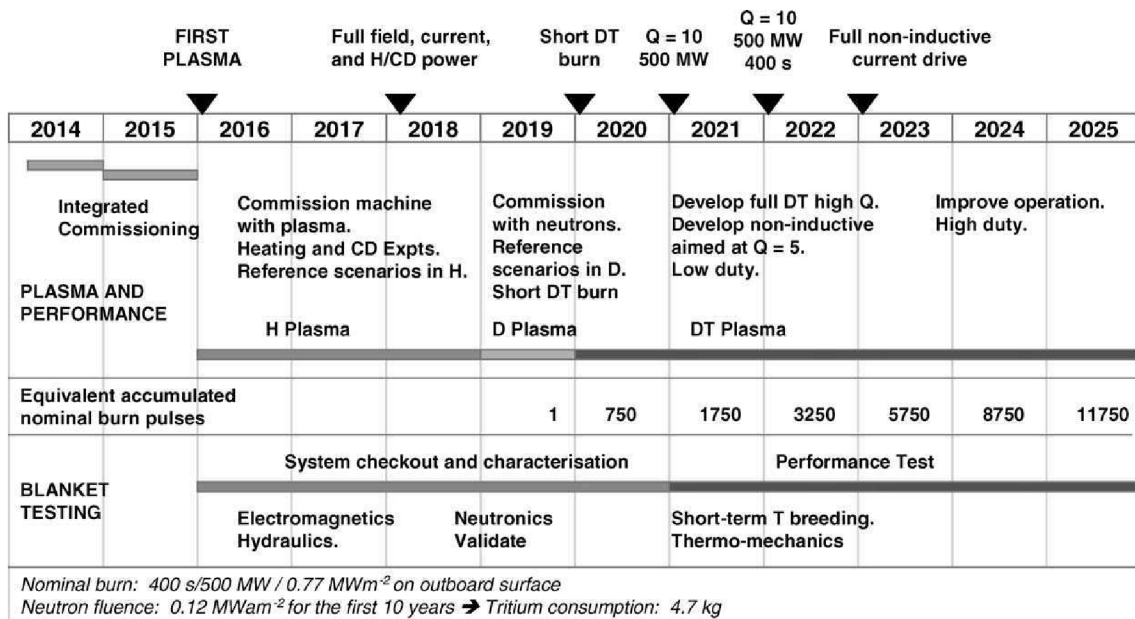
Figure 2: TBMs strategy in ITER [3]

ITER. Solution of this problem is needful for the next step in fusion energy development DEMO. For more information see section 2.1.4 or [3]. The timetable for the first 10 year of ITER operation is shown in figure 2. This first period will be divided in three operational modes. Experiments will be consisted of initial H-H operation for 2.5 years, subsequent short D-D phase and final D-T phase for 6 years. In last D-T phase, several modes for testing are considered. For example, a test with a pulse length of 400 s with neutron wall loading up to 0.78 MWm^{-2} or testing of a pulse length up to 3000 s (inductive + partial current drive) are considered to be performed in D-T phase. The parameter Q = 10 and performance of 500MW should be reached. The expected neutron damage is of about 1.1 dpa (displacement per atom) and 3 dpa after 10 years and 20 years of operation, respectively. Unfortunately, dpa levels required for DEMO are greater than 70 dpa (with possibility to extend it to 150 dpa) and ITER cannot give answer to long-term irradiation effects. Therefore, the existence of fusion relevant irradiation source (for example IFMIF (International Fusion Materials Irradiation Facility) is very important for the development of new materials during ITER operation (see [5]).

Another schedule is shown in figure 3. In the top part, similar programme for ITER as in figure 2 is shown, plus theoretical plan for DEMO. The construction phase of DEMO is estimated to take eight years. Further five years are considered for reaching of full performance. From this moment, DEMO should regularly deliver power to the net with a power plant relevant energetic efficiency, although probably with a reduced availability. According to this schedule DEMO should start its operation in year 2036. In the bottom part of figure 3 timetable of IFMIF development. It is obvious that start of pre-design of DEMO will follow after reaching 80 dpa in IFMIF device and H-H phase in ITER
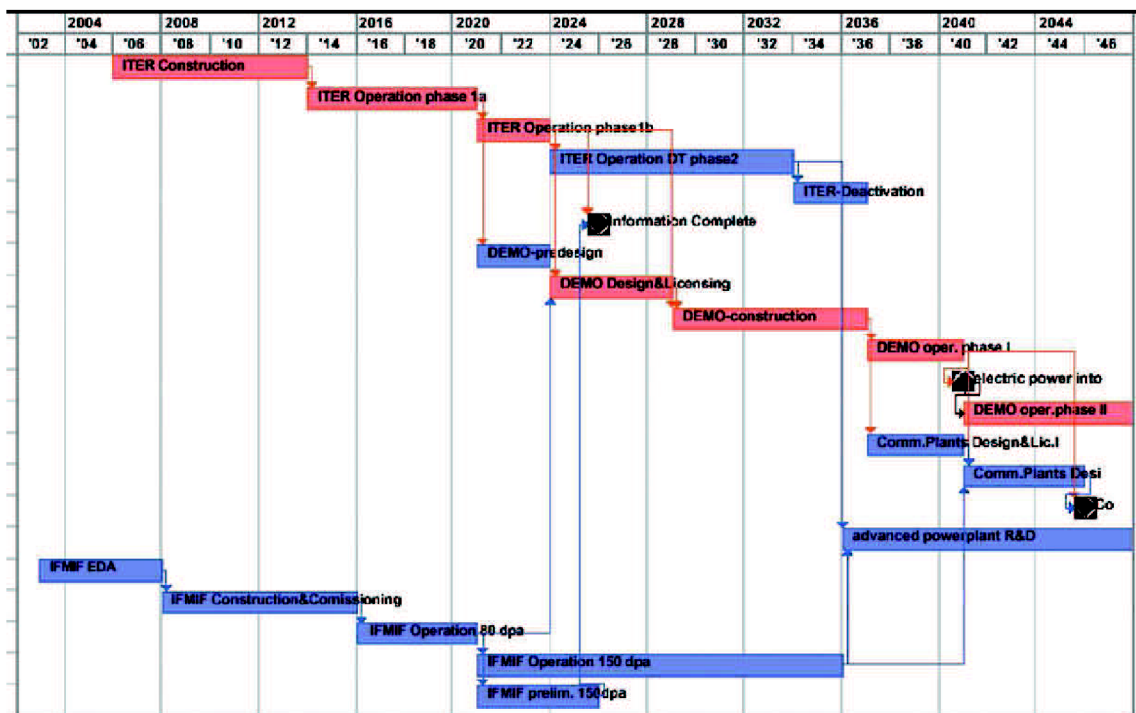

Figure 3: Road map to commercial fusion power production, reference case [4]

device. These information are necessary for the next development. The road map could be accelerated, if a more aggressive concept is adopted. For example, the design phase of DEMO could be divided into two phases. First phase could start immediately after construction of ITER. The second acceleration by assuming a faster progress of DEMO full operation, concretely in three years instead of five years, which are considered in conservative timetable. Unfortunately, each of accelerations increase risk and possible delay in fusion energy [4].

The European programme is based on the concept that DEMO will be very close to a commercial power plant. Therefore, the design of a commercial power plant could start immediately after successful start up full performance of DEMO. At that time, the result of 150 dpa from IFMIF should be known and should establish suitable material with sufficient lifetime [4].

2.1.3   Divertor

The divertor is bottom part of the fusion reactor, which will be under the worst heat and neutron flux conditions. The main function of the divertor is to exhaust helium and most of alpha particles power and to control impurities in plasma. The components in the divertor, so called a plasma face components (PFCs), must carry out a function such as nuclear shield, tritium inventory and so on. The erosion in the strike region will be very high, therefore, the exchange of divertor parts must be possible in a short time. For this reason, the divertor is segmented into 60 cassettes each with PCFs onto cassette body. These cassettes are secured accurately in place on a pair of concentric, toroidal rails which are welded to the vacuum vessel. A cassette is a water cooled stainless steel structure that supports one set of PFCs. The ITER divertor cross-section is shown in figure 4 [1, 6].

2.1.3.1   Armour selection

The materials for the armour or PFCs are being chosen especially from viewpoint of life-time in condition of burning plasma in strike point region and in SOL (scrape-off-layer). The components are designed to basic lifetime of about 1000 full power pulses with projection of surviving more then 3000 pulses. These parts will be intensively sputtered. This

Figure 4: Cross section through the ITER divertor [1]

erosion lifetime can be divided into physical sputtering, chemical sputtering, disruption erosion and slow transient. The estimation of three main candidates for armour (carbon fibre composite CFC, tungsten + 3 % rhenium alloy and beryllium) was given by Pacher et al. [7]. There were considered actions in the strike point region and in SOL, based on initial thickness compatible with maximum operation temperatures (1500 °C for carbon fibres composites and 800 °C for tungsten alloys and Be). The results show that Be has too short lifetime for the regime 10 MWm^{-2} and was excluded from candidates for armour. Tungsten possesses a disadvantage that the melt layer from disruption could re-solidify into an undefined place and the combination with vaporisation of tungsten could pollute the plasma. Tungsten has been selected for the upper part of the reactor and the carbon composite for components under very high heat flux (SOL and the strike point region) [6].

2.1.3.2   Heat flux components

The armour components must be cooled. The basic options of armour cooling are shown in figure 5. Two alloys are considered for cool pipes, CuCrZr and aluminium oxide dispersion strengthened Cu alloy (DS-Cu). The DS-Cu is suitable for all tile geometries, the CuCrZr is unsuitable for the flat tile design. Both alloys shows a loss in ductility at elevated temperatures (150 °C) after irradiation of about 1 dpa. Therefore, temperature of cooling medium will be kept of about 140 °C. The CuCrZr possesses slightly higher tensile properties and significantly higher fracture toughness than the DS-Cu (ten times higher at 350 °C). It is important because of high impulsive electro-magnetic loading. The main advantage of DS-Cu it its better thermal stability. The heating up to 1000 °C has only little effect on its tensile properties. Therefore, the CuCrZr was chosen as material for pipes, only if the operating temperature is too high, the DS-Cu is recommended [6].

For carbon composites, the monoblock geometry is considered. This design minimise the temperature in tube, nevertheless, the flat tile design appears to be cheaper. The pipes are joined to carbon composite by brazing. Firstly, the standard brazing technique based on sliver was used. Unfortunately, the silver could transmute in fusion relevant environment to cadmium which is unacceptable in ultra high vacuum due its low vapour pressure. The new brazing technologies had to be found, diffusion bonding, HIPing, and metal casting are used as well.

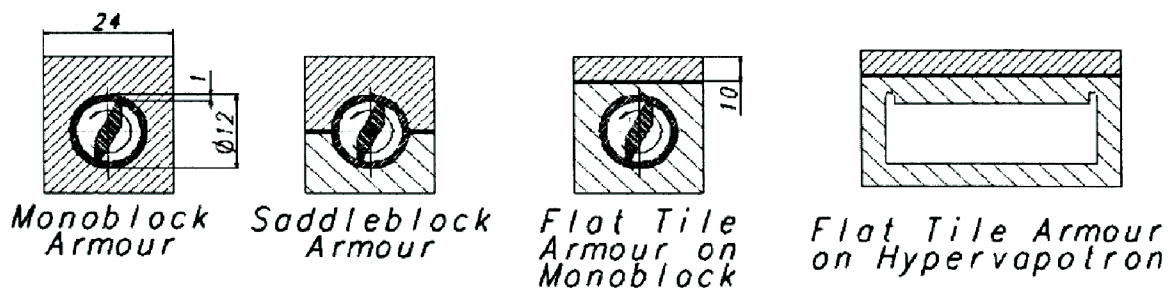For the tungsten armour flat tile structure can be used, because the maximum flux is

Figure 5: Heat sink geometry [6]

limited to 5 MWm^{-2}. The coefficient of thermal expansion of tungsten is very different than in case of copper, therefore, the brush structure must be used for compensation of thermal expansion. This structure is schematically shown in figure 6. In this case, the 316 austenitic steel is chosen as support structure. There is a few options for connection tungsten brushes to the copper substrate in this design, for example the hot pressing at 450 ℃ is probably the simplest way [6].
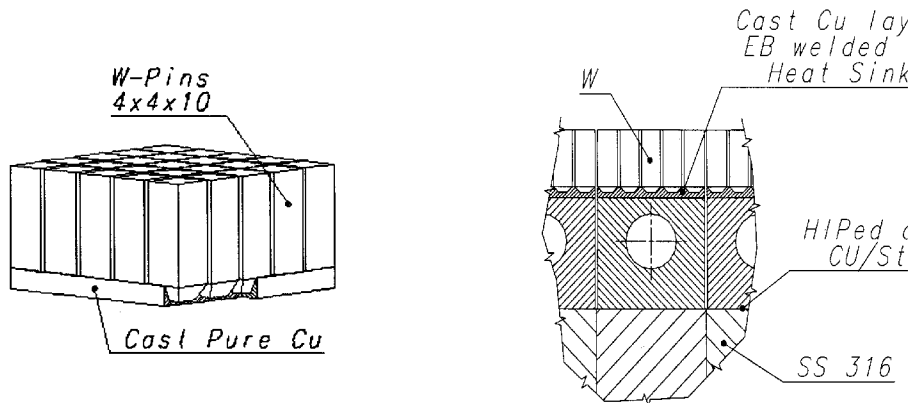

Figure 6: Tungsten brush geometry [6]

2.1.3.3   Target design

The profile of the lower part of the vertical target in the poloidal plane with respect to the field lines is straight in order to ease manufacture of the CFC monoblock, and held at 15 degree to the separatrix to minimise peak heat flux. The W armour will be used in upper part of divertor and the shape and distance decrease the maximum heat flux to 5 MWm^{-2} and less. The vertical targets are composed from a few thin elements, 23 mm width, and they are arranged so that the coolant can run poloidally. This solution is better than toroidal, because a polodial flow arrangement better distributes the strike point heat and it does not expose the vulnerable connection between inlet and outlet to high heat flux. The design with 23 mm width is well supported by results obtained for example in [8]. The upper part of each element is covered by a W brush and it will be kept design in figure 6 and the lower part will be covered by carbon monoblocks, it is shown in figure 7. Each target is armoured and then non-destructive tested. The position of the intersection SOL and strike point can not be exactly determined, therefore, the polodial geometry of target is kept straight over a 500 mm length and it allows fabrication with monoblock. The swirl tape is in the tube in the lower part of target. The speed of swirl flow is quite high (about 12 ms^{-1}) to minimise overall pressure in vertical target. In the upper part of vertical target, the smooth tubes are used, because a loading of this part is much lower then in case of lower part. Thanks to brush structure of armour, the poloidal target can be curved.
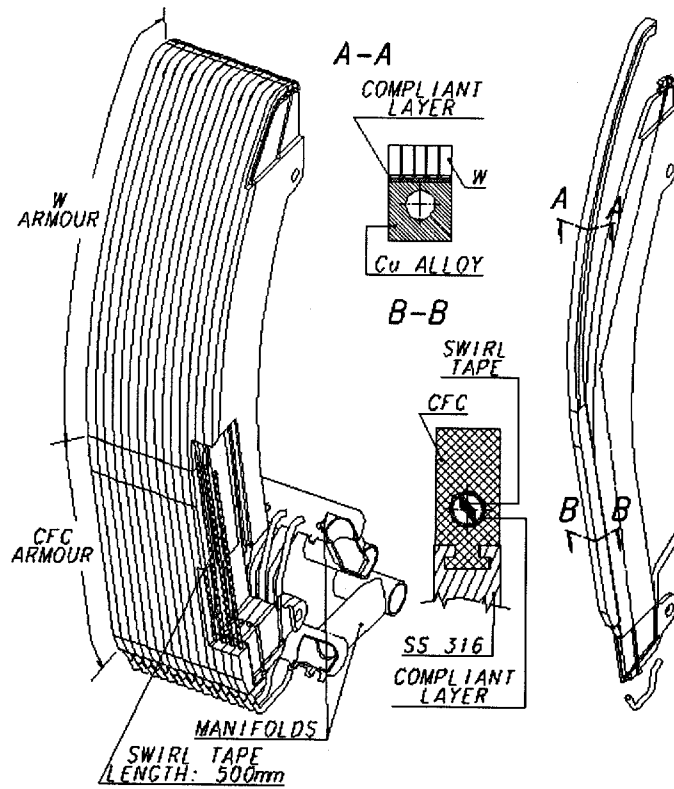
Figure 7: Vertical target [6]

2.1.4 Breeding blanket modules

The schematic of a test blanket modules which is considered for ITER test port is shown in figure 8. The TBMs inside a port must be contained in water cooled steel frame, which provides a standardised interface with the ITER basic structure. To avoid the need of TBM alignment with the ITER shielding blanket, the TBM first wall is recessed of 50 mm
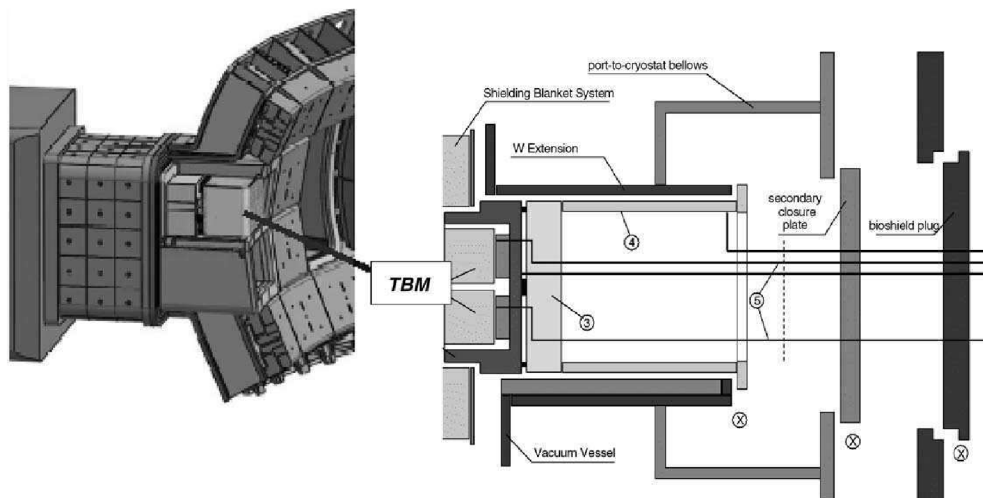
Figure 8: Schematic view of TBMs installed in an ITER test port [3]

and may require a Be protection layer in order to limit sputtering and erosion issues. The location of the circuits and components associated with the TBMis of extreme importance for testing. Behind of each port, there is a space (the port cell) available for placing a movable container with the interfacing equipment. Because of the limited amount of space available in the port cell, some components may be located in the Tokamak Cooling Water System (TCWS) vault and inside the tritium building. TBM systems may use the ITER heat rejection system designed to supply cold water at 35 ℃ and to accept water at 35 ℃. A different coolant system is described in next section [3].

The ITER is probably the only opportunity for testing DEMO-relevant TBMs in a real fusion environment. The most important difference in blanket testing in ITER and DEMO is in the magnitude of neutron flux, neutron influence and so on, which are considered lower for ITER than for DEMO. As a consequence, for each selected blanket concept, several different TBMs have to be developed using different engineering scaling depending on the assessed performance, in order to achieve the corresponding DEMO-relevant working conditions in each dedicated TBM. Maximum expected neutron damage is about 3 dpa (in ferritic steel) even after 20 years of operation, while dpa levels required for DEMO are higher than 70 dpa. Therefore, ITER cannot give answers to long-term irradiation effects on blanket performances, failures, functional, and structural materials, and interfaces, synergistic effects. These should be addressed in other facilities, e.g. fast-neutron fission reactors, fusion neutron sources or the IFMIF facility [3].

2.1.5   Advanced EU coolant concept

The advanced dual coolant concept (A-DC) is on of the EU concept, which was investigated during the long-term power plant conceptual study (PPCS). The scheme of this concept is shown in figure 9. This dual coolant concept is consisted of self-cooled breeding zone with liquid metal Pb-17L serving as breeder and coolant at the same time and of helium cooled RAFM (reduced activation ferritic martensitic) steel structure and of carbon composites serving as electrical and thermal insulator. This design allow relatively high exit temperature of about 700 ℃ for the liquid metal. This temperature is higher then the maximum liquid metal/street structure interference (of about 150 ℃) and of about 100 ℃ then the maximum structure temperature. The thermal efficiency of about 44 % could be reached using a closed cycle helium gas turbine in the power conversion system. Moreover, the use of oxide dispersion strengthened ferritic steels allow increasing of a temperature limit of the first wall up to 650 ℃, which is about 100 ℃ higher then for standard ferritic materials. This idea can be improved using RAFM steel Eurofer for the entire blanket structure where only the first wall is plated with a 2-3 mm thick ODS layer. This solution offers an advantage of using the ODS steel without welding, because only diffusion welding of ODS steel is recommended. In this design, the pressure of helium is quite high (8 MPa) for minimise pumping power. The helium gas will enter at 300 ℃ and its temperature after cooling process increase to 440 ℃. In breeding blanket, the temperature will reach maximally of about 500 ℃ due to decreasing of corrosion. The second designed system will be operated with 280 ℃ entrance temperature and 650 ℃ by leaving of system. The pressure of helium in this part is considered to be 18 MPa [9].
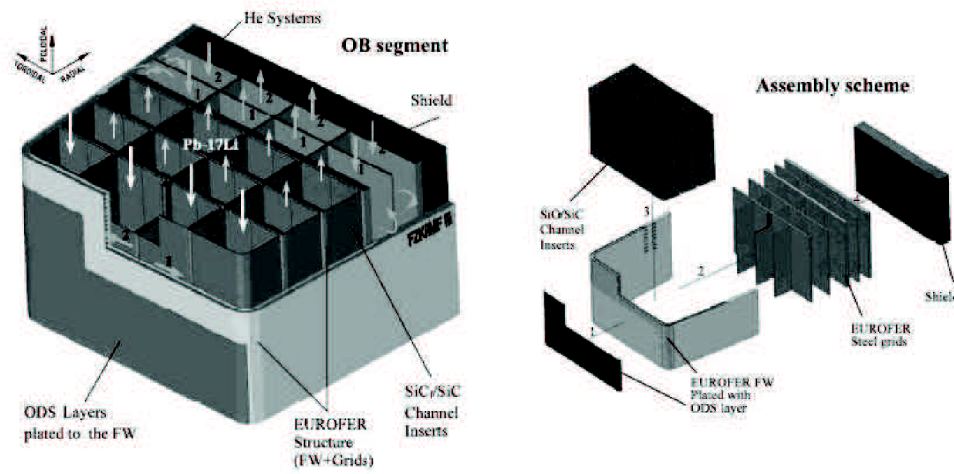
Figure 9: Isometric view of an A-DC outboard blanket segment at torus centre [9]

2.2 Structural materials for the fusion power plant

The selection of structural material is one of the critical issues during fusion energy development. The 316L austenitic steel was chosen as structural material for ITER. Unfortunately, this steel does not belong to group of material with low activation, because this steel contains high amount of nickel, which under irradiation produces isotopes with long decay time. For example, Ni, Cu, N, Mo and Nb are forbidden elements for structural materials under fusion conditions due to the activation properties.

Structural materials will be exposed to very intense neutron radiation originating from the plasma reaction. These neutrons will create damage in materials, especially, displacement cascades, transmutation products and helium implantation. Structural materials must have good physical properties in combination with high irradiation resistance, low residual activation and good compatibility with cooling media. Moreover, for achievement of high thermal efficiency the reactor must be operating at as high temperature as possible.

In first the part of this section, the activation properties of 316L steel are described. In the second part, the RAFM steels with focus on Eurofer steel, Eurofer ODS steel and ferritic steel are reported. These steels are considered as structural materials for fusion reactor. In last part, the tungsten alloys and SiC_f/SiC composites are presented. These materials are considered as protective layer of the blanket structure.

2.2.1 Activation properties of 316L steel

The activation properties for 316L steel and five ferritic steels were calculated by Butterworth et al. in 1984 [10]. The operation time of 2.5 years and the neutron power loading of 7 MWm^{-2} were considered in calculations. The dependence of the transmutation effects, radioactivity, after heat and biological hazard potential on time was determined. The "burn up" (i. e. lowering the amount of an element due to transmutation) of iron, nickel and molybdenum is roughly linear in time.The production of manganese, chromium and vanadium was predicted. The evaluation of production rate of cobalt, hydrogen and helium is more complex. However, it is the worst in case of 316L steel. The isotopes ^{63}Ni, ^{93}Nb, ^{94}Nb and ^{93}Mo are responsible for long-term radioactivity. The radioactivity calculation results in Bqm^{-3} representation show that the radioactivity of 316L steel after the irradiation is higher and decreases significantly slower then radioactivity of studied ferritic steels. The dose rate at which the material can be freely manipulated by hands (hands on dose rate) is 2 x 10^{-5} Gyh^{-1}, but dose rate of the 316L steel after the irradiation is predicted to be of eleven magnitudes higher. This value decreases quite fast because of ^{94}Nb and ^{60}Co isotopes have the half life of 5.3 years. The dose rate drops down to 2 x 10^{-2} Gyh^{-1} after 100 years and this value will be almost constant for next 1000 years. The strong influence of impurities on activation properties was also predicted. The presence of elements such as Ag, Tb, Ir or Bi even at level below 1 ppm can raise the activation to unacceptable levels [10].

The next problem with nickel is the helium formation. The helium is formed in two step reaction of ^{58}Ni with neutron in the mixed spectrum. The reactions are:

$$^{58}_{28}Ni + n = {}^{59}_{28}Ni + \gamma \tag{3}$$

$$\ce{^{59}_{28}Ni + n = {}^{56}_{26}Fe + {}^{4}_{2}He} \tag{4}$$

where γ is gamma ray. The production of $\ce{^{56}_{26}Fe}$ does not present a problem because it is a stable isotope, however the helium presence in the metal matrix is unacceptable [11].

2.2.2   RAFM

The steels, commonly named reduced activation ferritic/martensitic steels, are probably the most promising group of material for structural material for future fusion powerplats. Low activation materials are defined as materials in which the irradiation induces only very low levels (i.e. hands on level) of radioactivity caused by transmutation elements. This condition is unreachable, therefore the term "reduced activation" steels was determined. In these steels small radioactivity is allowed which should decay to low level in 100 years. The dependence of surface gamma dose rate on time after the irradiation is shown in figure 10. The irradiation corresponding to 12.5 MWm^{-2} was considered. The Eurofer 97 steel met the low level waste after the 100 years. Unfortunately, the surface gamma dose rate is constant (still quite high) for the next 10 000 years. Therefore, further reduction of impurities is planned.

Figure 10: Surface gamma dose [4]

Research programs in Japan, European union and USA developed wide group of materials with reduced activation. The steels are alloyed by Cr, W, V, Ta (Mo and Nb is replaced by W and T or V, respectively). The amount of Cr is chosen between 7-12 %. The chemical composition of several RAFM steels is shown in table 1. The concentration of about 12 % Cr exhibits the best corrosion behaviour. In these steels, the delta - ferrite is formed, which is followed by toughness decreasing and chi-phase precipitation during irradiation. Presence of delta ferrite causes embrittlement. It is possible to prevent the formation of delta ferrite by nickel but by using of nickel, the steel does not meet the reduced activation requirement. The steels with about 8-9 % Cr exhibit the best compromise between corrosion resistance and delta ferrite formation. The microstructure of these steels typically contains tempered martensite, $M_{23}C_6$ carbides on prior-austenite grain boundaries with a few small MX precipitates in the matrix [12].
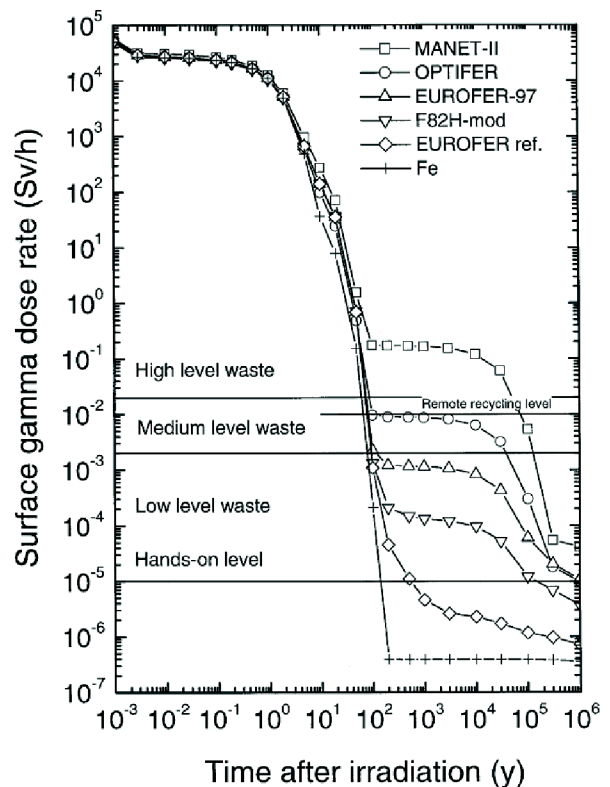
Table 1: Nominal composition of RAFM steels (wt%) [12]

producer	Steel	C	Si	Mn	Cr	W	V	Ta	N	B	Ge
Japan	F82H	0.1	0.1	0.5	8.0	2.0	0.2	0.04	>0.01	0.003	
Japan	F82:-IEA	0.1	0.1	0.1	8.0	2.0	0.2	0.04			
Japan	JLF-1	0.1	0.08	0.45	9.0	2.0	0.2	0.07	0.05		
Europe	Optifer Ia	0.1	0.06	0.5	9.3	1.0	0.25	0.07	0.015	0.006	
Europe	Optifer II	0.125	0.04	0.5	9.4		0.25		0.015	0.006	1.1
Europe	Eurofer	0.11	0.05	0.5	8.5	1.0	0.25	0.08	0.03	0.005	
USA	ORNL	0.1	0.3	0.4	9.0	2.0	0.25	0.07			

2.2.2.1 Irradiation effects

High-energy neutron irradiation in a fusion reactor displaces atoms from their normal lattice positions resulting in formation of vacancies or interstitials. This damage is usually measured as displacement per atom (dpa) and results into voids and dislocations loops that cause swelling. Loop size and loop density decreases with increasing temperature. Dislocation loops become unstable around 400-450 ℃. Vacancies can lead to void swelling up to about 500 ℃. This swelling is lower than in case of austenitic stainless steels. Besides the swelling, the vacancy production during irradiation can accelerate recovery, precipitation processes and induce non-equilibrium phases.

Transmutation reactions of neutrons with metal atoms produce a new isotope with a smaller atomic number and a gas atom (helium or hydrogen). The small number of new isotopes can have an influence on material properties and they become the source of radioactivity. The effect of hydrogen was generally thought to be minimal, because most of it was expected to migrate out of the lattice at reactor operating temperature.

Recent research shows that helium has strong effect on swelling. Therefore, boron and nickel doping becomes undesirable, because natural boron contains about 20% of $^{10}_{5}B$ isotope which can produce helium in the material according to the reaction:

$$^{10}_{5}B + n = {}^{4}_{2}He + {}^{7}_{3}Li \qquad (5)$$

where n is the neutron (fast or thermal). Thermal neutron is a free neutron with kinetic energy < 0.025 eV. Fast neutron is a free neutron with kinetic energy > 1 MeV. Fast neutrons are produced during nuclear fusion. A lot of simulations of swelling process exist, unfortunately, these simulation techniques have problems, because boron is quite reactive element and can be associated with precipitates. Lithium as product of reaction given in Eq. 5 could be problem as well and these simulations do not take into account those features. Furthermore, in fission reactor, all boron is quickly transformed to helium, which is different from what happens in fusion reactor, where helium forms simultaneously with the displacement damage.

The irradiation effect on F82H-mod steel and its welds was studied by Rensman [13]. The steel was irradiated at 300 ℃ with dose levels of 2.5, 5 and 10 dpa. Results of tensile test are shown in figure 11a. The small and dark symbols correspond to $R_{p0.2}$ and the large and open symbols correspond to R_m. It seems that both strength parameters

exhibit a linear dependence on dose level up to 5 dpa, after which the saturation occurs. The impact test results of material irradiated with 2.5 dpa are shown in figure 11b. There is comparison between F82H-mod 25 mm plate and HIP (hot isostatic pressing) powder F82H in non-irradiated and irradiated state. In non-irradiated condition, results are similar to each other, the upper and lower shelf energies are more or less the same, but the DBTT (ductile-brittle transition temperature) is little lower for hipped F82H. After irradiation, the DBTTs exhibit shift (of about 100 °C) in both cases, but still this temperature is little lower for hipped F82H, but the upper self energy of hipped F82H significantly decreases.
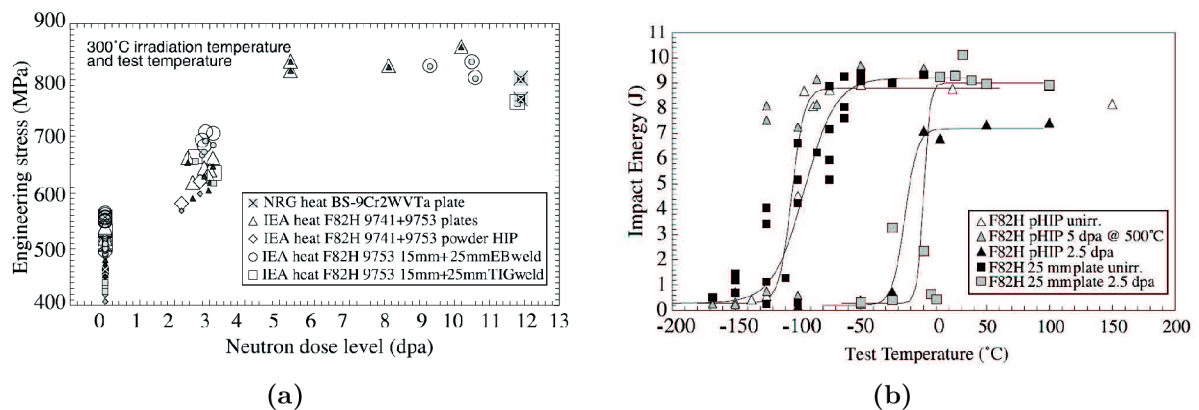

(a)   (b)

Figure 11: Mechanical properties of F82H-mod after irradiation [13]: a) tensile engineering data as function of neutron dose ($R_{p0.2}$ - small dark symbols, R_m - large open symbols), b) impact energies measured in the F82H powder and the F82H-mod irradiated at 300 °C

The other work was focused on low fatigue properties of the F82H steel under proton irradiation [14]. The F82H steel was investigated under three different conditions: unirradiated, irradiated state and during *in-beam* testing (unirradiated specimens irradiated during cycling).

The softening curves of specimens cycled at different conditions are shown. The unirradiated specimens prove the longest life times as was excepted. In case of a specimen, which was tested after irradiation, the life time was shorter by 17 % in comparison with unirradiated one. The continuous softening was observed in both cases and it was more obvious in case of irradiated specimen. The life times of *in-beam* tested specimens were even shorter than those of irradiated specimen. The influence of testing frequency was studied. The fatigue response of a specimen tested with high frequency is quite close to unirradiated specimen, but its life time is significantly shorter. The lowest cyclic softening occurred in a specimen tested with low frequency, but it is still present. The life time is shorter by 10 % in comparison with specimen cycled with high frequency. It could be explained by considering neutron dose. The specimens cycled with low frequency reached a dose of about 30 % higher than at specimens cycled by high frequency [14].

2.2.3   Eurofer 97

The Eurofer 97 steel is the last European variant of the RAFM steel group. The main difference between the Eurofer 97 and previous variants of RAFM steels as F82H, Optifer, Manet etc. consist in higher Ta content which reduces the prior austenitic grains size and results in a finer microstructure. The Mn presence avoids the formation of delta ferrite and high Cr content ensures 100 % martensitic transformation at room temperature. Chemical composition of Eurofer steel is shown in table 1. The heat treatment consists of austenitization at 980 °C for thirty minutes with air shower cooling and subsequent tempering at 760 °C for ninety minutes with air cooling.

Figure 12: Scheme of Eurofer 97 steel microstructure [15]

Schematically, the microstructure of the material is shown in figure 12. The primary austenitic grain is decomposed during cooling into several blocks with martensitic laths elongated in the same direction. Tempering results in formation of roughly equiaxed subgrains with the same diameter as the lath width. Some authors distinguish different packets of martensitic laths inside individual blocks [15].
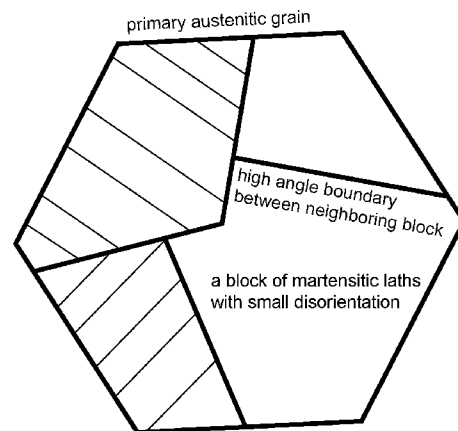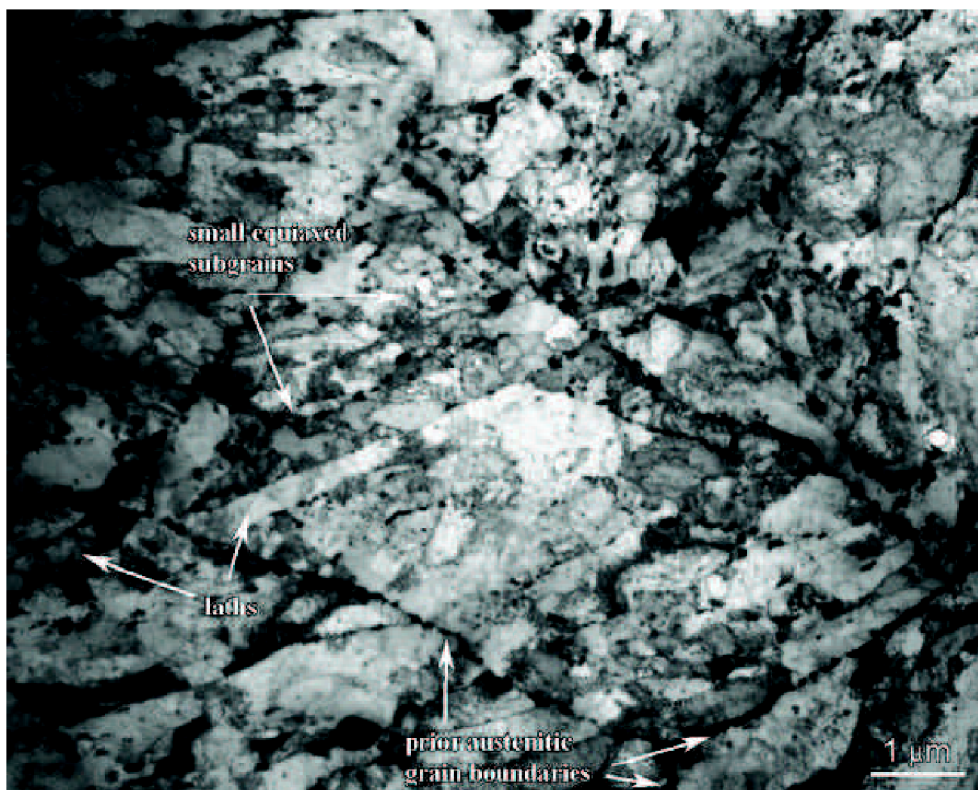

Figure 13: The microstructure of Eurofer 97 steel [16]

The transmission electron microscopy (TEM) was used for experimental determination of microstructure [16]. This observation revealed equiaxed subgrains having a diameter around 0.7 μm (figure 13). Elongated martensitic laths are rather rare, and their thickness was determined to be close to 0.6 μm. This is in an agreement with the value of 0.7 μm given by Sauzay et al. [17]. There exist also larger grains, up to several microns in diameter, which are not fractionated into clearly developed subgrains or cells. The dislocation density is highest in the laths and small grains. There are at least two types of precipitates: fine ones which are more or less regularly distributed in the grains and large ones found mainly on the boundaries or more commonly on the triple points. The large precipitates (about 0.3 μm in diameter) were identified as carbides with high content of Cr and W. Some Ta rich carbides having a smaller dimension (< 0.1 μm) were also identified. It should be noted that the Eurofer microstructure differs from F82H (prior austenitic grain size = 80 μm) and other 9-12 Cr steels by much smaller dimension of the prior austenitic grains, which have diameter about 15 μm [16].

2.2.3.1   Tensile and impact properties

The results of tensile tests performed at 25 °C without the irradiation and after the irradiation are presented in figure 14a [18]. The yield stress of as-received Eurofer steel is of about 550 MPa. Obviously, the deformation behaviour strongly depends on dpa. All of irradiated specimens show significant hardening and decrease of ductility. The stress increase after irradiation by 15.5 dpa is lower of about 200 MPa than after irradiation by 10.9 dpa which is in disagreement with results given by Lucon et al. [20]. Lucon et al. observed the continuous hardening with increasing dpa [20]. The phenomena of increase of ductility between 7.7 dpa and 10.9 dpa is not well understood until now.

The negative influence of irradiation on ductility is confirmed using Charpy tests (figure 14b). The DBTT in the as-received conditions was measured as -90 °C. This
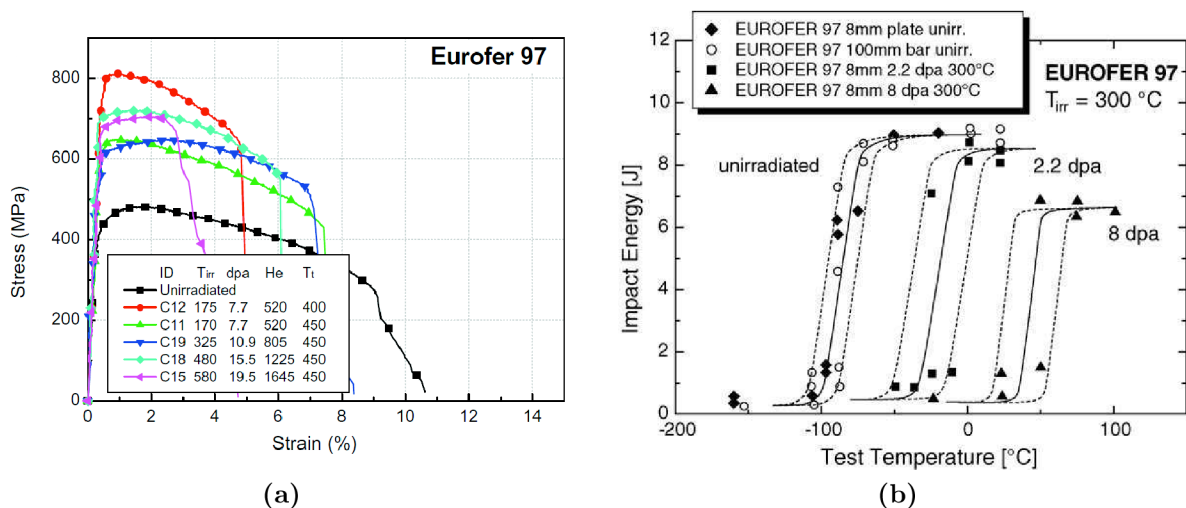

Figure 14: Mechanical properties of Eurofer 97 steel: a) Tensile properties of irradiated specimens at RT [18], b) impact properties [19]

temperature is increased by irradiation at 300 °C with 2.2 dpa and 8 dpa to about -14 °C and +40 °C, respectively. The absolute shift of DBTT is not linear. The decrease of the upper shelf energy is about 0.3 J per dpa [19].

2.2.3.2   Fatigue properties

Fatigue properties of the Eurofer 97 steel at room and elevated temperatures were studied by Marmy and Kruml [16]. Eurofer 97 steel softens during entire fatigue life. After several initial cycles (typically 1-10), the Eurofer 97 steel exhibits slow continuous softening. Its rate is almost constant during cyclic loading. This behaviour is obvious from softening
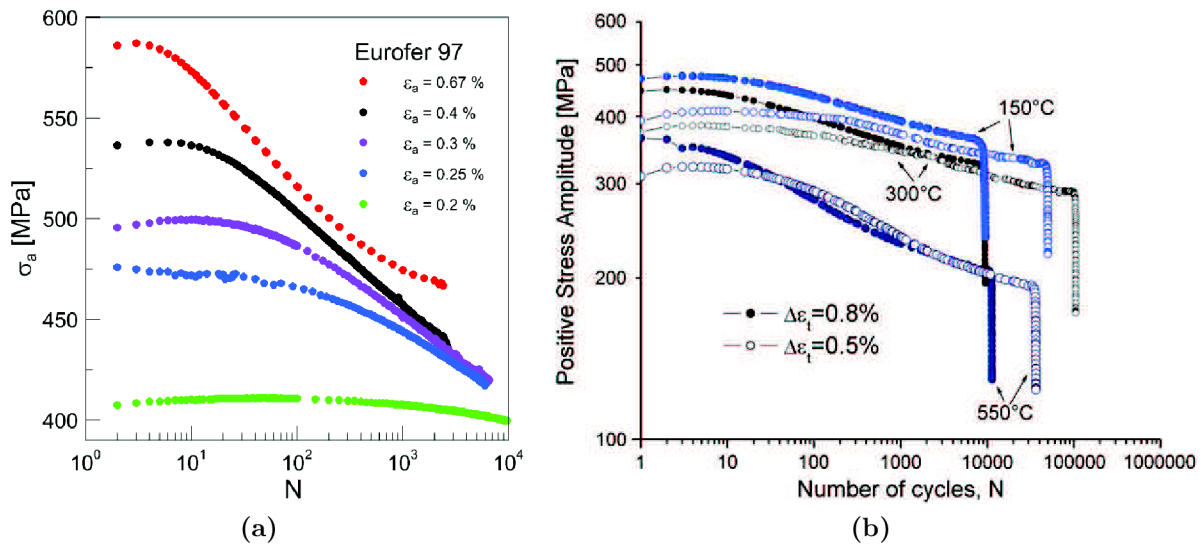

Figure 15: Cyclic softening curves of Eurofer 97 steel: a) at RT [21]; b) at elevated temperatures [16]

curves in figure 15 in $\sigma_a = f(N)$ representation. The softening occurs in whole amplitude range and its intensity depends on total strain amplitude and temperature. This is in agreement with behaviour commonly observed in ferritic-martensitic steels.

The microstructure after fatigue loading at room temperature with 0.8 % total strain amplitude is shown in figure 16a. It is obvious that the microstructure was significantly changed. The martensitic laths are decomposed into subgrain. The overall dislocation density decreases. The grains/subgrains are cleaner and well defined. Dislocations may be observed mainly in small grains, suspected not to be deformed plastically. The large grains do not exist anymore. They were fractioned into fatigue cells and a quite homogeneous microstructure consisting of subgrains of around 1 micrometer in diameter is formed [16].

The microstructure formed at medium temperature range up to 300 °C resembles the one described for room temperature. Nevertheless, the microstructure, which is formed at 550 °C, is different. A subgrain coarsening due to a coalescence of two or more neighboring subgrains induced by cyclic plastic deformation was observed. Almost no dislocations were found in grains [16].
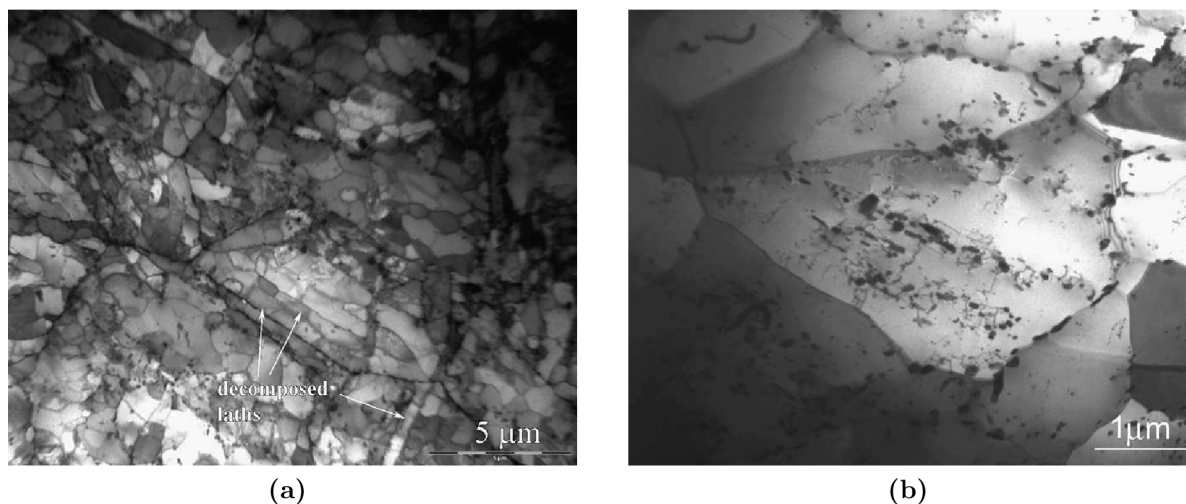
Figure 16: The microstructure of Eurofer 97 steel after cyclic loading [16]: a) Cell structure induced by the cyclic deformation in Eurofer 97, tested in air, at room temperature, at 0.8 % of total strain range, for 7261 cycles, b) Large cells observed in Eurofer 97 continuously cycled with 550℃, in vacuum, with 0.8 % of total strain range, for 11273 cycles

2.2.3.3   Creep properties

The creep curves of the Eurofer 97 steel at 550 ℃ for applied stresses of 285 and 300 MPa are shown in figure 17a. The creep curves appear to be composed of a very short primary stage, characterized by a decreasing strain rate with increasing time, followed by an extended steady state stage and a tertiary stage characterized by an increasing strain rate with time. All specimen exhibited necking and failed in a ductile regime [22]. The Larson-Miller plot of Eurofer 97 and F-82H mod. is shown in figure 17b. As can be seen in the plot, the creep rupture strength of both alloys seem to be equivalent.

The microstructure of Eurofer 97 contains two types of carbides $M_{23}C_6$ and MX (part 2.2.3). The microstructural investigation have shown the presence of a new phase rich in W and Fe. This phase precipitated during creep, which was identified as M_6C type [23].
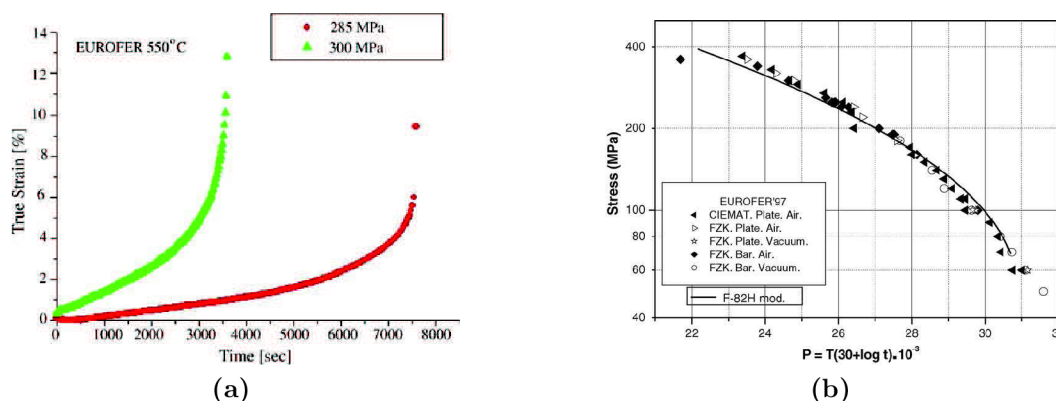

Figure 17: Creep behaviour of Eurofer 97 steel: a) Examples of creep curves at 550 ℃ [22], b) and Larson - Miller plot [23]

2.2.4   ODS Eurofer

The ODS Eurofer development started in year 2002 at CEA (France), CRPP (Switzerland) and FZK (Germany) using the steps:

1. inert gas atomisation of Eurofer 97

2. mechanical alloying with Y_2O_3 particles in industrial ball mills

3. compaction of powders by HIPing (hot isostatic pressing).

2.2.4.1   Microstructure

The microstructures the ODS Eurofer steels with two yttrium content (0.3 % and 0.5 %) were investigated by Schaeublin et al. [24]. The ferrite grains were found, which were decorated with Cr carbides of the $Cr_{23}C_6$ type. The grain size of about 5 μm in both ODS steels is smaller than in the case of the base tempered martensite EUROFER 97, which presents primary austenitic grains of about 15 μm. Oxide particles (Y_2O_3) seem to be heterogeneously distributed (figure 18a). It is possible to found regions free of particles and regions with high particles density. The mean size of particles was determined as 3.8 nm. Lindau et al. used HRTEM (high resolution transmission electron microscopy) for observing nanoparticles. The indicated planes in figure 18b correspond to type of {2 2 2} planes of cubic modification with lattice constant of 1.06 nm [25].

(a)   (b)
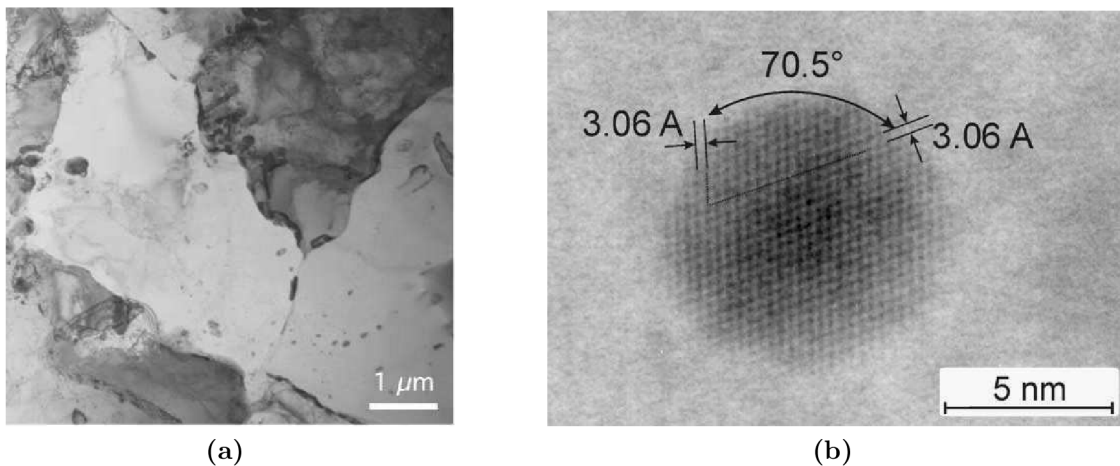
Figure 18: Microstructure of ODS Eurofer steel: a) an overview of microstructure [24] b) HRTEM micrograph of Y_2O_3 particle [25]

2.2.4.2   Tensile and impact properties

Tensile tests show that ultimate stress is increased of about 35 % by oxides at room temperature and this gain is kept up to 700 °C. Several modification of hipped ODS Eurofer

were prepared because of insufficient ductility of ODS Eurofer after hot isostatic pressure (HIP). Different thermo-mechanical treatments and hot extrusion were applied. These treatments do not change strength of materials significantly (see figure 19), but the influence on ductility is enormous. The total elongation of extruded or thermo-mechanically treated ODS Eurofer is increased almost four times in comparison with HIPed ODS Eurofer at temperatures higher than 500 °C.

The influence of thermo-mechanical treatment on ductility is obvious in figure 20. The oxide addition causes increase of DBTT of about 200 °C to 125 °C, which is unacceptable. The thermal treatment of ODS Eurofer has only low influence on DBTT. Thermo-mechanical treatment of this material shifts its DBTT to tolerable temperatures between -60 °C and -40 °C. The upper-shelf energy is decreased by oxide particles of about 40 % and subsequent thermo-mechanical treatment increases this value of about 15 %. It should be noted that data possesses quite a big scatter.
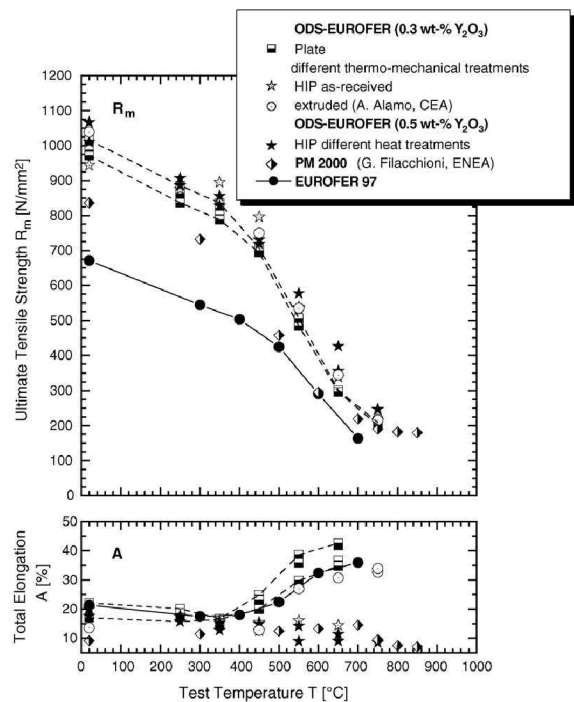
Figure 19: Ultimate tensile strength and total elongation of different ODS steels [19]

2.2.4.3   Fatigue properties

The fatigue properties of ODS materials (9 % Cr ferritic-martensitic ODS steel and 12 % Cr ferritic ODS steel, not exactly ODS Eurofer but with similar chemical composition) were studied by Ukai and Ohtsuka [26]. Both materials were prepared using powder metallurgy and hot extrusion. The cyclic softening curves of two ODS steels and mod. 9Cr-1Mo steel are shown in figure 21. The saturated behaviour was observed in
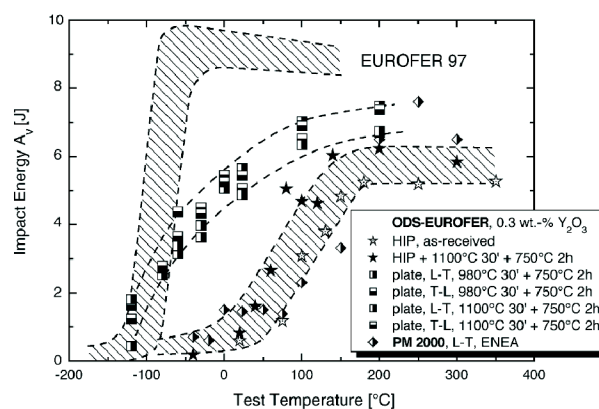
Figure 20: Impact energy measured by standard Charpy test [19]

case of ODS steels, whereas strong cyclic softening was measured in case of 9Cr-1Mo steel, which is typical for ferritic-martensitic steels hardened by precipitates and lath structure [27]. The increase of strength and saturated behaviour is attributed to oxide particles.
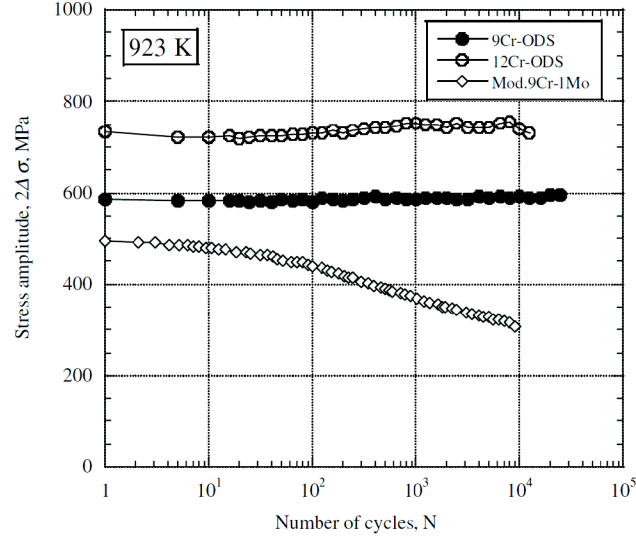
Figure 21: Cyclic softening curves of ODS steels at 650 ℃ [26]

2.2.4.4   Creep properties

The creep response of two variants of ODS Eurofer steel is given in [22]. These steels were produced in the Centre of research in plasma physics (CRPP), Switzerland and in the Commissariat à l'énergie atomique, France. Both steel were produced by powder metallurgy, but there were a couple of differences in preparation. Figures 22a and 22b show the creep curves which was obtained for both ODS steels. The typical three stage in creep plots were found. In the first stage, the deformation increases quite fast in comparison with the second steady state stage. In the second stage, the creep rate is constant. The third stage is followed by a rupture. The size of the total strain and strain rate in steady state stage depends strongly on temperature and applied stress. It is obvious that higher stress level significantly reduces size of steady state stage. The Larson-Miller parameter was used for comparison of two ODS steels and Eurofer 97 steel. The Larson-Miller parameter is determined by equation:

$$P = T_k(30 + log t_m)10^{-3} \tag{6}$$

where T_k is the test temperature in Kelvin and t_m is the creep life in hours. The results are presented in figure 22c. The difference in creep resistance is not significant between two ODS Eurofer steels in this representation. Nevertheless, the Larson-Miller parameter measured in the ODS Eurofer steel is 1.5 times higher than in the Eurofer 97 steel for given applied stress. It means, that the ODS variant can be used of about 65 ℃ higher temperature then the Eurofer 97.
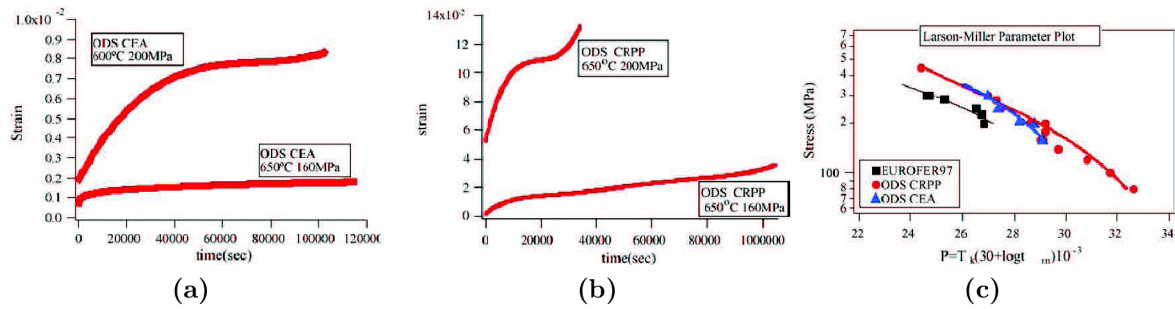
Figure 22: a), b) Creep curves of two ODS Eurofer steels; c) comparison with Eurofer 97 steel in the Larson-Miller plot [22]

2.2.5   Ferritic ODS steels

Ferritic ODS steels are prepared as well as Eurofer ODS steel using powder metallurgy. Either 12 % Cr or 14 % Cr ferritic steels were studied by several laboratories. The preparation of these materials is almost the same as in the case of the Eurofer ODS. It consisted of inert gas atomisation, mechanical alloying with oxide particles and compaction of powders by HIPing. Then different thermal treatment can be used.

2.2.5.1   Microstructure

The microstructure of Fe-14Cr-2W-0.3Ti-0.3Y_2O_3 steel is shown in figure 23. This material was made by hot extrusion. The big differences in microstructure in the longitudinal and transverse direction were observed. In the longitudinal (rolling) direction elongated grains and a high dislocations density can be seen. Contrary, the equiaxed grains were observed in transverse direction. The average diameter of Y-Ti-O nano-clusters measured by TEM were found to be about 5 nm [28].

Figure 23: TEM images of the ODS ferritic steel microstructure [28]: a) the longitudinal direction, b) the transverse direction

2.2.5.2   Mechanical properties

The tensile test results of the ODS ferritic steel described in section 2.2.5.1 are shown in figure 24a. The ultimate stress at room temperature was determined as 1340 MPa in longitudinal (rolling) direction and 1420 MPa in transverse direction. This values are in agreement with results given in [29], where a similar steel was studied. The ultimate stress and the yield stress in transverse direction is slightly higher than in longitudinal direction at a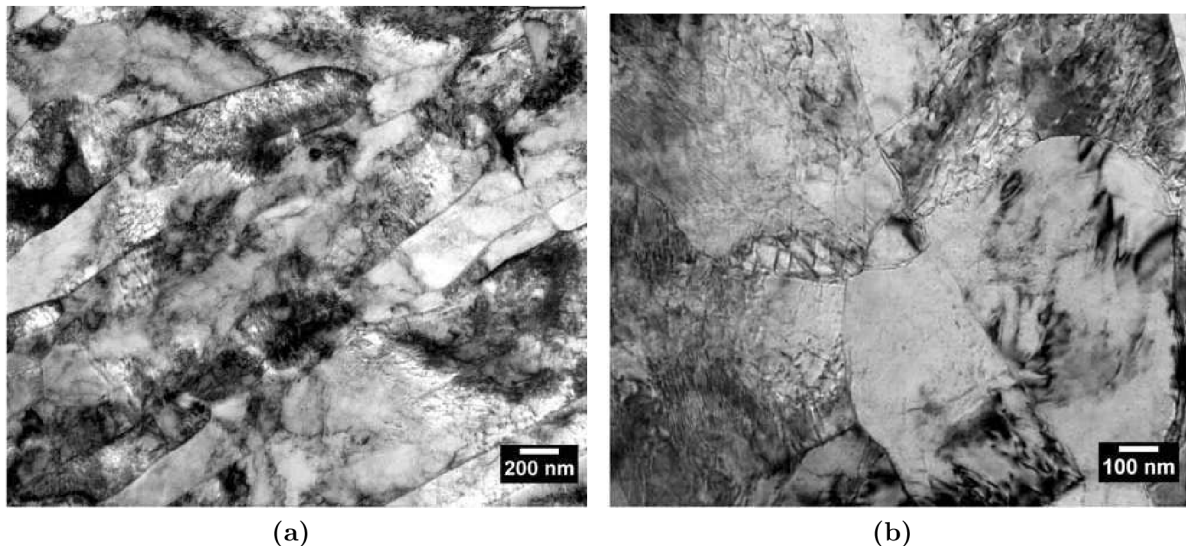ll tested temperatures, the difference decreases with increasing temperature. The figure 24a shows that the decreasing of the yield stress is more significant at temperatures higher than 450 ℃. This material exhibits relatively high yield stress (325 MPa in transverse direction) at 750 ℃.

Recently, another tensile results were published in [30]. The studied 14 % Cr ODS ferritic steel was prepared by powder metallurgy followed by hot extrusion and it exhibits a little bit lower yield stress than the material studied in [28], but it is balanced by considerable increase in ductility. The tensile plastic elongation exceeds 20 % at all testing temperatures [30].

The irradiation influence on tensile properties of 14 % Cr steel was studied by McClintock et al. [29]. Specimens were irradiated at 300 ℃, 580 ℃ and 670 ℃ to 1.5 dpa. The increase in yield stress of about 9 % was measured for specimens irradiated at 300 ℃ and tested at RT. The increase of the yield stress in other specimens is close to each other between 10-20 %, depending on test temperature. The increase of strength is accompanied by the decrease of ductility. The decrease of total elongation of about 6 % was measured in irradiated specimens.

The Charpy impact test results are shown in figure 24b [28]. This steel, due to the anisotropy of the microstructure after hot extrusion and hot rolling, exhibits significantly different impact properties in the two perpendicular directions. Relatively low upper
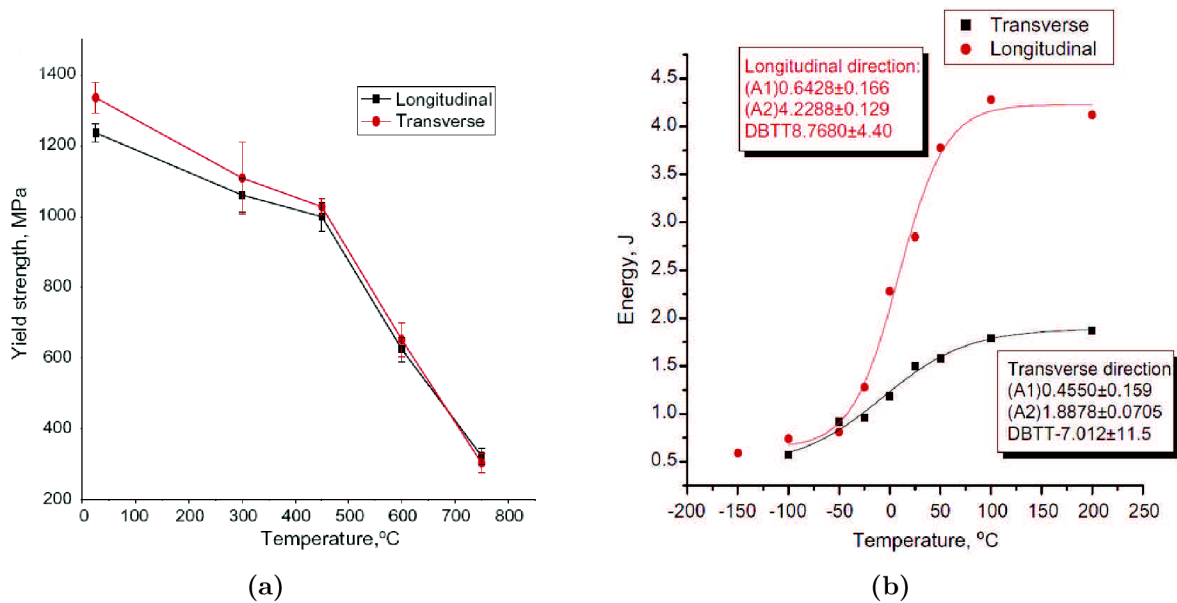

(a)   (b)

Figure 24: Mechanical properties of ferritic steel [28]: a) tensile properties, b) impact properties

shelf energy of about 1.9 J and the DBTT of about 7 ℃ were measured in the transverse direction. In the longitudinal direction larger upper shelf energy and DBTT values, of about 4.2 J and 9 ℃, respectively, were measured.

The fatigue or creep properties have not been published until now, with the exception of already mentioned work [26] (see figure 21).

2.2.6 Tungsten alloys

Tungsten is a candidate for protective armour on the first wall of a fusion power plant and the material main candidate for the divertor. Advantages of tungsten are very high meting point, high strength, high creep resistance, high thermal conductivity and high erosion resistance. The drawbacks include brittleness at room temperature, generally low fracture toughness, ductile to brittle transition temperature above room temperature and tensile elongation ofalmost zero at room temperature [31, 32, 33].

To enhance the properties of present tungsten alloys for safe operation at about 1000 ℃ under pressurised conditions (10 MPa) is challenging. One of possibilities is producing ultra fine grains (UFG) materials with low interstitial content. Simultaneously, the fundamental study of failure modes and of brittle behaviour is needed as well as determination of strength and creep rate between 900 ℃ and 1500 ℃, fracture toughness between RT and 1500 ℃ and fatigue properties (life curve and crack propagation) between RT and 1500 ℃.

2.2.6.1 Status of development

The first objective is to specify the suitable chemical composition. After investigating, W10La (W with 1 % La_2O_3) and WVM (W with modest potassium doping) was found to be primary candidates. The UFG structure proves increase of fracture toughness by a factor five to 30 MPam$^{0.5}$ and severe plastic deformation (SPD) decreases the high DBTT inherent for W alloys. A combination of redistribution of impurities and high dislocation densities seems to be responsible for the high fracture toughness. Unfortunately, these results were reached only at laboratory scale. The microstructure of WVM alloy after high pressure torsion (HTP) was found relatively stable after being exposed to 1200 ℃ for 1h, but fractures toughness after this heat treatment is reduced [31].

W alloys exhibits a ductile to brittle transition typical for bcc metals, but parameters governing ductility are more complex than in the case of steels and not yet fully understood. Present activities are the development of a microstructural based criterion for the optimisation of fracture toughness. The effects of the grain size and shape, grain boundary character and dislocation density and arrangement are under development [31].

Low permanent hydrogen retention at elevated temperatures is very one of advantages of tungsten. The formation of H bubbles, as well as the blistering due to He, observed in laboratory after high dose of H or He, are still under discussion. Sputtering by deuterium occurs only at relatively high energies (e.g. sputtering rate 10^{-3} for 400 eV ions) so sufficiently cold plasma in the SOL and in front of the target plates does not lead to substantial erosion [32].

2.2.6.2   Bulk components

In a reactor, bulk tungsten components solutions have to be foreseen. Several experiments with bulk W limiters to explore their behaviour under fusion relevant conditions was performed in Textor tokamak. The technical concept depends on the cooling medium. The latter requires relative high pressures but allows high coolant temperatures. In such a case, the cooling structure itself could be designed from W components. Figure 25 shows the concept of W-thimbles which are designed as part of a He cooled divertor in DEMO [32].
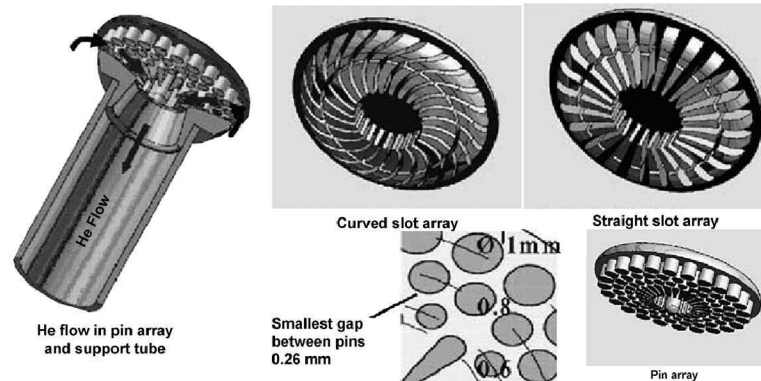
Figure 25: Principle layout of W cooling tubes and different array structures for a He cooled divertor [32]

2.2.6.3   Activation properties

The tungsten layer is considered to be an armour of blanket structure as was described in section 2.1.3.1.

This armour layer will be exposed to high neutron flux, therefore, the study of activation properties is needed. The activation behaviour of a 2 mm thick layer of tungsten was studied by Taylor and Pampin [33]. Two (helium or water cooled) plant models were assumed. The numerical calculations were performed using 3D model, it is shown in figure 26.

The activation properties are summarised in figure 27. The specific activity of the tungsten after the end of operation is shown in figure 27a for both plant model A and B. For comparison, plant model D was added, which assumes silicon carbide composite blanket structure. The gamma dose rate in contact with
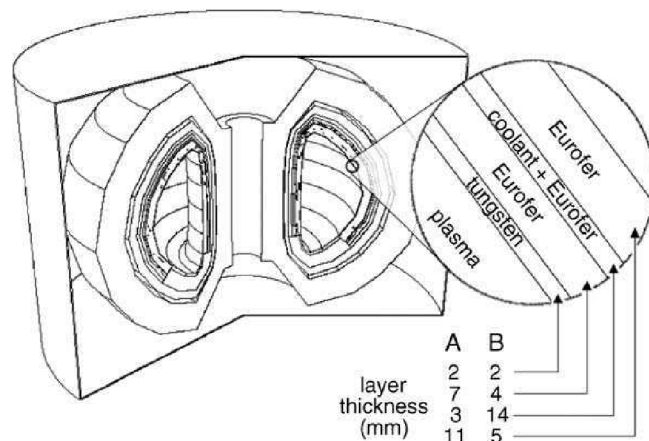
Figure 26: Illustration of the model geometry with the thicknesses of first wall layers for Plant models A and B. [33]

tungsten is plotted in figure 27b, for both plant models again. The same calculation was performed for Eurofer steel blanket structure and data were plotted in the figure 27b for comparison. The dose rate is very important parameter in the criteria for categorisation of active materials. Moreover, the high dose rate at early times has an impact on mainte-
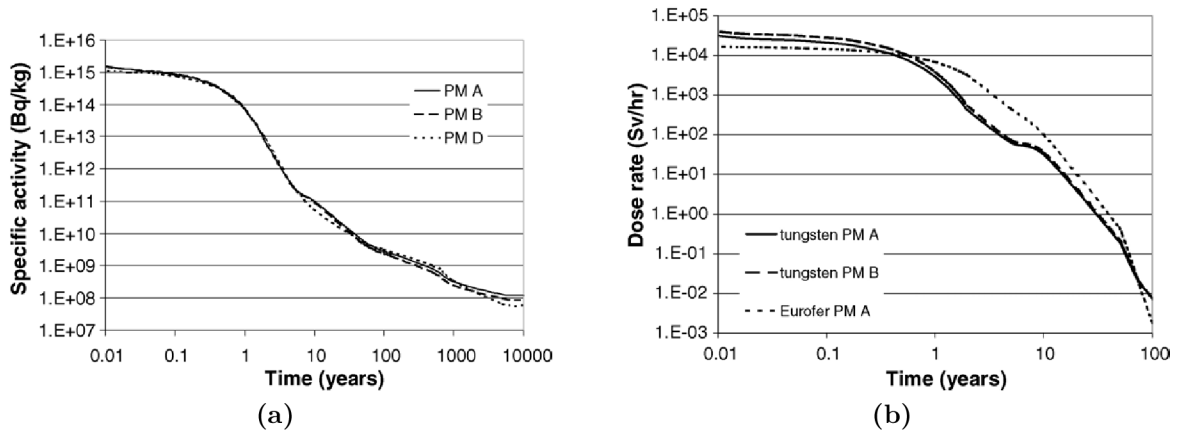
Figure 27: Activation properties of tungsten armour [33]: a) specific activity in tungsten armour of plants model A, B, D; b) contact gamma dose-rate of plants model A, B and of Eurofer with no armour

nance operation. The gamma dose rate is above 10 000 Sv/h for around six months after shutdown, it is challenge for handling equipment. Although the result for tungsten after this six months is better than in case of Eurofer steel, its radioactivity is still to high for maintenance procedures. Anyway, from figure 27 it is obvious that the values are very similar for both plant models. This illustrates that the neutron spectra in the blanket have little influence on the activation properties of tungsten armour [33].

2.2.7 SiC$_f$/SiC composites

At present, a last group of materials considered as a structural material for the fusion power plant are composites. The SiC$_f$/SiC composite possesses very good high temperature properties and good activation properties in short and medium term. Operation temperature is considered to be between 600 ℃ and 1000 ℃. Its drawbacks are high gas production due to nuclear transmutation, fast properties degradation under irradiation and low plastic properties [34].

These composites are produced in 2D and 3D arrangement. Two dimensional (2D) variant is produced by stacking and pressing layers and possesses about 40 volumetric % of fibers with planar arrangement. 3D variant is characterised by about 35 volumetric % of fibers and about 10 volumetric % of fibers going perpendicularly to lamination [34].

2.2.7.1 Mechanical properties

The basic mechanical properties of SiC$_f$/SiC are summarised in table 2. It is obvious that the composite exhibits higher Young's modulus and lower strength dependence on temperature than in case of steels, but plastic properties are very low. The fracture

surface after monotonic bending test at room temperature is shown in figure 28. The pull out of fibers occurred. This feature is more pronounced at room temperature than at 1000 ℃ [34].

Table 2: Mechanical properties of SiC_f/SiC composite [34]

Compsite	2D	3D
Fiber volume [%]	41	35
Density [g/cm^3]	2.73	2.65
Young's modulus [GPa]	295	252
Tensile strength [MPa]	272	198
Bending strength at RT [MPa]	356 ± 47	-
Bending strength at 600 ℃ [MPa]	303 ± 11	-
Bending strength at 1000 ℃ [MPa]	268 ± 27	-
Strain to failure at RT, 600 ℃, 1000 ℃ [%]	0.19, 0.16, 0.15	-

A few results from fatigue test were obtained. The test duration was limited to $0.8 \times \tilde{1}0^5$ cycles and four-point bending cyclic test was used. This composite exhibits good fatigue response at RT. The specimens loaded less than 98% of bending strength were not broken after 0.8×10^5 cycles. This amplitudes are higher than matrix cracking stress (100 MPa). It indicates that the composite can stop the cracks propagation which are produced in first cycles. The crack can be stopped because fiber bridging reduces stress intensity at it tip. The hysteresis loops indicate that the composite exhibits the saturated behaviour, it means the elastic modulus and the stress amplitude remain
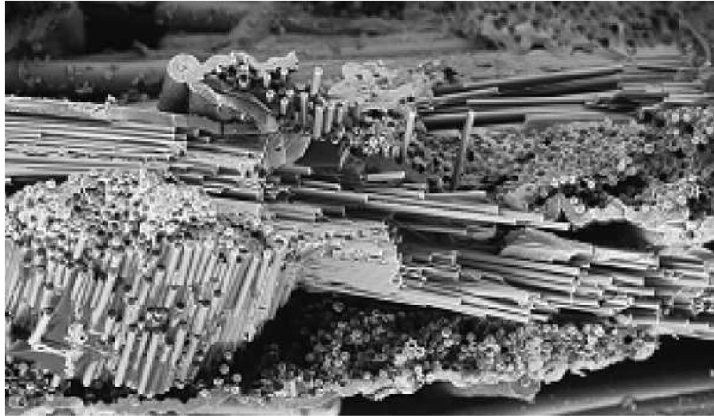

Figure 28: Fracture surface after monotonic bending testing at RT [34]

constant during cycling. The cyclic behaviour of this material is different at 1000 ℃. Long life time was observed only for stress amplitude below 40 % of bending strength at 1000 ℃. From hysteresis loops the fatigue softening during entire testing is obvious. At both temperatures the fiber pull out is absent [34].

2.3   Fatigue damage

The term "fatigue of materials" does not seem to fit into precise technical terminology. However, there is a certain analogy between fatigue in the common sense of the life, and fatigue of metals. When a machine part or a whole structure is loaded by cyclic external forces, a complete fracture may occur, although no obvious damage can be observed throughout the majority of loading cycles. Moreover, the magnitude of external forces may be so small that their single application does not result in any detectable damage. The final fatigue fracture is preceded by complex microscopical changes in structure, which are of a cumulative and irreversible type [27].

The fatigue process is controlled by cyclic plastic deformation. It is generally known that pure elastic deformation is fully reversible and no repeated plastic deformation means no damage. The plastic strain amplitude at the fatigue limit is of the order of 10^{-5} for most materials. This plastic strain, applied only once, does not cause any substantial changes in the structure, but multiple repetition of this plastic deformation leads to the fatigue fracture [27, 35, 36].

In the next part of this work, the individual stages of fatigue life are described with focus on vacancy models of surface relief evolution.

2.3.1   Stages of fatigue life

The fatigue process can be separated into individual stages and substages, see figure 29 [36]. From the engineering point of view, the fatigue life can be separated into the initiation stage of an engineering crack, and the stage where the crack propagates until it reaches its critical length. This stage can be described using the fracture mechanics. The macrocrack initiation description requires the microscopic approach. This approach distinguishes important substages in the domain of macrocrack initiation (figure 29). The fatigue process starts by initial hardening/softening phase which is connected to the evolution of the dislocation microstructure. Then usually the cyclic strain localisation into persistent slip bands (PSBs) and surface relief evolution occurs. So called persistent slip markings (PSMs) can be observed on the specimen surface as a result of the intersection of PSBs and specimen surface. Fatigue cracks initiate often within PSBs and then they grow and affect each other. The individual stages are described in detail in next chapters.
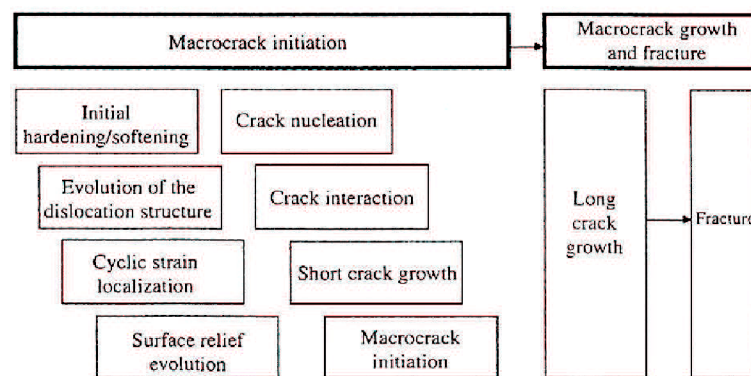

Figure 29: Evolution of fatigue damage in crystalline materials [36]

Please note that the different notation is used for the bands in the bulk of materials in which the plastic deformation is localised (PSB) and for the relief formed on the surface (PSM). Often in the literature, the term PSB is used for both features.

2.3.2   Cyclic stress-strain response, hardening/softening curves

The cyclic stress-strain response is generally studied using smooth bodies that are subjected to cyclic loading, in order to generate homogeneous stress and strain in a larger volume of the specimen. Three basic regimes are adopted for fatigue test: constant plastic strain amplitude (ε_{ap}), constant total strain amplitude (ε_a) or constant stress amplitude (σ_a) regime. During a test, one parameter (for example: ε_a) is kept constant and the remaining parameters can be measured. Almost for all materials, the remaining parameters are not constant during cycling, especially in the beginning of cycling. The size of changes decreases in number of cycles, some materials possess a stable (saturated) behaviour after initial softening or hardening stage. The best solution how to show this behaviour is by hysteresis loops (figure 30). The hysteresis loop is plotted in selected cycles and then the plots are analysed. Three basic parameters, ε_{ap}, ε_a and σ_a (one is under control and two remaining depend on materials response) can be easily measured. These quantities can be plotted as a function of number of cycles, usually called hardening or softening curves. An example of cyclic softening curves was described in section 2.2.3.2.

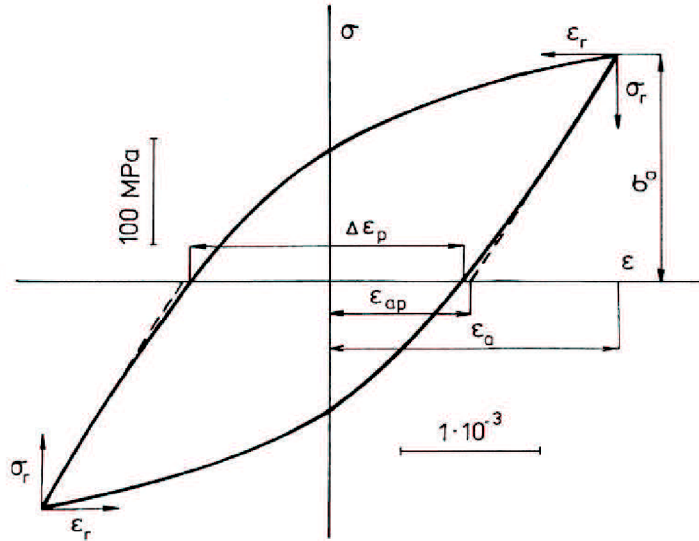**Figure 30:** Hysteresis loop [35]

The useful parameter describing a hysteresis loop shape is called V_H [37] parameter and this parameter is determined by equation:

$$V_H = \frac{W}{4\varepsilon_{ap}\sigma_a} \tag{7}$$

where W is the hysteresis loop area, which represents the specific energy dissipated in a material within one cycle. The dependence of V_H parameter and stress amplitude on

number of cycles of 316L austenitic steel is shown in figure 31. The presence of the first persistent slip marking was found after 10 - 50 cycles corresponding very well with the local minimum of V_H [38]. The fact that the cyclic slip localisation occurs when the V_H parameter curve reaches its minimum is in agreement with data obtained for fcc single [36] and polycrystals [39].
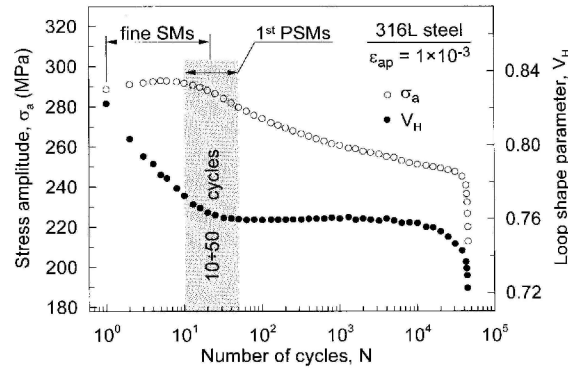

Figure 31: Vh parameter and softening curve of 316L steel [38]

2.3.3 Effective and internal stresses

The motion of dislocations under an external applied stress in a crystal is opposed by short–wavelength and long–wavelength fluctuating forces. In the first class, lattice friction, contact interactions with localised obstacles and short–wavelength fluctuating elastic stresses participate. The stress necessary to overcome these obstacles is called effective stress σ^*. In the second class, we find long-wavelength fluctuating elastic stresses, which originate typically due to groups of dislocations. The amplitude of the long–wavelength stresses is identified with macroscopic internal stresses σ_i [40]. In cyclic loading, stress amplitude can be resolved in these two additive components [35]:

$$\sigma_a = \sigma_a^* + \sigma_{ai} \tag{8}$$

These two components can be experimentally separated, e.g. by strain dip test method used for creep testing [41, 42] or constant strain rate testing [43]. Mughrabi [44] presented composite model for Cu with developed ladder structure. He considered that the ladder structure is composed of two parts with very different levels of internal stress, "soft" channels with low dislocation density and "hard" dislocation walls. Saada recently generalised this model for n domains with variable internal stresses [45] in an attempt to describe different response of a mild steel in tension and compression. In this work, we will use similar approach, the statistical theory derived by Masing and further developed by Polák [35]. This theory assumes that 1) the microstructure consist of continual distribution of microvolumes. Effective stress is the same for all microvolumes, but internal stress may differ in each microvolume. Total strain is the same for all microvolumes which implies that plastic strain differs for each microvolume. No further assumptions about the microstructure are necessary. According to this theory, it is useful to plot a hysteresis half–loop in relative coordinates with the origin in the minimum (or maximum) stress,

and to make first and second derivative of this curve (see schematics in figure 32). The statistical theory correlates the minumum of the second derivative with the effective stress and the curve after this minimum corresponds with the distribution microvolumes with given internal stresses. This theory was applied on several kind of materials, e.g. duplex steel [46]. The example of second derivative of the hysteresis half loop of duplex steel is given in figure 33. After the minimum, two distinct maximas are formed which correspond to plastic deformation of microvolumes in austenitic and ferritic phases [46].
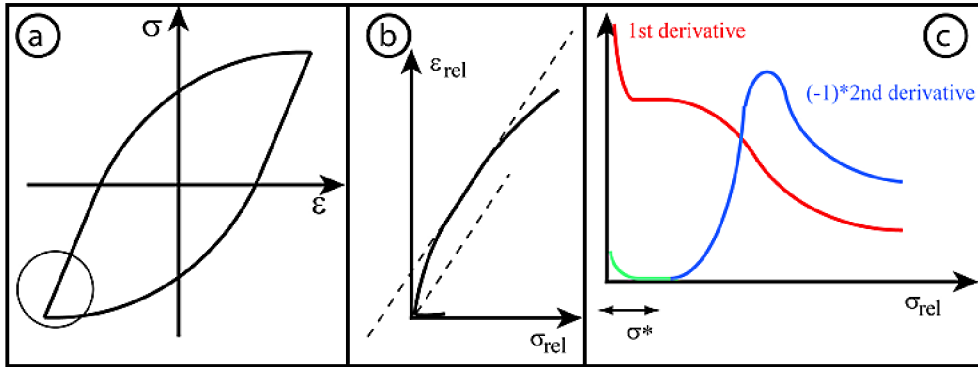
Figure 32: a) Example of a hysteresis loop; b) use of relative coordinates; c) first and second derivative (multiplied by -1)
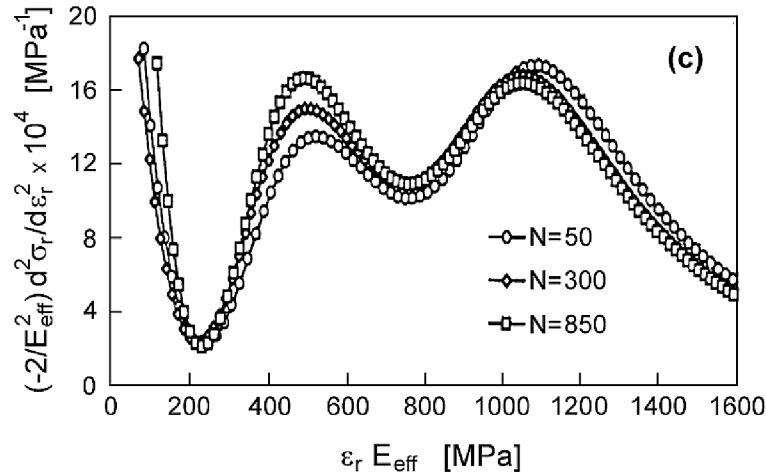
Figure 33: Two maximas on the second derivative of hysteresis loop of a duplex steel show different levels of internal stress in austenitic and ferritic phases [46]

2.3.4   Surface relief formation

The first observation of surface relief in fatigue was performed by Ewing and Humfrey using optical microscopy [47]. Polycrystalline Swedish iron fatigued by rotating bending was studied. The repolishing technique was used to show that the slip bands were persistent. The PSMs can have different forms, but most often material is pushed off from the crystal and an extrusion arises, or the original surface deepens and an intrusion is formed

[36]. The morphology of well developed PSMs differs in single crystals and in polycrystals. Whereas macro-PSMs are typical for single crystals, individual PSMs are present both in single and in polycrystals. The PSBs have different dislocation microstructure and different mechanical and physical properties than a surrounding matrix [35].

Numerous models involving the formation of extrusions, intrusions and fatigue crack initiation have been proposed. The latest models of surface relief formation and fatigue crack initiation can be divided in three categories:

1. Surface-stress-assisted models.

2. Vacancy models.

3. Micromechanical models.

In the following part of this work, several models of surface relief formation and crack initiation are described. To give thorough overview is very difficult and it exceeds range of this thesis. For more detail, reader is recommended to references [35, 36, 38, 48].

2.3.4.1   Surface-stress-assisted models

Brown's model
The ladder like dislocation structure (consisting of alternating thin dipolar dislocation walls and wide channels where almost no dislocations were found) of PSBs was considered for fatigue crack initiation [49]. Taking into account the experimental findings that the dipoles in the walls of PSB and the matrix are mostly of vacancy type and their density within the PSB is much larger than in the matrix, they concluded that the whole PSB layer experiences a macroscopic tensile internal stress in direction of the primary Burgers vector. This stress was visualised by two extrusion in both ends of PSB, and it is driving force for decohesion of matrix and the PSB. According to this model, the height of the static extrusion h_e can be calculated by equation:

$$h_e = \varepsilon_f D \tag{9}$$

where D is a grain size and ε_f corresponds to tensile fiber strain at the PBS and matrix interface. This equation is in qualitative agreement with some experimental results, but only for static extrusion [38]. The vacancy migration is not taken into account, therefore this model does not describe development of extrusions [49].

Zhai et al. model
The similar dislocation arrangement as in Brown's model was suggested by Zhai et al. [50]. It was suggested that under the combined loading of applied and internal stress, the walls in the PBS can collapse, resulting in a large number of vacancies, microcrack or microvoid can be formed near the surface. This model does not respect a dynamic equilibrium between multiplication and annihilation of dislocations. The applicability of this model is limited to special configuration of fatigued aluminium single crystals [50].

2.3.4.2   Vacancy models

EGM model

The real dislocation structure of a PSB in cooper was presupposed by Essmann et al. [51] to create realistic model of surface relief formation. In this model, the surface profile at the emerging PSB is divided to two processes: a) the rapid formation of static extrusion and b) the slow development of surface roughness by random irreversible slip [51].

The EGM (Essmann, Gössele, Mughrabi) model is based on the analysis of steady-state cyclic deformation in PSBs, involving the dynamic production and annihilation of both dislocations and point defects [51]. The vacancy type defects are predominately produced [35]. Contrary to the Brown's model, the PBS is considered to be in compression. The height of the static extrusion is precisely equivalent to the number of vacancies in the PSB in the cyclic saturation according following equation:

$$h_e = \frac{f_w C_v^{sat} D}{2} \qquad (10)$$

where C_v^{sat} is a saturated vacancy concentration in the walls, f_w is volume of PSB occupied by walls and D is grain size or specimen diameter in the case of monocrystals. The roughening of static extrusion is controlled by random slip. This roughness and the PBS-matrix interface are considered as stress concentration places and crack initiation sites. No intrusions are considered in this model contrary to some experimental results [38, 39] and Polák's model.

Polák's model

The Polák's model is an important extension of EGM model which was stimulated by the surface observation of copper single crystals [35]. The dislocation arrangement considered by Polák is shown in figure 34. The point defects are supposed to be generated homogeneously in whole volume of a PSB, i.e. both in dislocation-rich wall and in dislocation-poor channels. Two basic mechanisms of point defect formation are considered: mutual annihilation of two opposite edge dislocations moving on neighbour planes and non-conservative motion of screw dislocation [38].

The vacancies or di-vacancies are mobile at room temperature. They can migrate and annihilate when approaching sinks. Edge dislocations are perfect sinks for vacancies and their density is much higher in the walls than in the channels. The PSB-matrix interface is also very good sink for vacancies. Therefore, the quasi-equilibrium concentration of vacancies reaches its maxima in the middle of channels (see figure 34). This results in a flow of atoms and mass redistribution and two different morphologies (a matrix and a PSB) are predicted by Polák [35].

The flux of vacancies from the channels to the walls withing the PSB results in the accumulation of the mass in the channels and its diminution it the walls. The internal stress can be continuously relaxed only in the y-direction (see figure 34). This leads to the production of extrusions at the sites where channels intersect the surface and intrusions where the walls intersect the surface. The average spacing between the extrusions or intrusions at the early stage of PSM development is given by equation:

$$s = \frac{d}{cos\alpha} \tag{11}$$

where d is the mean spacing between the walls in the PBS and α is the angle between the primary Burgers vector and the intersection of the primary slip plane with the surface.

The mass redistribution between the PSB and matrix results in the build up of compressive stress in the PSB. This compressive stress is continuously relaxed by gliding dislocations, however, only it the direction of the active Burgers vector. This leads to the growth of an extrusion. Due to mass reduction close to PSB-matrix interface, the tensile stresses arise, which leads to growth of intrusion.

According to Polák's model, the steady state growth rate of extrusion height is given by equation:

$$\frac{dh_e}{dN} = \frac{2pL}{w} \sqrt{\frac{D_v \tau}{A}} \tanh \left(\frac{w}{2} \sqrt{\frac{A}{D_v \tau}} \right) \tag{12}$$

where p is vacancy production rate, L is the depth of the PSB below the surface, w is width of the PSB, D_v is diffusivity of vacancies, τ is the period of the cycle and A is vacancy annihilation rate. For more detailed information, see [35, 36, 38].
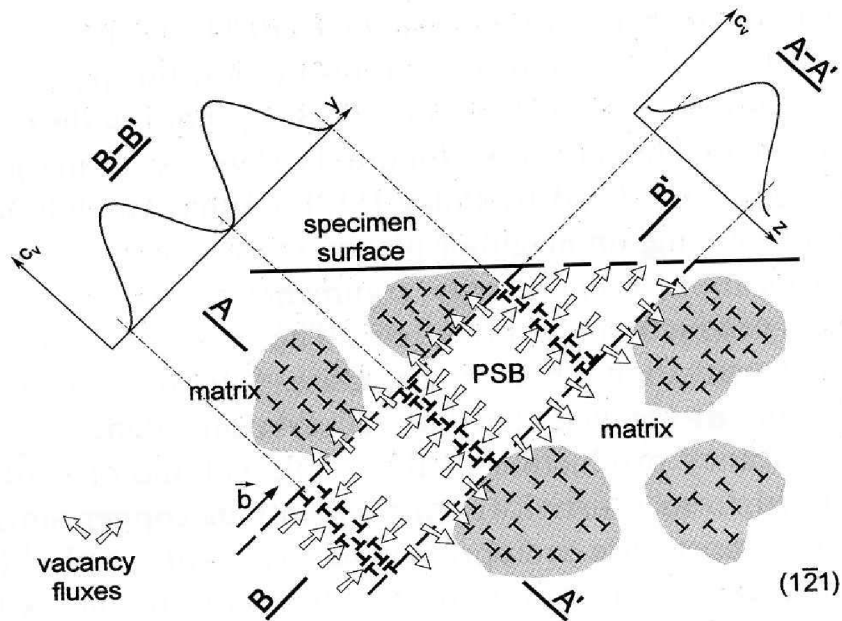

Figure 34: Polák's model of surface relief formation, schematic section through a crystal containing a PSB. [35]

2.3.4.3   Micromechanical models

Lin's model
The basic idea of this micromechanical model is that extrusion and intrusion are driven

by alternate specific micro-stress field in the PSB. Lin et al. calculated these micro-stress fields analytically and the relevant plastic shear strain accumulated during cycling in PSB was determined. The amount of cumulative plastic shear strain is connected to extrusion and intrusion size. This model was initially considered only for polycrystals, however recently it was also applied to single crystals [52].

2.3.5   Fatigue crack initiation

The fact that crack nucleation occurs in the surface layers of homogeneous materials was confirmed by many experiments. The cyclic strain localisation is also needed. This localisation can be connected with some effects such as eccentricity of load, bending loading or surface roughness or with surface relief formation (see section 2.3.4). The inhomogeneous materials make an exception, for example, for materials with strengthened surface layer the crack initiation often occurs at the interface between basic material and strengthened layer. Of course, the crack initiation stage is absent for materials containing cracks [35].

In the case of homogeneous materials, the nucleation sites predominately are:

- Persistent slip bands,

- grain boundaries,

- inclusion-matrix interface,

- precipitate-matrix interface.

The most common way of crack nucleation is in the PSB. Generally, the PSB density increases with number of cycles and stress or strain amplitude. The plastic strain localisation in intrusions and suitable dislocation arrangement along intrusions are necessary conditions for crack formation in PSB [35].

Experimental studies performed in high vacuum or in an inert gas atmosphere show that the slip-unslip mechanism can be reversible and new surfaces can be rewelded [53]. The role of environment is critical, the oxidising atmosphere enhances the irreversible slip-unslip mechanism leading to the formation of new surface, primary cracks. Two mechanisms of crack initiation are schematically shown in figure 35. The initiation of shallow surface crack by interconnection of half-elliptic intrusions along the PSB is shown in figure 35a. In figure 35b, the irreversible slip-unslip process originating form primary intrusion is shown. Both models distinguish between intrusion and a crack. The intrusion growth rate along primary plane is almost constant in constant cycling and depends on vacancy mobility and local strain amplitude. The stress and strain concentration increase with increasing depth of intrusion [35].

2.3.6   Fatigue crack growth

Fatigue cracks are usually divided into several categories [48].

1. **Small craks**. Crack smaller than approximately 1 mm are called "small". Three types of short crack can be distinguished:
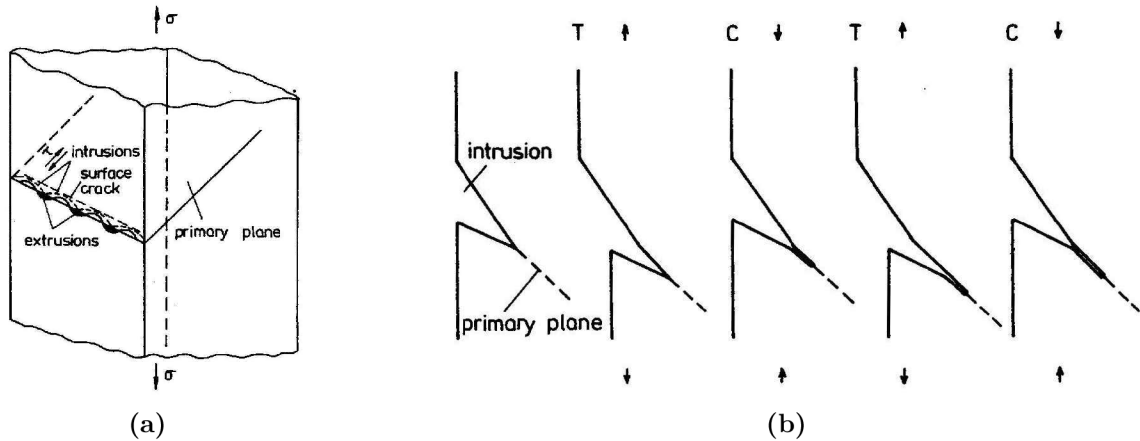
(a) (b)

Figure 35: Schematics of environment assisted crack initiation [35]: a) initiation from the row of intrusions, b) initiation by irreversible slip-unslip at the tip of intrusion

(a) **Physically small crack.** These cracks have a dimension under 1 mm. The difference between a long crack and small crack lies in a different closure stress.

(b) **Mechanically small cracks.** These crack have the same or smaller dimension than the plastic zone. Elastic fracture mechanics can not describe the stress and strain field around these crack.

(c) **Microstructurally small crack.** These crack have the same or smaller dimension than characteristic structural unit, e.g. grain size.

2. **Short craks** Definition of short cracks is based on fracture mechanics. Range of stress intensity factor (ΔK) at the tip of the short crack is lower than the threshold value (ΔK_{th}) .

3. **Long craks** $\Delta K > \Delta K_{th}$. In the certain interval of their length they follow the famous Paris-Erdogan law. Often The ASTM methodology is used for the long crack growth rate using CT specimens.

The initiation period and the short crack growth presents an important and very often decisive stage of fatigue life. The short crack propagation can be hardly solved using fracture mechanics which is usually used for long crack growth. If ΔK of a small crack exceeds ΔK_{th} its growth rate is often faster than the one measured by ASTM methodology.

The most of experimental data for small crack growth are compared with the master curve for long cracks in the growth rate vs. the stress intensity range coordinates, see figure 36. The stress intensity factor of small crack is calculated in the same way as for long cracks. In reality, stress and strain field at the small crack tip are different from the fields calculated using fracture mechanics for long cracks. Therefore, the crack growth rates are higher than for long cracks [54]. They have also higher scatter and the cracks grow at ΔK below the threshold value for long cracks. The small crack growth rates of individual cracks fluctuate considerably since structural barrier may stop the crack growth temporarily or even permanently [35, 54].
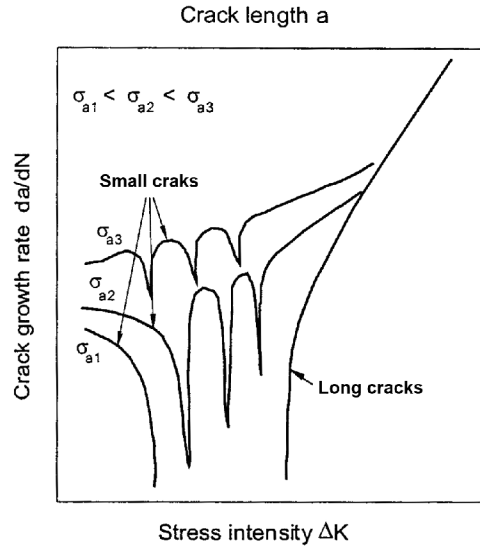
Figure 36: Schematic plot of crack growth rates in fracture mechanics representation [54]. For very small crack growth rates long crack curve approaches ΔK_{th}

The small crack kinetics can be solved by approach proposed by Polák [35]. This approach does not need the difficult stress and strain solution at the crack tip. Small cracks in most materials exhibit exponential dependence of growth on number of cycles [35, 36, 54, 55, 56]. The experimental data of Eurofer 97 steel is shown in figure 37a. This exponential dependence can be written as:

$$a = a_i . e^{k_g . N} \tag{13}$$
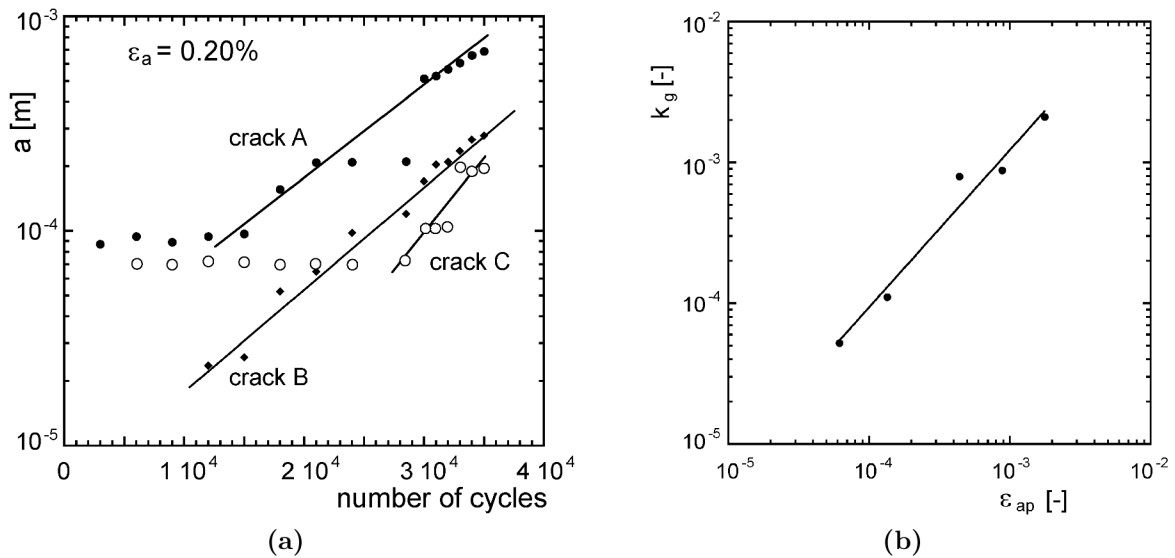
Figure 37: Fatigue life prediction using small cracks kinetics [55] a) measured data in the Eurofer 97 steel cycled with $\epsilon_a = 0.25\%$ b) the crack growth coefficient vs. plastic strain amplitude

where a_i is the extrapolated value of the crack length to the zero cycle, N is number of cycles and k_g is the crack growth coefficient. The increment of crack per one cycle can be obtained by derivation of equation 13:

$$\frac{da}{dN} = a_i.e^{k_g.N}.k_g = k_g.a \tag{14}$$

According to equation 14, the dependence of the crack growth rate on the crack length a is linear. It is assumed that the crack growth coefficient k_g depends only on plastic strain amplitude:

$$k_g = k_{g0}\epsilon_{ap}^{d} \tag{15}$$

where k_{g0} and d are coefficient which can be found for most of materials. This dependence for Eurofer 97 steel is shown in figure 37b.

The usual fatigue life time curves (Wöhler and Manson-Coffin) are suitable for the fatigue life prediction for the smooth specimens. The Paris-Erdogan law gives a possibility to predict long fatigue crack growth rate and thus to predict the residual fatigue life for a body containing a long crack. Polák's analysis offers an option how to determine residual fatigue life of specimens containing small cracks without difficult determination of stress and strain fields at the crack tip.

3 Experiment

3.1 Materials

In this work, fatigue properties of three steels strengthened by fine oxide dispersion are studied. These materials are produced by powder metallurgy in small quantity resulting in small size and small number of specimens Preparation of the three materials differs in some details. The chemical composition of these steels is shown in table 3. All materials contained the same amount of Y_2O_3 particles and belong to group of materials with reduced activation. Basic tensile properties are given in table 4. The Young modulus E was measured from the slope of elastic part in the first half–cycle of the hysteresis loop. Yield stress $R_{p0.2}$ was measured in the first cycle using specimens cycled with high strain amplitudes. Ductility was found in literature.

3.1.1 ODS Eurofer steel

The ODS Eurofer steel batch used in this study was produced by *Plansee Holding AG* in the form of a hot rolled plates, with a final thickness of 17 mm. Yttrium was added in a form of fine oxide particles. The chemical composition of this material is given in table 3. The final heat-treatment applied to the material was: annealing at 1100 ℃ for 30 min, air-cooling, tempering at 750 ℃ for 2 hours, air cooling. The material was supplied as a block of 16 × 32 × 45 mm. Twenty and twelve specimens were prepared in longitudinal (L) and transverse directions (T), respectively.

3.1.2 14Cr ODS ferritic steel produced in CEA

The first variant of 14Cr ODS ferritic steel studied in this work was finalised in the CEA (Commissariat à l'énergie atomique, Saclay, France) in 2008. The first step, the preparation of a metal powder and an yttrium powder was performed by the Austrian company *Plansee Holding AG*. In the CEA, the resulting powder was degassed at 300 ℃ and consolidated by hot extrusion at 1100 ℃, air-cooled and then annealed at 1050 ℃ for 1 hour. The chemical composition is given in table 3. This variant of ferritic steel

Table 3: Chemical composition of studied steels in wt. %

	Cr	W	Ti	Mn	V	Ta	C	O	Y_2O_3	Fe
Eurofer ODS	8.9	1.1	-	0.47	0.2	0.081	0.11	0.201	0.3	rest
the CEA steel	13.65	1.17	0.3	0.33	-	-	0.05	0.06	0.3	rest
the EPFL steel	14	2	0.3	-	-	-	0.067	0.38	0.3	rest

Table 4: Basic mechanical properties

	E [GPa]			$R_{p0.2}$ [MPa]			A [%]		
	RT	650 ℃	750 ℃	RT	650 ℃	750 ℃	RT	650 ℃	750 ℃
ODS Eurofer	2.09	1.27	1.02	1020	380	190	20 [19]	30 [19]	33 [19]
CEA steel	2.09	1.42	–	960	440	–	23 [30]	25 [30]	23 [30]
EPFL steel	2.06	1.42	1.15	1070	480	300	6 [57]	–	4.2 [57]

is called simply "CEA steel" in following parts of this work. The material was supplied as a cylinder with diameter of 15 mm with length of 29 mm, 8 specimens parallel to the extrusion direction were prepared. These specimens were used for the study of cyclic stress – strain response and for determination of the number of cycles to failure at RT, 650 ℃ and 750 ℃.

Bigger batch of this material was supplied in year 2010. It was possible to prepare sixteen specimens (also parallel to the extrusion axis). Half of them were used for fatigue test at RT and second half were used for small fatigue crack growth measurement.

3.1.3   14Cr ODS ferritic steel produced in EPFL

The second variant of 14Cr ODS ferritic steel studied in this work was produced at the EPFL (École Polytechnique Fédérale de Laussane, Switzerland). The powder was prepared by planetary ball milling for 50 hours in H_2. The heat treatment consisted of degassing at 800 ℃ for two hours followed by a HIPing at 1150 ℃ and 200 MPa and final annealing at 900 ℃. The chemical composition is given in table 3. This variant of ferritic steel is called simply "EPFL steel" in following parts of this work. The material was supplied as a block of $20 \times 20 \times 28$ mm. 16 specimens were prepared.

3.2   Standard fatigue tests

3.2.1   Specimens

Due to limited amount of material produced by powder metallurgy and in order to maximise the number of the specimens, small specimens were prepared according to the design developed within the framework of the "Small Specimen Testing Technology" program [58]. These specimens had a diameter of 2 mm and a gauge length of 7.6 mm and they were used for standard fatigue tests, see fig. 38. Inconel "holders" were used for fixing of specimens to the grips of fatigue machine. This kind of geometry was used for the EPFL steel, the ODS Eurofer steel and the CEA steel supplied in 2008. Slightly different geometry was used for the batch supplied from the CEA in 2010. Diameter of specimens
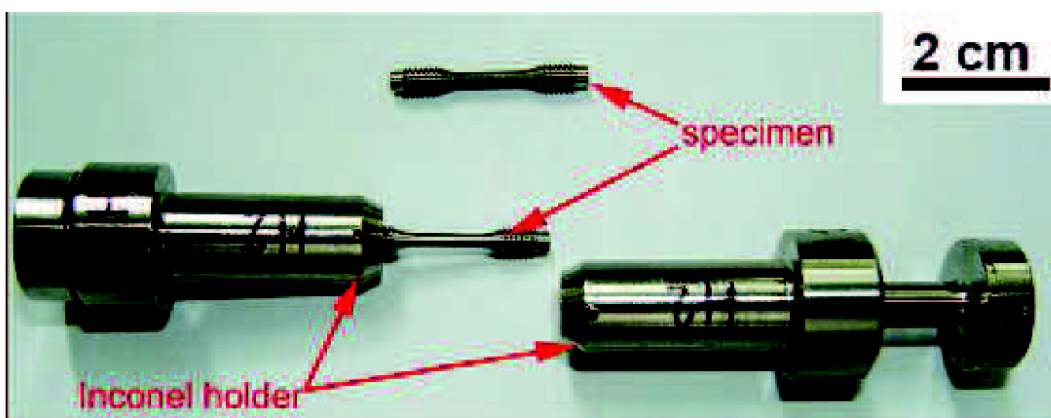

Figure 38: Specimen and Inconel grips

was extended to 2.3 mm as well as gauge length to 9 mm. Gauge length of all tested specimens was mechanically and electrolytically polished.

3.2.2   Methodology

The specimens were cycled in MTS 880 servohydraulic machine controlled by the MTS FlexTest electronics. The fatigue tests were performed in symmetrical cycle with constant total strain amplitude ε_a (R_ε = -1). The controlling parameteris (P, I, D) was adjusted to used specimen geometry very well and strain amplitude was kept constant precisely during tests, see figure 40. Force was measured by a load cell and strain by an extensometer with ceramic rods attached to the specimen gauge length, see figure 39. Strain rate equal to 2×10^{-3} s^{-1} was kept constant during cycling. Room temperature (RT) in laboratory was kept constant (23 °C) during testing. This arrangement (figure 39) is also applicable for testing at elevated temperatures, because the measuring part of the extensometer is placed outside of a furnace. The specimen heating is reached using three-zone furnace. Temperature in each zone was controlled by a thermocouple attached to grips and fourth thermocouple was attached to the specimen. Grips were cooled by water. Force and strain were recorded during cycling, subsequently they were recalculated to engineering stress and strain. Plastic strain amplitude was determined as half-width of hysteresis loop.
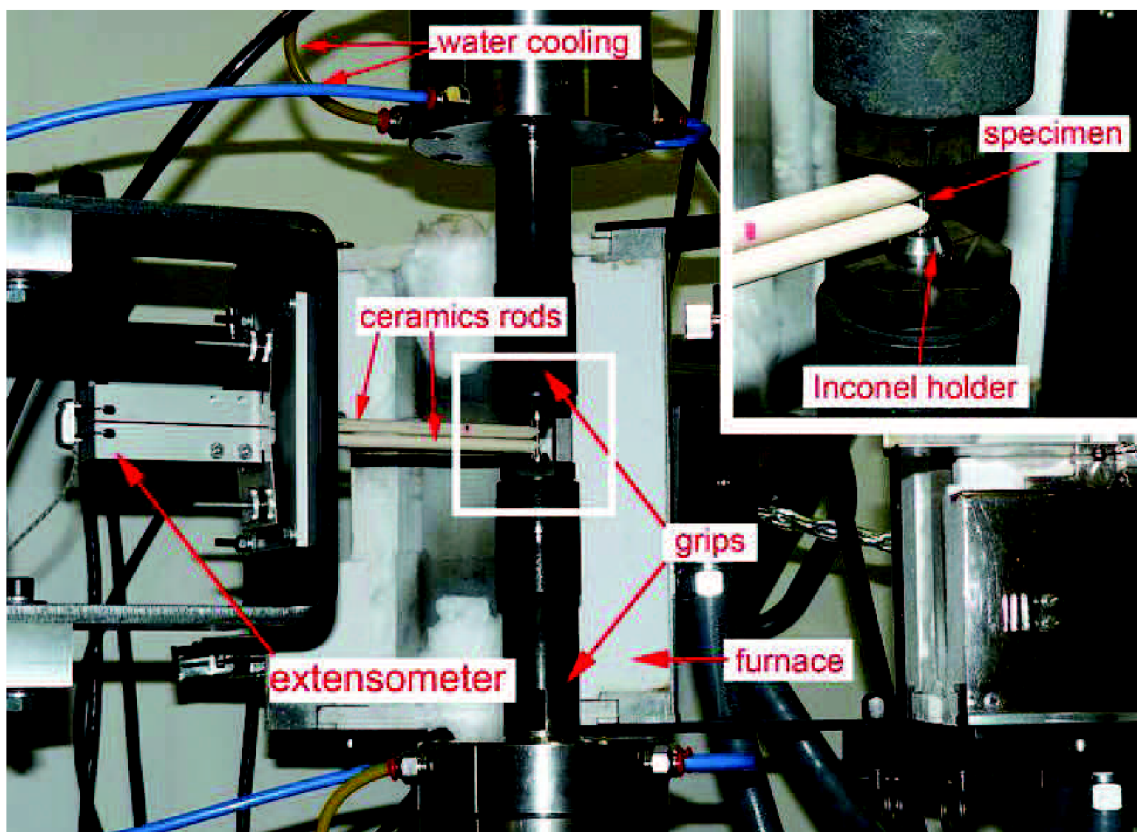

Figure 39: Experimental arrangement allowing experiments at room and elevated temperatures. Attachment of ceramic rods to the specimen is shown in detail
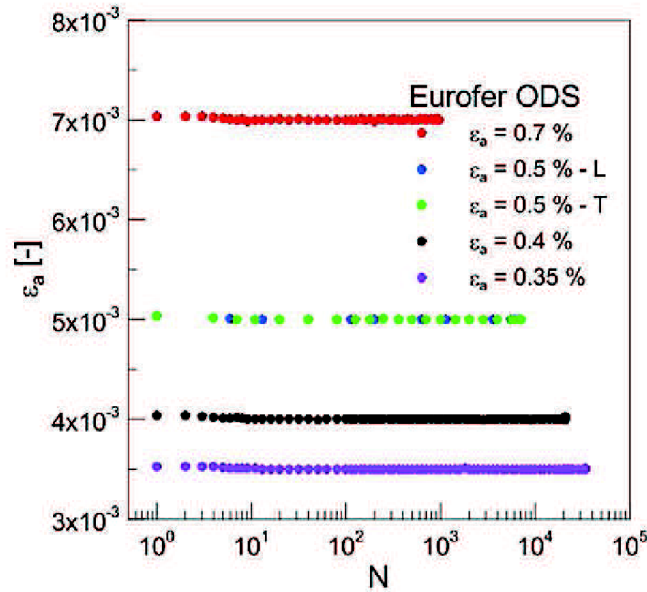
Figure 40: Verification of strain control quality: strain amplitude vs. number of cycles

3.3   Small crack growth measurement

Kinetics of small fatigue crack growth was measured in the CEA steel and in the ODS Eurofer steel. It was not possible to measure it in the EPFL steel, because of lack of supplied material.

3.3.1   Specimens

The geometry described in previous section was used. Moreover, the shallow notch was fabricated on the gauge length, see figure 41. The notch surface was polished mechanically, electrolytically and in some cases the final polishing was performed using 0.25 μm diamond paste. This notch causes stress concentration which is sufficient for initiation of main crack in this area. Typically, only one crack initiated in the CEA steel, which was found out during surface observation of specimen after failure, see section 4.7. Therefore, pre–cracks were prepared in polished area using focused ion beam (FIB) technique to ensure that the crack will propagate in observed area, see figure 42b. Parameters of ion beam were set to prepare a crack perpendicular to the stress axis with semicircular depth profile in both studied material. The notch length were changed during experiments. The starting value
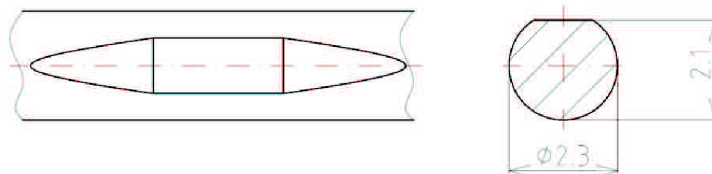
Figure 41: Scheme of the gauge part of the specimen with a shallow notch

of pre–crack length was chosen as 100 μm. According to first results, pre–crack length was shortened to values from 50 to 75 μm.

3.3.2 Methodology

The fatigue tests were regularly interrupted and two pre–cracks were photographed using a light microscope with long focal distance, which was attached to the machine frame, see figure 42a. Micrographs were subsequently analysed and a dependence of crack length on the number of cycles was obtained. The crack length a was defined as half length of the surface length crack projection into the direction perpendicular to the specimen axis. An example of growing crack in the ODS Eurofer steel is shown in figure 42b.

(a)   (b)
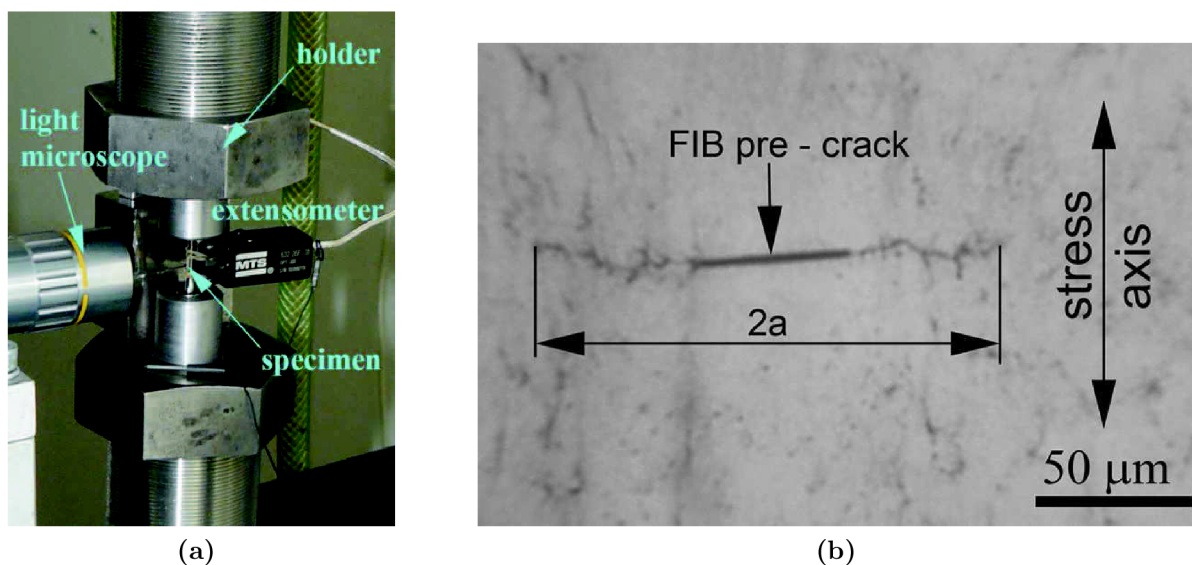
Figure 42: a) MTS 810 adapted for short crack growth measurement; b) typical optical micrograph of growing crack with marked length and stress axis

3.4 Microscopy

Specimens for transmission electron microscopy were prepared by standard procedure consisting of spark cutting, mechanical polishing and disc cutting. The final electropolishing was carried out at temperature of 14 °C and 90 V using 5% perchloric acid and 95% acetic acid. Philips CM12 TEM was used for microstructural study. Surface observations and EBSD analysis were performed with TESCAN Lyra 3 XMU scanning electron microscope. The disorientation of 10 degree was chosen as a definition of high angle boundaries.

4 Results

Results achieved in this work are described in this chapter. It starts with verification of experimental setup which was adapted for small specimen testing. Description of microstructure of studied materials in as – received state was characterised using TEM (transmission electron microscopy) and SEM (scanning electron microscopy). Cyclic hardening/softening curves, cyclic stress–strain curves and the fatigue life curves were determined at room temperature, 650 and 750 ℃. This section is followed by microstructural description after fatigue loading. Changes in microstructure due to fatigue loading are highlighted if possible. This chapter is finished by SEM observation of specimen surface after fatigue loading in all studied steels and by small fatigue crack growth rate measurements in the ODS Eurofer steel and the CEA steel.

Since materials were delivered free of charge, producers required certain experiments to do. Producers (the CEA and the EPFL) requested information about fatigue behaviour at RT and at elevated temperatures in high strain amplitude region. For this reason, together with low quantity of received materials, fatigue curves contain only small number of points and test with low strain amplitude to determine longer fatigue life were not performed. This fact complicates statistical analysis and all parameters of fatigue curves are burdened with non–negligible statistical standard deviation.

4.1 Verification of experimental set up

At first, it was necessary to verify if geometry of specimens and original machine set up (section 3.2.2) have any influence on cyclic properties. The Eurofer 97 steel was used for this purpose. Specimens of the geometry described in section 3.2.1 and one specimen of 8 mm in diameter were prepared from the Eurofer 97 steel and fatigue experiments
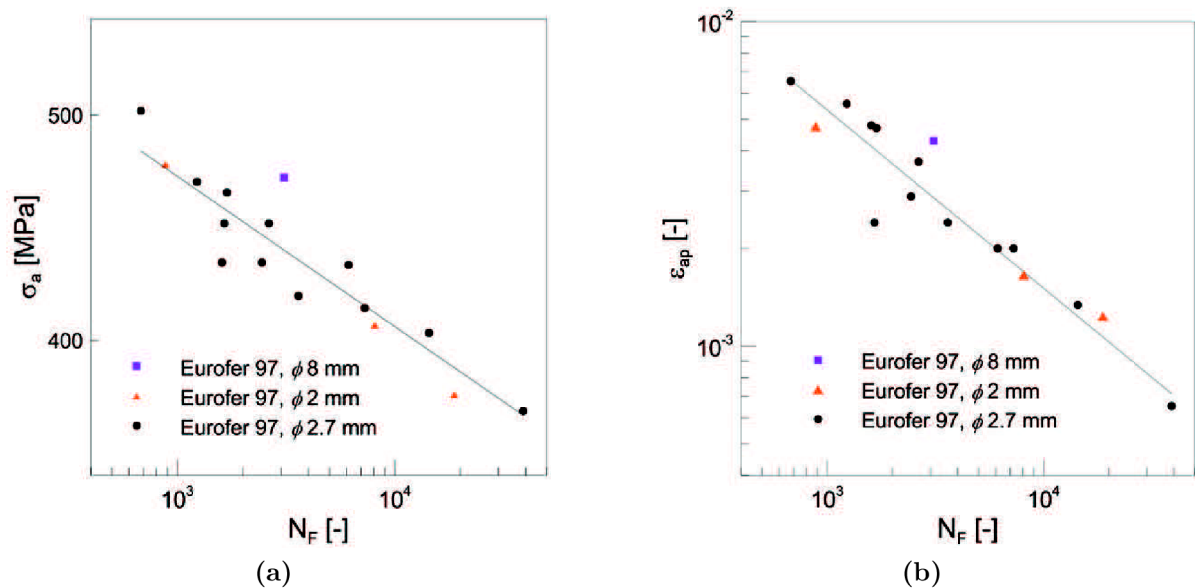

(a)   (b)

Figure 43: Fatigue results of the Eurofer 97 steel obtained with different specimen geometries and speciem set – ups, black dots were taken from [16]; a) Wöhler plot; b) Coffin-Manson plot

with constant strain amplitude were performed. Three fatigue experiments were carried out with specimens of 2 mm in diameter and one with specimens of 8 mm in diameter. Results are plotted in Wöhler and Coffin-Manson plots in figure 43. For the comparison, data by Marmy and Kruml [16] measured on specimens with diameter of 2.7 mm are plotted in figure 43 too. The 8 mm specimens appears to exhibit slightly higher strength and better resistance to cyclic plasticity then [16]. On the other hand, results obtained with 2 mm specimens follow data measured in [16] very well. Only the lowest strain amplitude exhibits a bit lower life time in Wöhler plot. Nevertheless, scatter of measured data is reasonable. It was concluded that fatigue life measured with specimens of 2 mm in diameter is the same as fatigue life measured with specimens of other geometry. Similar experiments were performed by Hirose [59]. Specimens from another reduced activation steel with diameter of 6 mm and 1.25 mm were tested. No influence of specimen size on mechanical properties was found too.

Moreover, the studied materials have fine microstructural unit, typically under 1 μm, which suppresses the effect of specimen size on obtained results. Thus, it was proven that using miniaturised specimens and adapted experimental setup, it is possible to measure reliably mechanical properties of studied steels.

4.2   Microstructure of as – received state

The microstructure of as – received state was studied by TEM, SEM and EBSD (electron backscattered electron diffraction) techniques. Observations revealed a fine microstructure in all cases. Oxides particles can be seen only in TEM dark field mode, an example is shown in figure 44b. The amount and mean size of oxides is the same for all materials, nevertheless not much is known about the homogeneity of oxide particles distribution. Since it is experimentally difficult to assess the distribution of nanometric particles in the macroscopic sample, it cannot be excluded that the quality of powder mixing was different for the three materials. Some differences in microstructure among studied materials, especially, in grain size and geometry were found.

4.2.1   The ODS Eurofer steel

Majority of the volume of the ODS Eurofer steel is filled by approximately equiaxed grains/subgrains (figure 44a and 45a). At some place, elongated rests of tempered martensitic laths are visible. The thickness of the laths is about 500–700 nm. Dislocations are present in high density. Grain boundaries are decorated by carbides of typical dimension of 100 nm.

Defects present in the microstructure were found and subsequently analysed. An example of micrograph used for this analyse is shown in figure 45a. Homogeneously distributed voids with typical size of 0.2 μm were detected in microstructure. Larger defects of size of around 0.8 μm were found, although they are present in much smaller quantity. The EBSD analysis confirmed fine structure of the ODS Eurofer steel. Moreover, areas of size of about 5 μm with similar crystallographic orientation were found. The EBSD micrographs taken from directions perpendicular to the rolling direction (T) and parallel to the rolling direction (L) are shown in figures 45c and 45d. Microstructure of rolled
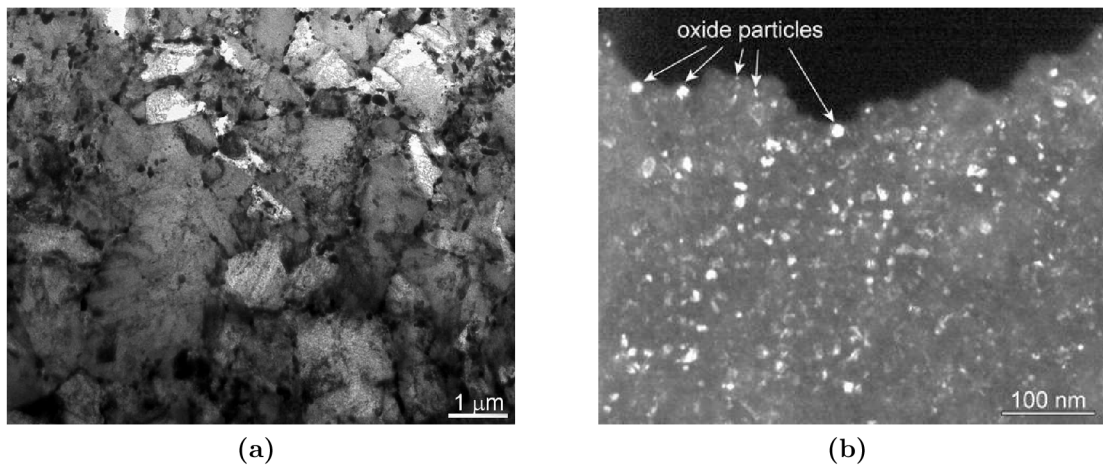
Figure 44: Microstructure of the ODS Eurofer steel: a) martenisitic laths and carbides (TEM - bright field); b) fine oxide particles (TEM - dark field)
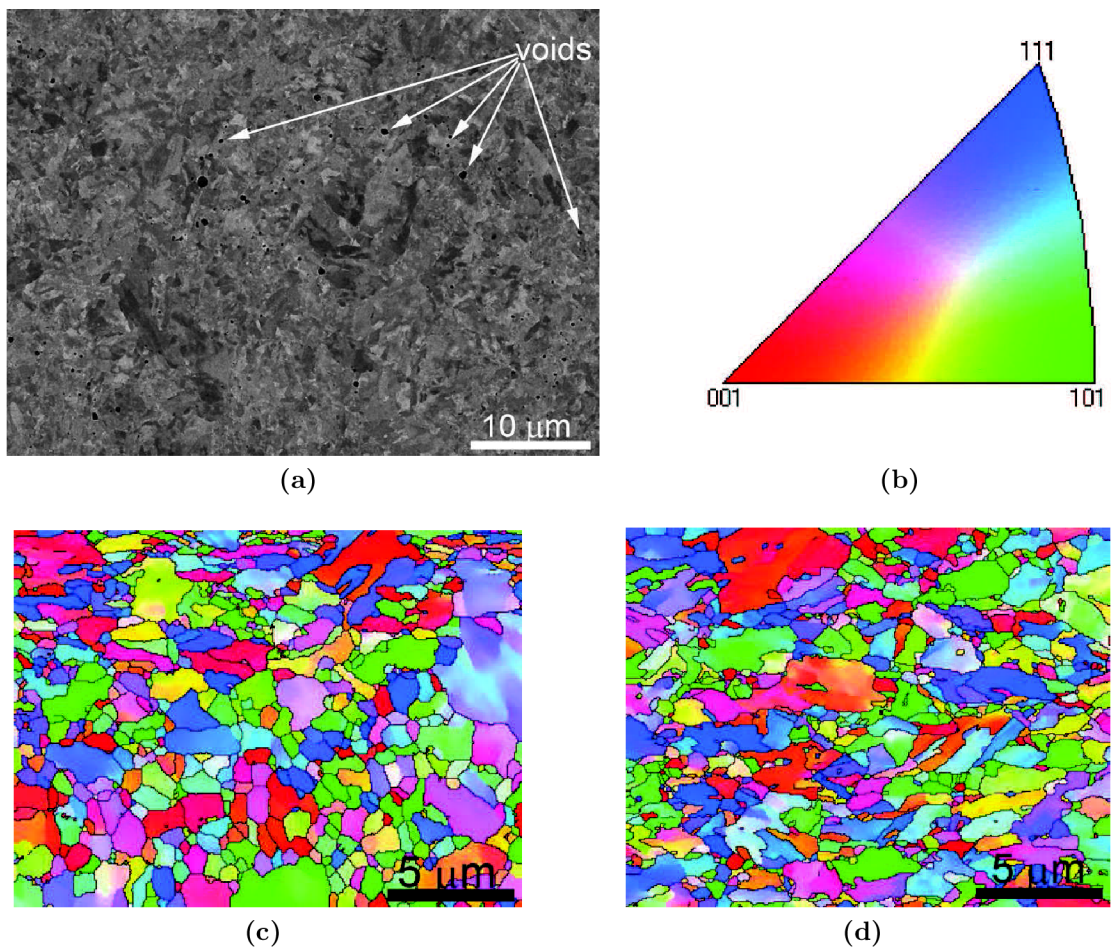
Figure 45: a) Microstructure of the ODS Eurofer steel (SEM, BSE mode), individual grains and voids are visible; b) color key of crystallographic orientations used during EBSD analysis; c) EBSD micrograph in L direction; d) EBSD micrograph in T direction

materials is often formed by elongated or pancake shaped grains. As shown especially in figure 45c, it is not the case here. The martensitic transformations and subsequent tempering result in almost equiaxed grains and subgrains. Very small dissimilarities between L and T directions can be found after careful analysis of micrographs, nonetheless, they do not have influence on fatigue behaviour, which is shown later.

4.2.2   The CEA steel

Cross section perpendicular to the extrusion direciton is shown in figure 46a. The equiaxed grains with the average size of 0.49 μm $\pm$ 0.2 μm were determined from TEM micrographs of the microstructure of the CEA steel in this cross–section. The dislocation density in
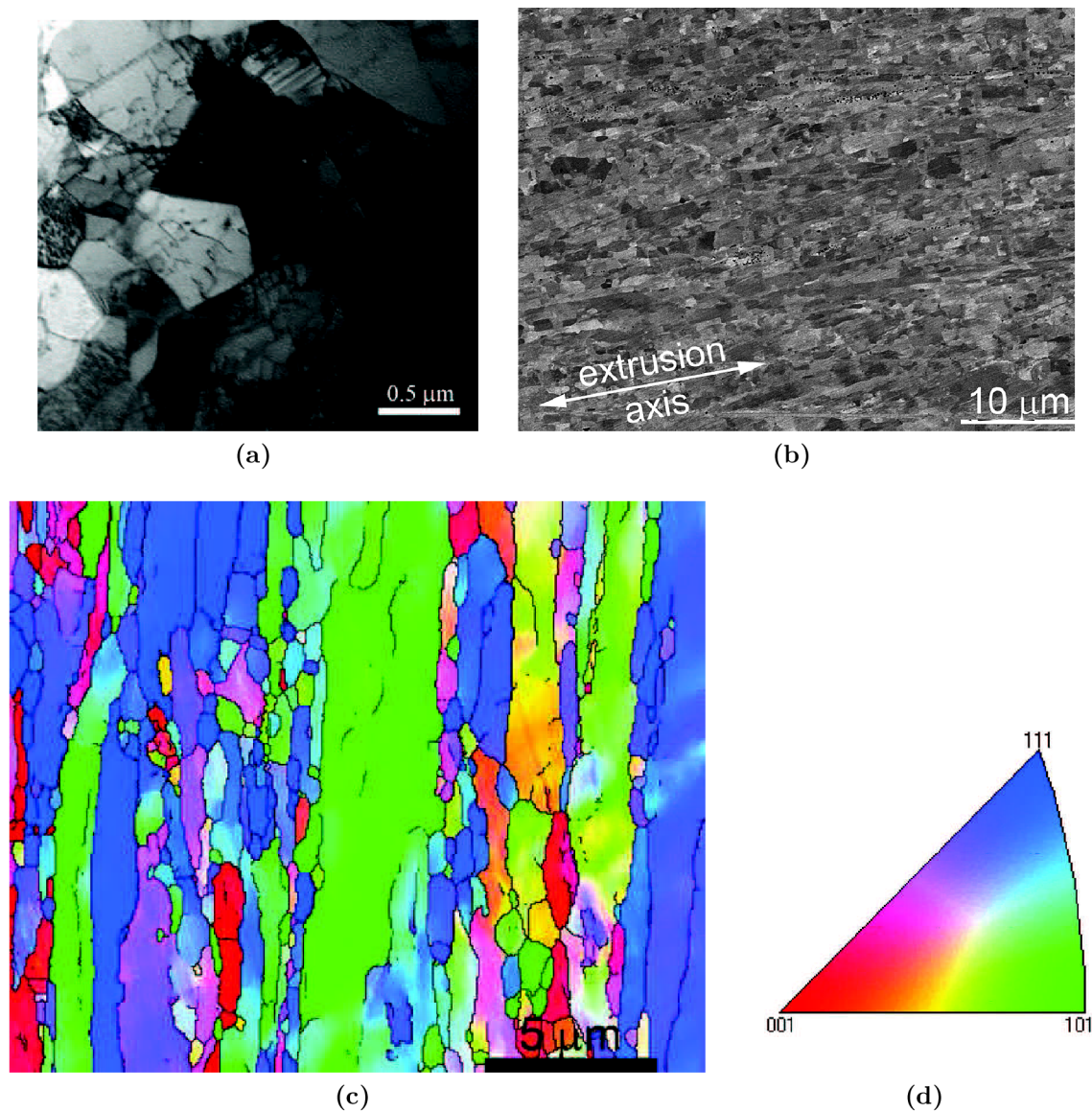
Figure 46: Microstructure of the CEA steel: a) TEM micrograph; b) BSE micrograph; c) EBSD micrograph; d) EBSD color key

grains is high. The elongated grains in the extrusion direction and fine voids are shown in figure 46b. Voids are arranged in rows mostly parallel to the extrusion direction. Their typical size is of about 0.11 μm and at least one defect of size of 1 μm was found in area of size 100 μm × 100 μm. The elongated microstructure is perfectly visible in EBSD micrograph, see 46c. The length of grains is up to 20 μm in extrusion direction.

4.2.3   The EPFL steel

The microstructure with bimodal grain size distribution was found in the EPFL steel. The microstructure consisted of regions with small grains with the average size of 0.34 μm ±˜ 0.18 μm and of big grains with size of about 3 μm. Areas with small grains occupy only about 15 % of volume. The dislocation density in both grain types is high. Regions

(a)   (b)

(c)   (d)
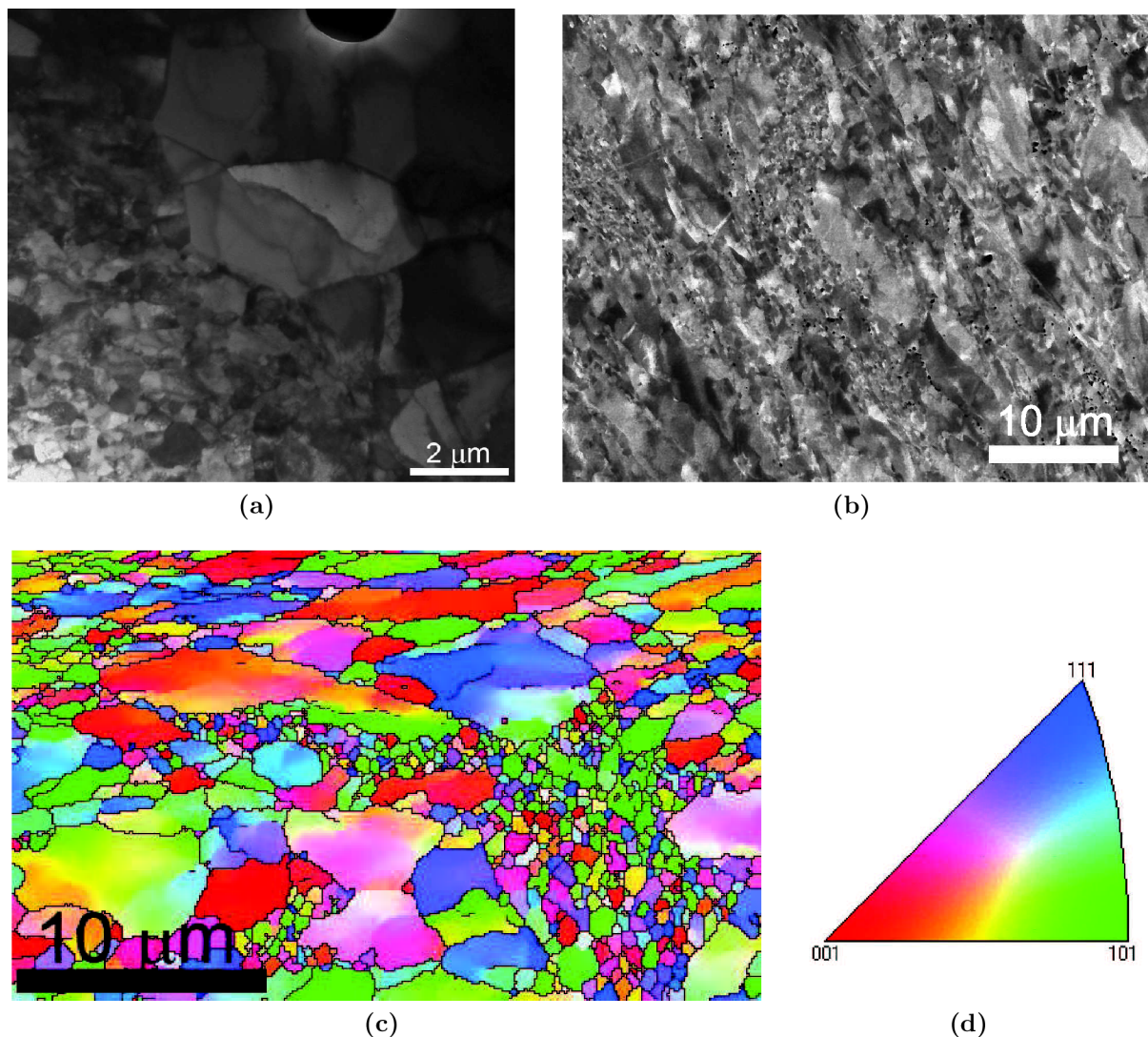
Figure 47: Microstructure of the EPFL steel: a) TEM micrograph showing regions of small and big grains, black hole at the top is a void; b) BSE micrograph; c) EBSD micrograph; d) color key used for EBSD

of small and big grains are clearly visible in figures 47a-c as well as microstructural defects, figure 47b. Microstructural defects, voids, are situated mostly at interfaces between regions of big and small grains. Their typical size is of about 0.2 μm, and no bigger defects than 0.8 μm were found in structure. The EBSD micrograph (figure 47c) confirms bimodal structure as well as ratio between individual regions.

4.2.4   Summary

Very fine microstructure was revealed in all studied steels, but some differences were detected. The characteristics of microstructural unit and void size are given in table 5. The major differences can be summarised in following points:

- The matrix of the tempered ferritic–martensitic ODS Eurofer steel consists of decomposed martensitic lath, which are decorated by carbides.

- The pure ferritic matrix was found in the CEA steel. Equiaxed grains were found in section perpendicular to the extrusion axis, grains are elongated in section parallel to the extrusion axis.

- The microstructure with bimodal grain size distribution is formed in the purely ferritic EPFL steel.

- All three materials contain submicrometric voids.

Table 5: The grain and defect size of studied materials

	matrix	grain size [μm]	grain characteristics	mean void size [μm]	max. void size [μm]	Number of voids in μm^2
ODS Eurofer	tempered martensite	0.72 ± 0.2	equiaxed, subgrains	0.21	0.8	0.07
CEA steel	ferritic	0.49 ± 0.2	elongated	0.11	1.0	0.26
EPFL steel	ferritic	0.34 ± 0.18 ~3	equiaxed, bimodal	0.2	0.8	0.2

4.3   Cyclic hardening/softening curves

The stress-strain data in selected cycles were stored during cycling allowing plot of individual hysteresis loops and subsequent determination of cyclic hardening/softening curves. The tests were performed in constant total strain amplitude mode, therefore cyclic hardening/softening curves were obtained in two representation, specifically in $\sigma_a = f(N)$ and in $\varepsilon_{ap} = f(N)$ representations. Values of σ_a and ε_{ap} measured at the half-life were plotted in fatigue life curves.

4.3.1   ODS Eurofer steel

It was supposed that oxide particles could prevent undesirable cyclic softening, which is observed inferritic-martensitic steels [16]. The cyclic softening curves obtained at RT are plotted in figure 48. Obviously, the oxide particles strengthen material substantially, nevertheless, cyclic softening is observed at all testing amplitudes. The cyclic softening rate depends on applied loading. Higher strain amplitude results in higher softening rate. For instance, softening rate was of about 65 MPa during 950 cycles in specimen cycled with the highest strain amplitude (0.7 %) and 36 MPa during 28000 cycles in specimen cycled with the lowest strain amplitude (0.35 %). Although softening size in ODS variant of the Eurofer steel is lower than in the Eurofer 97 steel [16], it indicates that oxide dispersion itself does not guarantee a stable cyclic behaviour and other microstructural aspects have to be taken into account.

The cyclic softening is documented in figure 49 too. Two hysteresis loops are plotted in figure 49a. It is obvious that the stress amplitude decreased with increasing number of cycles and also the loop became wider which means higher amplitude of plastic strain amplitude. Note that controlled total strain amplitude is kept very precisely during test, see figure 40. The cyclic softening is evident comparing tensile curve and cyclic stress –

(a)   (b)

Figure 48: The ODS Eurofer steel, cyclic softening curves at RT: a) in $\sigma_a = f(N)$ representation; b) $\varepsilon_{ap} = f(N)$
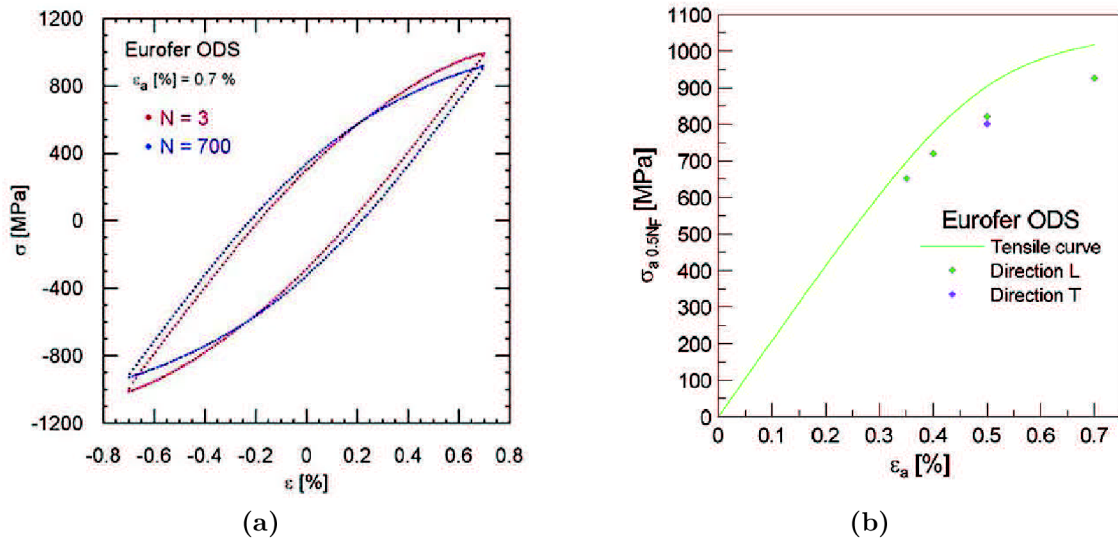
Figure 49: a) A hysteresis loop evolution during cycling; b) Tensile and cyclic stress – strain curves

strain curve, figure 49b. Cyclic data lies systematically under tensile curve, which again confirms cyclic softening. The dependence of softening rate on applied strain amplitude is documented too as well as negligible difference between L and T direction.

The cyclic softening is observed also at 650 °C and 750 °C, see figure 50 and 51 respectively. The softening rate at elevated temperatures is lower than at room temperature, but it was observed in all specimens. The softening rate increases with increasing strain amplitude and decreasing testing temperature. The cyclic softening is almost negligible at 750 °C in low amplitude region.

Figure 50: The ODS Eurofer steel, cyclic softening curves at 650 °C: a) in $\sigma_a = f(N)$ representation; b) $\varepsilon_{ap} = f(N)$

Figure 51: The ODS Eurofer steel, cyclic softening curves at 750 ℃: a) in $\sigma_a = f(N)$ representation; b) $\varepsilon_{ap} = f(N)$

4.3.2 CEA steel

The CEA steel exhibits stable cyclic behaviour after the first stabilising part taking less than one percent of life time at RT, see figure 52. The situation is different at 650 ℃. The slight cyclic hardening is observed in data representation shown in figure 53a, whilst stable behaviour is observed in second representation, figure 53b. Besides, the stress levels are still quite high for steel cycled at 650 ℃.
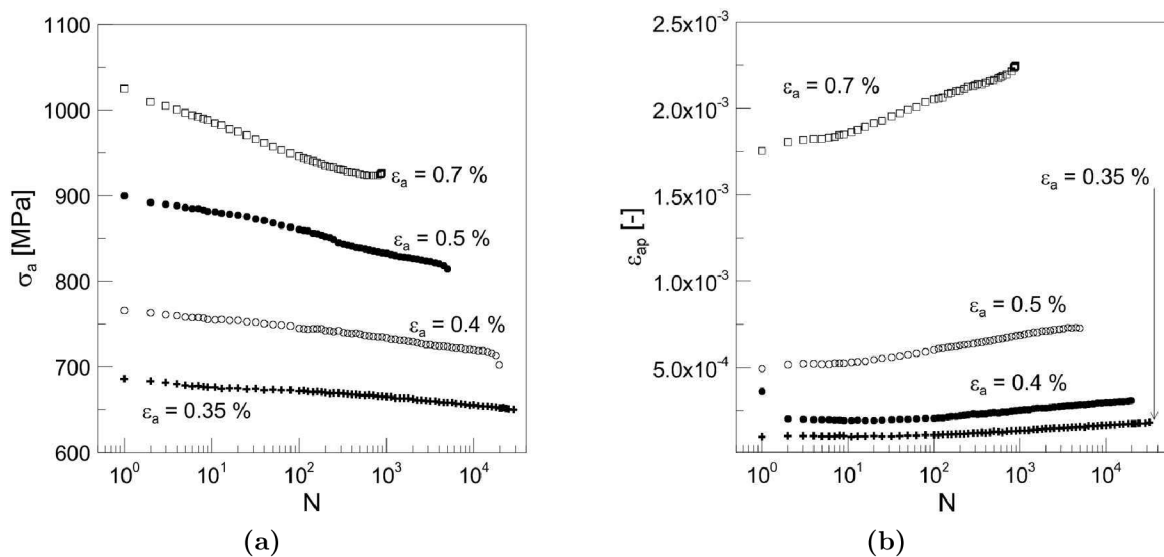

Figure 52: The CEA steel, cyclic softening curves at RT: a) in $\sigma_a = f(N)$ representation; b) $\varepsilon_{ap} = f(N)$

**Figure 53:** The CEA steel, cyclic softening curves at 650 °C: a) in $\sigma_a = f(N)$ representation; b) $\varepsilon_{ap} = f(N)$

4.3.3 EPFL steel

The evolution of σ_a and ε_{ap} with number of cycles for specimens prepared from the EPFL steel is shown in figure 54. Continuous softening for the highest amplitude and relatively stable behaviour for others strain amplitudes was observed at RT. The stress levels are the highest among studied steels. Slight cyclic hardening was observed at 650 °C. Cyclic hardening is not strong and it compensates a reduction of strength during first cycles. The evolution of ε_{ap} with number of cycles is stable across all tested amplitudes at 650 °C. Stable behaviour and slight cyclic softening were observed at the end of fatigue
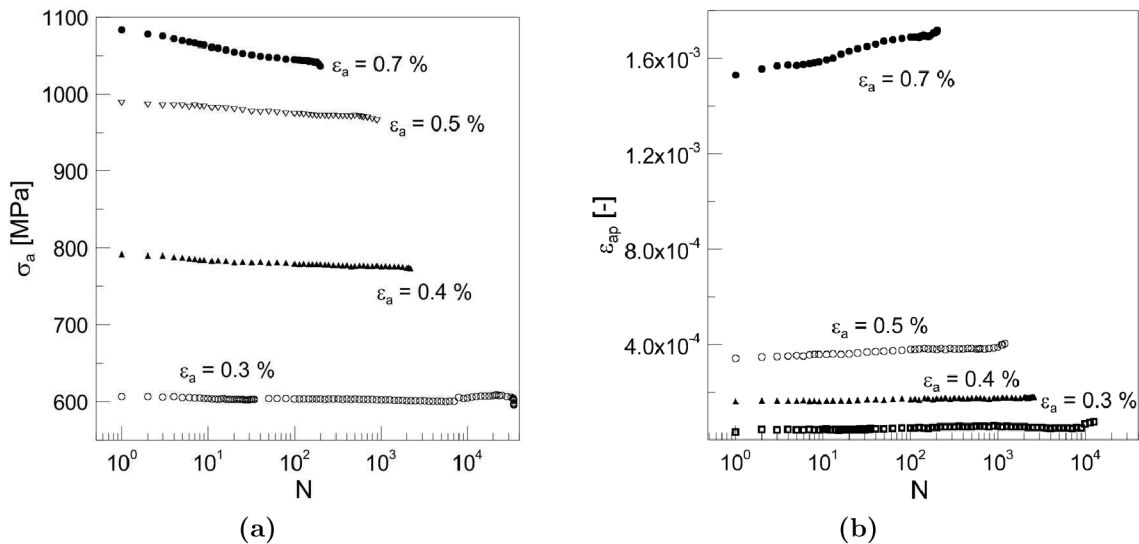
Figure 54: The EPFL steel, cyclic softening curves at RT: a) in $\sigma_a = f(N)$ representation; b) $\varepsilon_{ap} = f(N)$

life at 750 °C, see figure 56. The stress levels are relatively high for steels at such high temperature, nevertheless, the life time is the shortest.
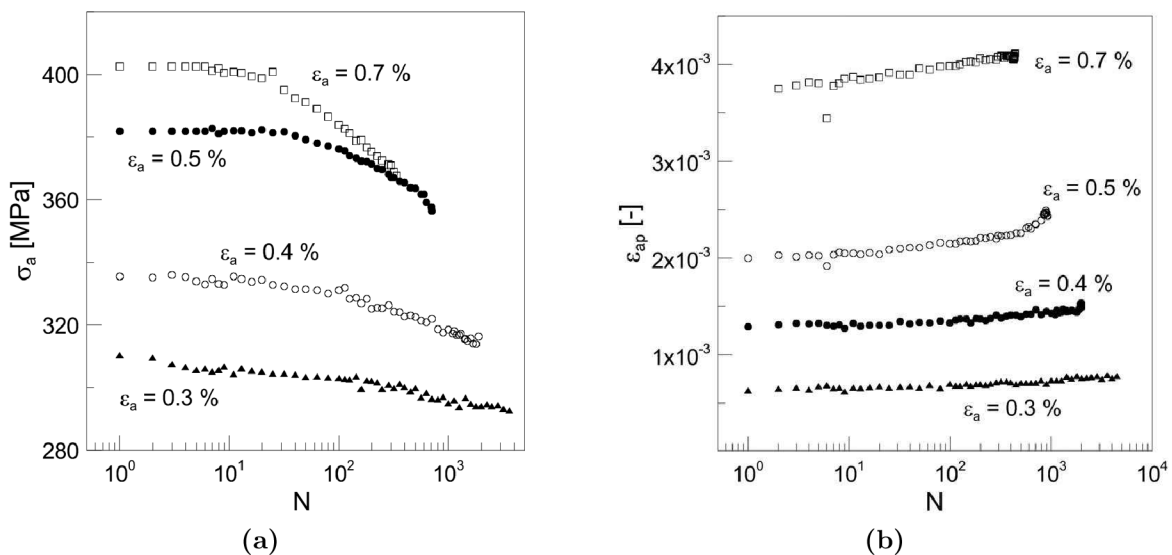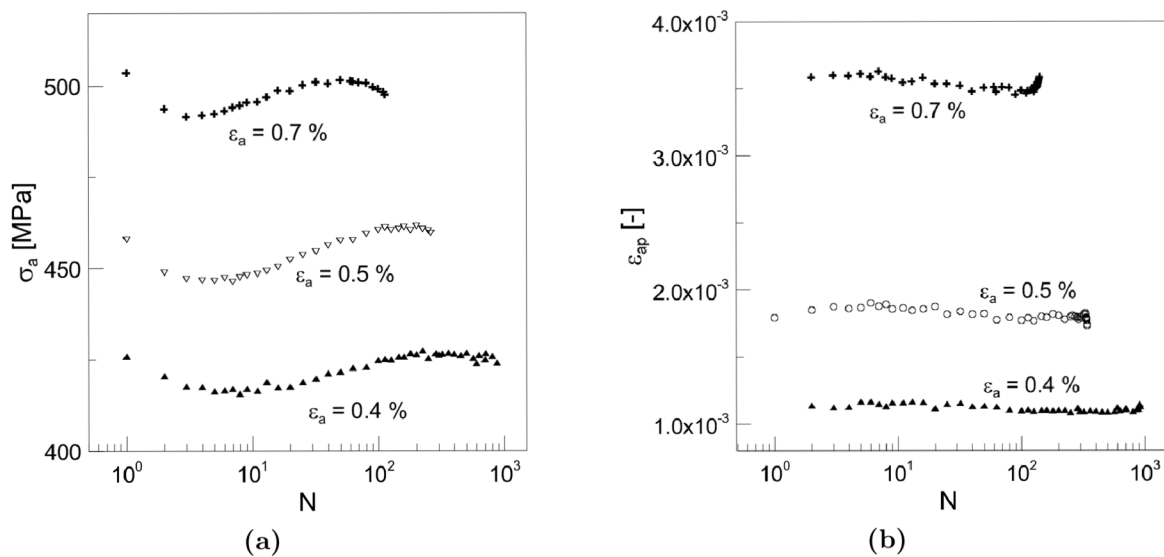

Figure 55: The EPFL steel, cyclic softening curves at 650 °C: a) in $\sigma_a = f(N)$ representation; b) $\varepsilon_{ap} = f(N)$

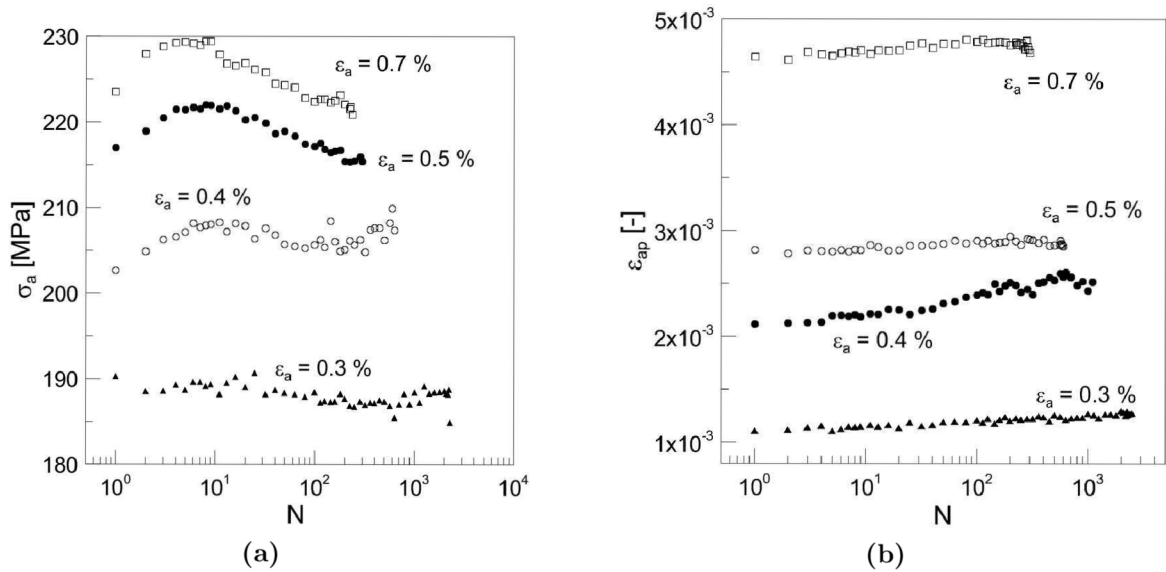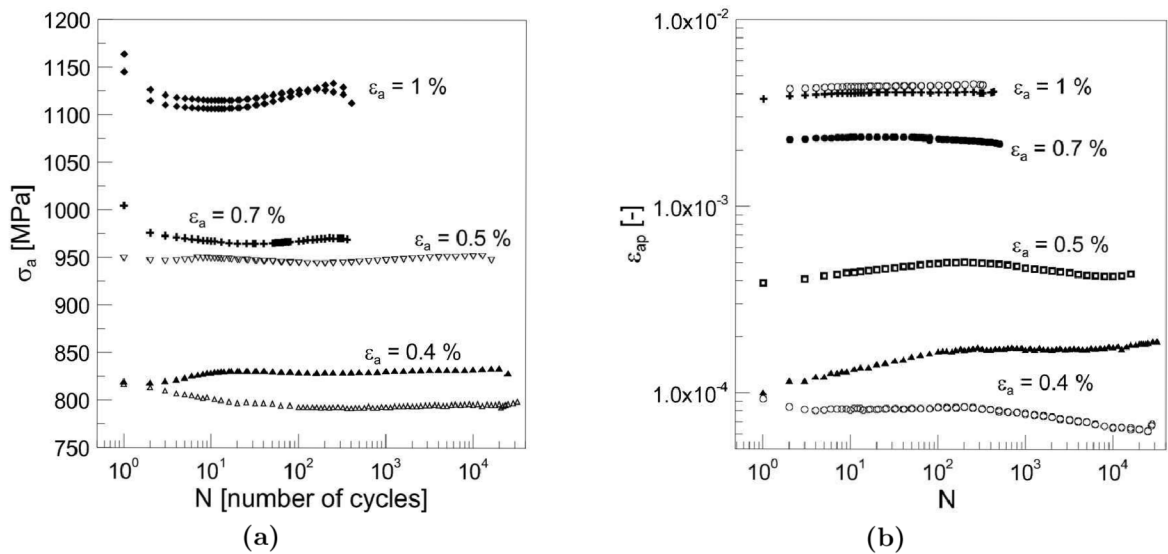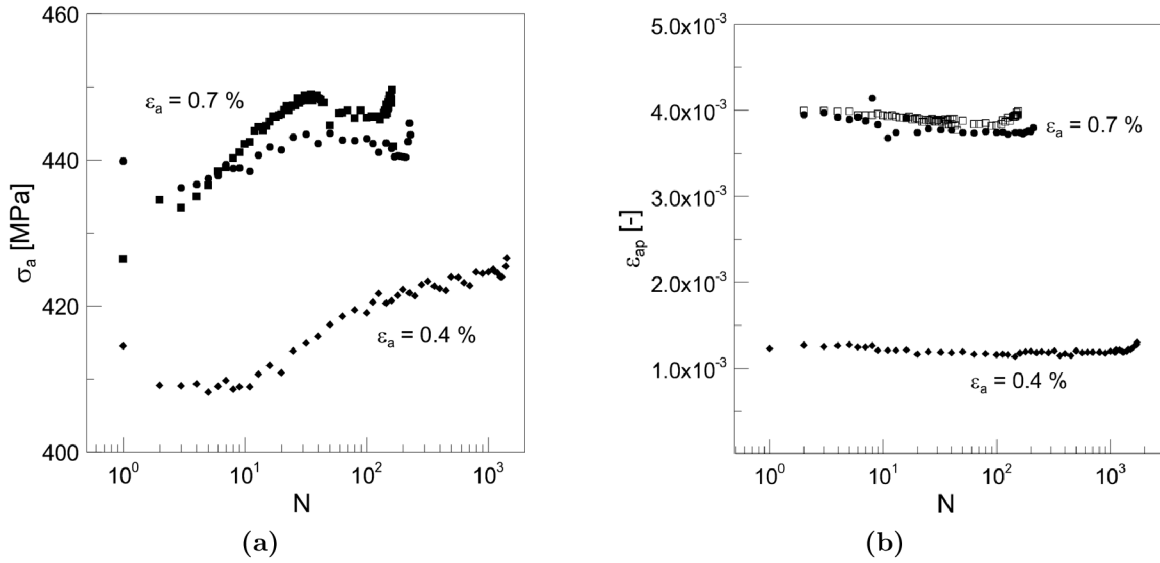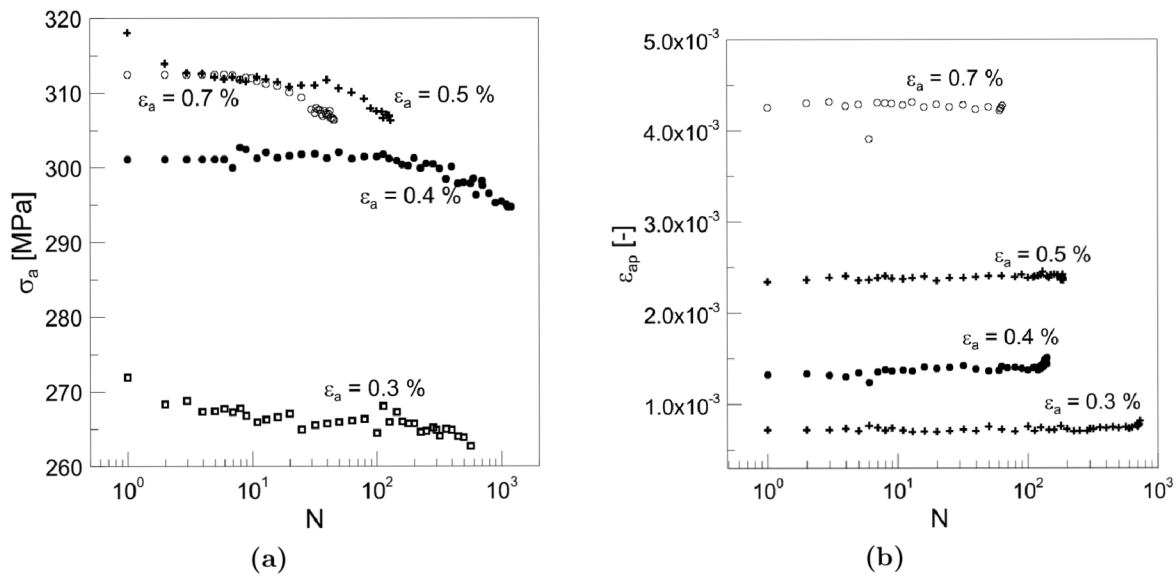**Figure 56:** The EPFL steel, cyclic softening curves at 750 °C: a) in $\sigma_a = f(N)$ representation; b) $\varepsilon_{ap} = f(N)$

4.3.4   Comparison of the ODS steels with the Eurofer 97 steel

Cyclic softening curves of all studied materials and of the Eurofer 97 steel are plotted in both representations in figure 57. The strengthening effect of oxide dispersion is obvious, stress levels are almost doubled comparing non – ODS with ODS steels. Moreover, cyclic softening is suppressed by oxides but it still persists for some experimental conditions especially in the ODS Eurofer steel. The EPFL steel possesses the highest strength for the highest strain amplitude. The strength of ODS ferritic steel is very similar under
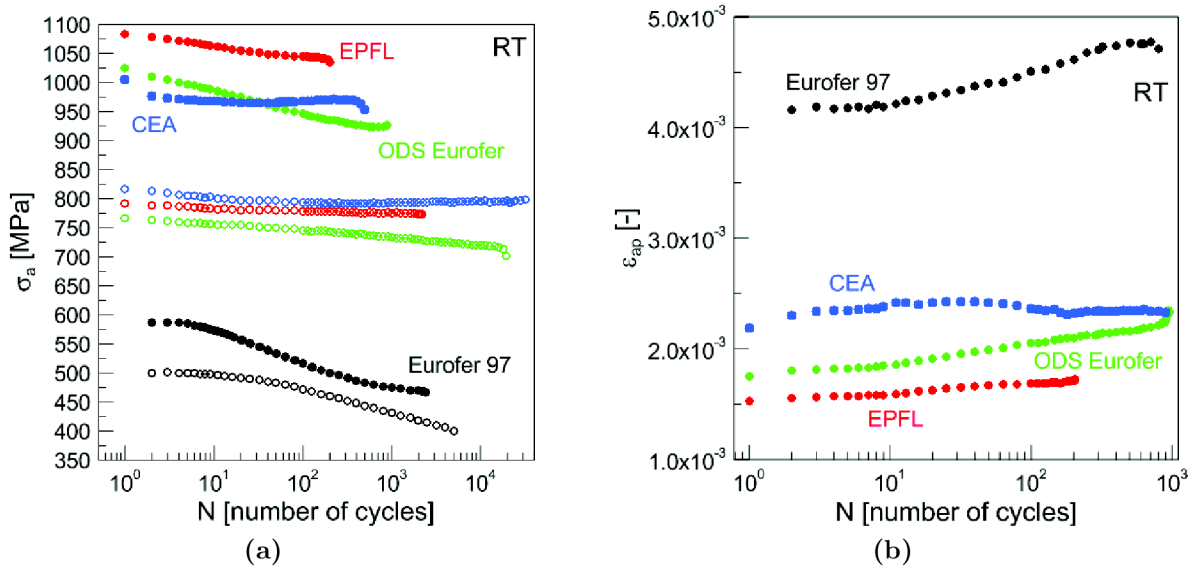
Figure 57: Cyclic softening curves at RT: a) in $\sigma = f(N)$; b) in $\varepsilon_{ap} = f(N)$ representation (full symbols - $\varepsilon_a = 0.7$ %, open symbols - $\varepsilon_a = 0.4$ %)
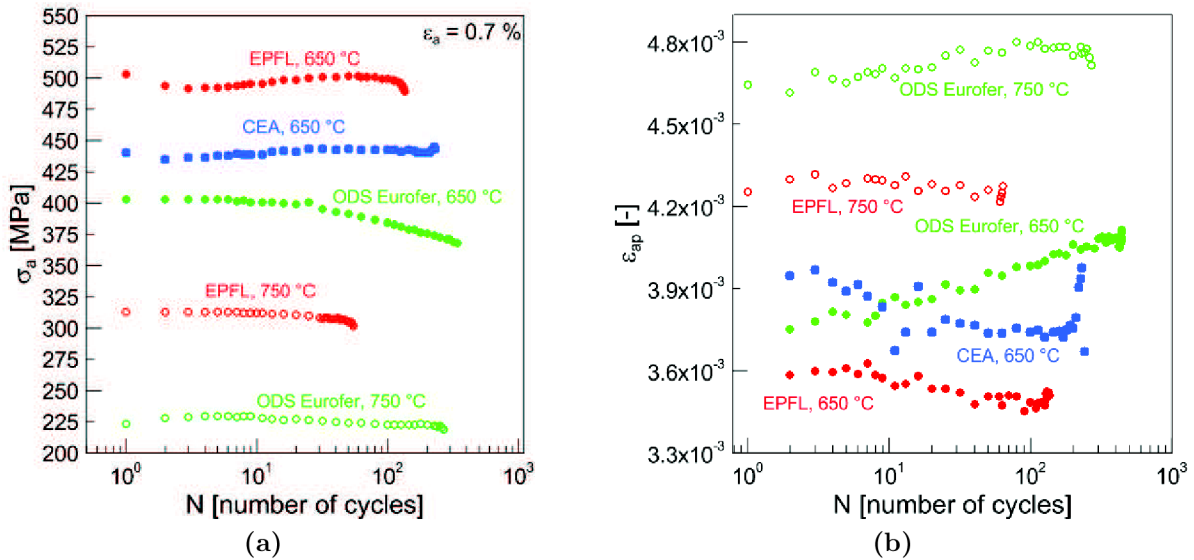
Figure 58: Cyclic softening curves for $\varepsilon_a = 0.7$ %: a) in $\sigma = f(N)$ representation at elevated temperatures (full symbols - 650 ℃, open symbols - 750 ℃); b) in $\varepsilon_{ap} = f(N)$ representation at elevated temperatures

loading with medium strain amplitude, while the ODS Eurofer steel possesses the lowest strength among studied ODS steels in this amplitude region (see open symbols in figure 57a).

Comparison of σ_a and ε_{ap} evolution with number of cycles at elevated temperatures is shown in figure 58. All studied steels keep quite high strength at 650 ℃ in comparison with conventional non – ODS RAFM or RAF (reduced activation ferritic) steels, see e.g. [60]. The EPFL steel cyclically resists to stress higher than 300 MPa even at 750 ℃. Unfortunately, the failure of specimens from the EPFL steel occurred after the lowest number of cycles at all tested temperatures. Strength of ferritic steels is higher than that of the ODS Eurofer steel at all testing temperatures. Due to the lack of material, no experiments were done with the CEA steel at 750 ℃.

4.3.5 Summary

Results of this part can be summarised in following points:

- The oxide dispersion strengthens material significantly.

- The ODS Eurofer steel exhibits cyclic softening at all testing temperatures and its rate increases with increasing strain amplitude and decreasing temperature.

- The CEA steel exhibits stable behaviour at all testing temperatures, slight hardening was observed at elevated temperatures.

- The EPFL steel exhibits the highest strength among studied steels. Stable behaviour was observed with exception of the highest amplitude at RT.

4.4   Cyclic stress – strain curves

The cyclic stress – strain curves for three tested temperatures are plotted in figure 59. The stress – strain curve is described by following equation:

$$\sigma_a' = K_b' \varepsilon_{ap}^{n_b'} \tag{16}$$

where K_b' is fatigue hardening coefficient and n_b' is fatigue hardening exponent. These parameters are given in table 6. A marked difference between two obtained batches of the CEA steel was found. Batch obtained in year 2010 exhibits higher cyclic strength than batch from year 2008, in spite of the fact that producer of material claims that both batches have the same chemical composition and they were prepared by the same
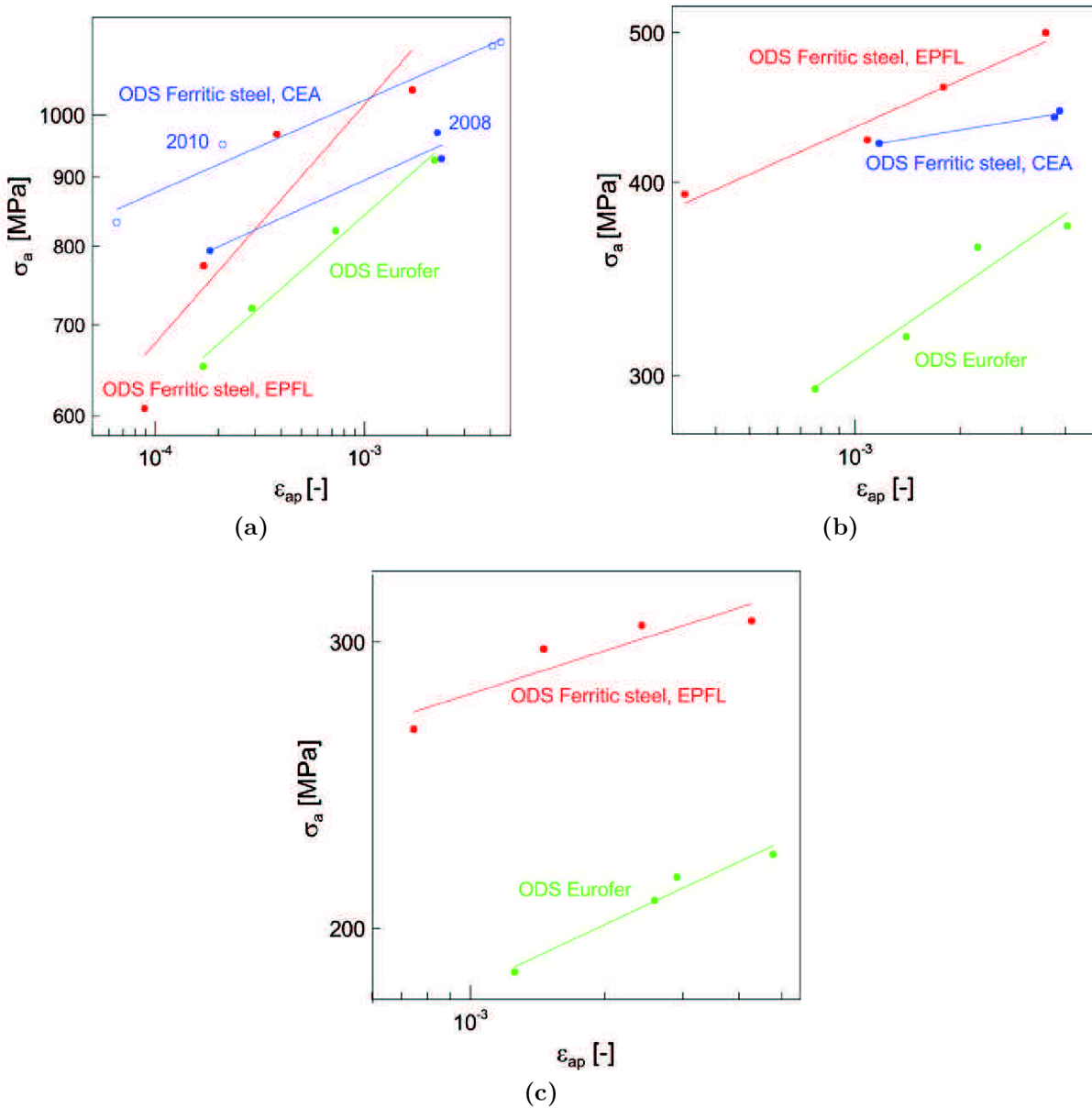
Figure 59: Cyclic stress – strain curves at a) RT; b) 650 °C; c) 750 °C

production route. The ODS Eurofer steel possesses the lowest strength among studied materials at all temperatures. Comparing two ODS ferritic steel, the CEA steel (2010) exhibits the highest cyclic strength at RT. The CEA steel (2008) has lower strength than the EPFL steel in high amplitude region but more strength than in low amplitude region. Cyclic stress – strain curve of the EPFL steel and the ODS Eurofer steel have higher slope, i.e. higher exponent n'_b than the CEA steel. The situation is similar at elevated temperatures. The EPFL steel and the ODS Eurofer steel have similar n'_b, which means similar slope of cyclic stress – strain curves. The data CEA steel lie slightly lower than the EPFL steel. It should be noted that experiments at elevated temperatures on the CEA steel were performed on batch from year 2008. The CEA steel was not tested at 750 °C because the lack of received material. The cyclic strength of the EPFL steel is higher than that of the ODS Eurofer steel.

Table 6: Parameters of Eq. 16 and the cyclic yield stress

	Temperature	K'_b [MPa]	n'_b [-]	$\sigma'_{0.2}$ [MPa]
The ODS Eurofer	RT	2160	0.136	928
	650 °C	906	0.15	357
	750 °C	445	0.128	201
The CEA steel (2008)	RT	1454	0.07	941
	650 °C	546	0.0375	432
The CEA steel (2010)	RT	1640	0.068	1074
The EPFL steel	RT	3431	0.176	1149
	650 °C	874	0.102	464
	750 °C	510	0.0877	296

4.5   Fatigue life curves

The three basic fatigue life curves, namely, combined curves, derived Coffin-Manson curves and derived Wöhler curves were measured. The amplitude of total strain was kept constant during cycling, therefore, the composed curve is presented firstly. As the name "combined curve" prompts, it can be decomposed to its particular parts, elastic strain amplitude and plastic strain amplitude, Eq. 17. The elastic part can be replaced by Basquin law [61], which describes dependence of σ_a vs. N_F, see Eq. 18. The Coffin–Manson law [62, 63], (Eq. 19) can be used for plastic part of combined curve and it describes the dependence of plastic strain amplitude on the number of cycles to failure. Inserting Eqs. 18 and 19 into Eq. 17, the life curve in constant total strain amplitude testing is given by Eq. 20

$$\varepsilon_a = \varepsilon_{ae} + \varepsilon_{ap} = \frac{\sigma_a}{E} + \varepsilon_{ap} \tag{17}$$

$$\sigma_a = \sigma_f'(2N_F)^b \tag{18}$$

$$\varepsilon_{ap} = \varepsilon_f'(2N_F)^c \tag{19}$$

$$\varepsilon_a = \frac{\sigma_f'}{E}(2N_F)^b + \varepsilon_f'(2N_F)^c \tag{20}$$

where E is Young modulus, ε_f' is the fatigue ductility coefficient (an extrapolation to the first half cycle), c is fatigue ductility exponent, σ_f' is fatigue strength coefficient and b fatigue strength exponent. The parameters of Basquin and Coffin–Manson laws (Eqs. 19, 18) were calculated and are given in Table 7. The fatigue life curves were determined at RT and 650 °C for all ODS materials and at 750 °C for the ODS Eurofer steel and for the EPFL steel.

Representative values of stress and plastic strain amplitude were chosen at the half life due to the fact that studied materials do not exhibit a stable cyclic behaviour, especially in case of the ODS Eurofer steel.

Table 7: Parameters of Basquin and Coffin-Manson law

	Temperature	σ_f' [MPa]	b [-]	ε_f' [-]	c [-]
The ODS Eurofer	RT	1449	-0.0651	0.0354	-0.434
	650 °C	803	-0.011	0.407	-0.689
	750 °C	370	-0.078	0.0229	-0.606
The CEA steel (2008)	RT	1342	-0.0471	1.01	-0.821
	650 °C	499	-0.02	0.0882	-0.982
The CEA steel (2010)	RT	1717	-0.062	1.01	-0.821
The EPFL steel	RT	2146	-0.112	0.042	-0.578
	650 °C	873	-0.0969	0.629	-0.904
	750 °C	375	-0.0302	0.0327	-0.446

4.5.1   Combined fatigue life curve

The combined curves of all studied materials **at RT** are presented in figure 60. The high strength of ODS materials causes that the elastic part is dominant even at high total strain amplitudes and the plastic strain amplitude is lower in order of magnitude at low total strain amplitudes. Two batches of the CEA steel are distinguished in figure 60b. The full line represents batch from 2008 and the dashed line that from 2010. The comparison of studied ODS steels is shown in figure 60d. Obviously, the EPFL steel exhibits the shortest fatigue life in this representation. The life time of the ODS Eurofer steel and the CEA steel (2008) is similar in region of studied strain amplitudes. The longest life was measured in the CEA steel 2010 in the high amplitude region, the differences become less significant with decreasing of strain amplitude.
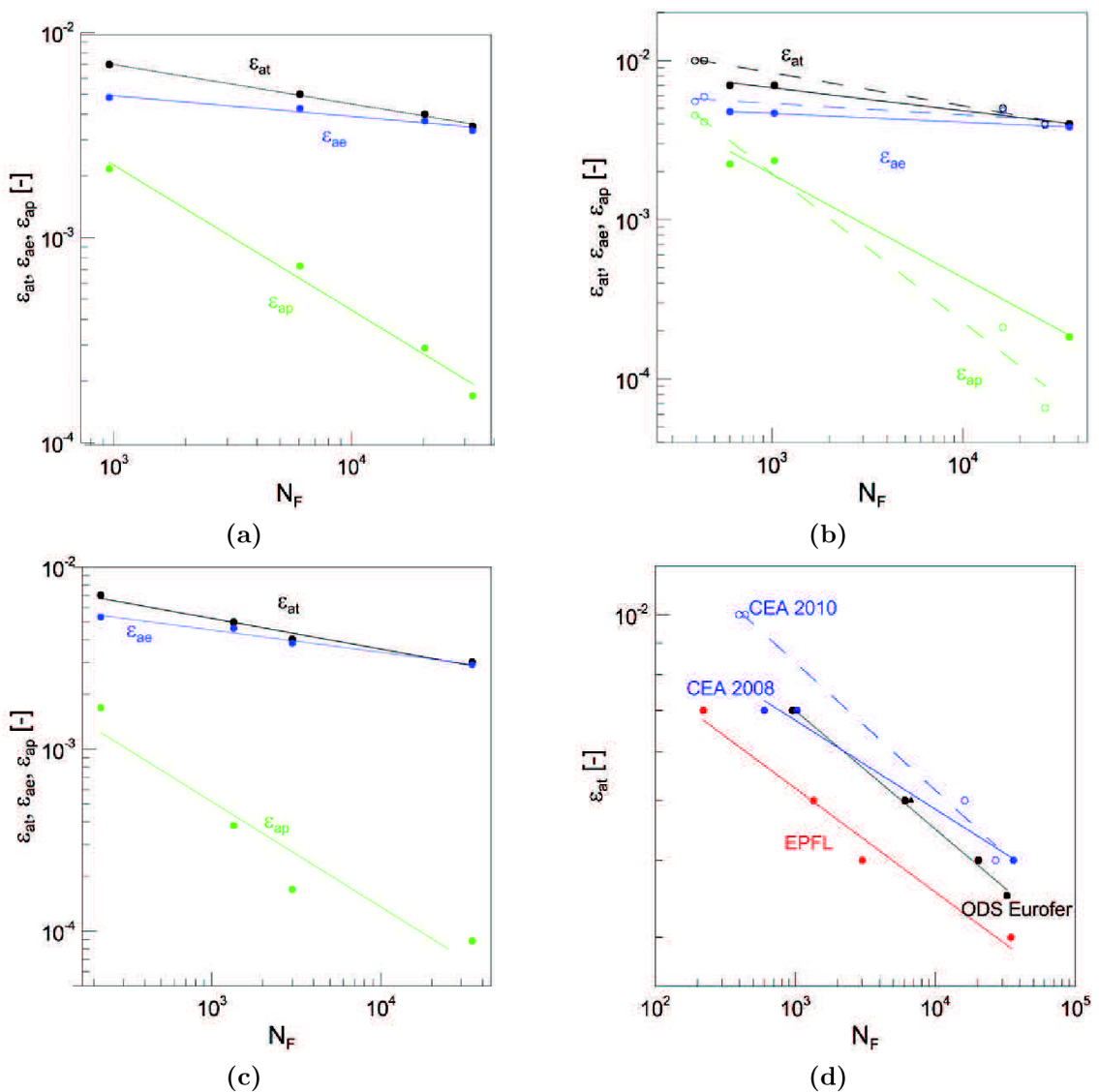
Figure 60: Combined curves measured at RT: a) the ODS Eurofer steel; b) the CEA steel; c) the EPFL steel; d) comparison of studied steels.

The results of combined curves obtained **at 650 ℃** are shown in figure 61. The plastic part of total strain amplitude increased with increasing temperature. Nevertheless, the elastic part is still dominant with exception of the highest stain amplitude. It was documented in previous section 4.4 that the fatigue strength at 650 ℃ was measured for the EPFL steel. It is confirmed in figure 61c. The elastic part is still dominant in the EPFL steel, only at the highest amplitudes both part are almost identical but the plastic part is not higher then elastic one as in the case of CEA steel and EPFL steel. In spite of these facts, the fatigue life is the shortest in case of the EPFL steel. The longest fatigue life was found in the ODS Eurofer steel. The fatigue life measured in the CEA steel is close to the EPFL steel in high amplitude region and to the ODS Eurofer steel in low amplitude region.
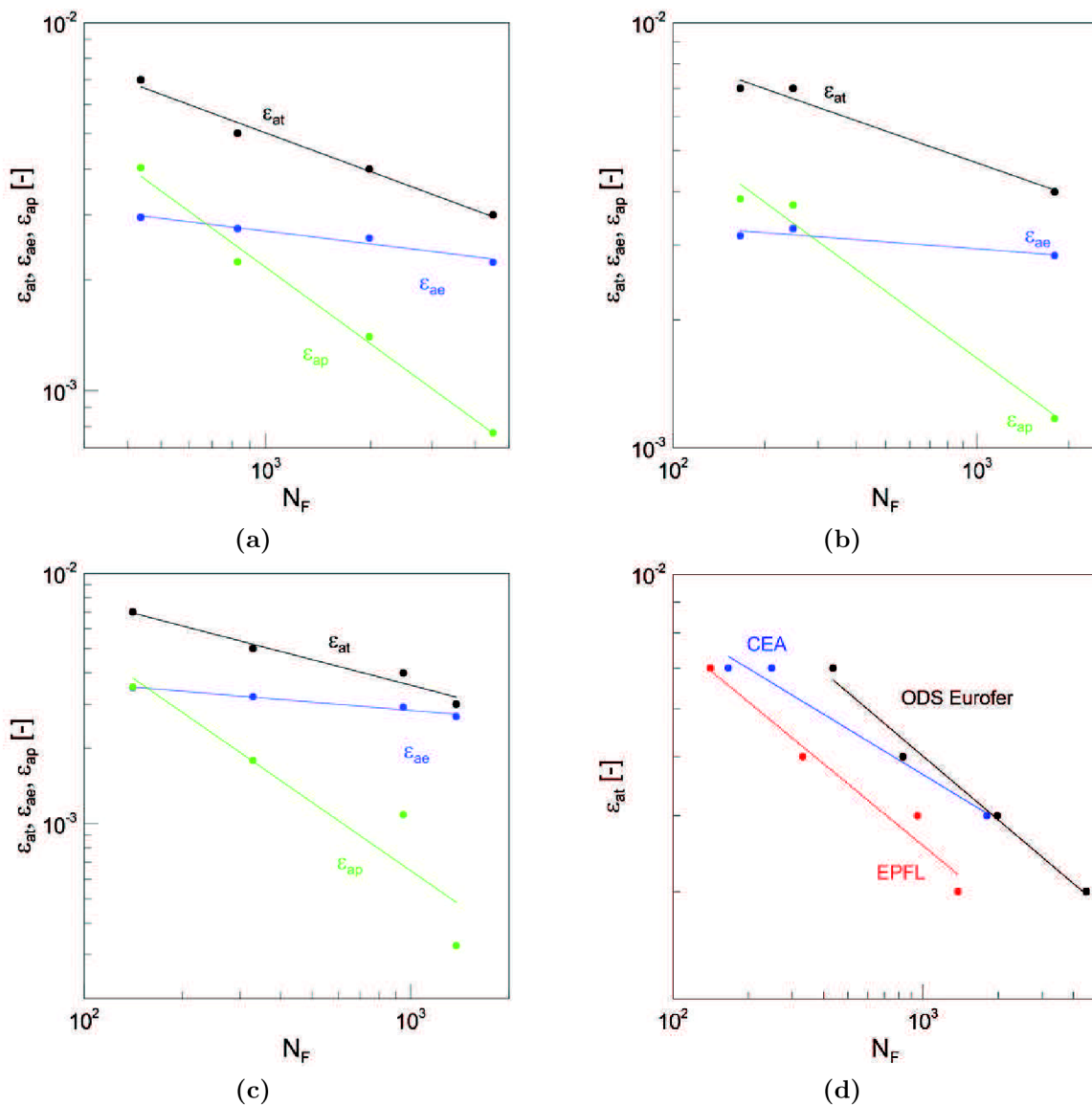
Figure 61: Combined curves at 650 ℃: a) the ODS Eurofer steel; b) the CEA steel; c) the EPFL steel; d) comparison of studied steels

The combined curves measured **at 750 °C** are shown in figure 62. Obviously, the plastic strain amplitude becomes dominant in the ODS Eurofer steel with the exception of the lowest amplitude. The plastic strain amplitude is lower in the EPFL steel than in the ODS Eurofer steel, which should result in longer fatigue life. Fatigue life in high strain amplitude region is significantly longer in the ODS Eurofer steel than in the EPFL steel. The fatigue life is similar in low strain amplitude region in this representation.
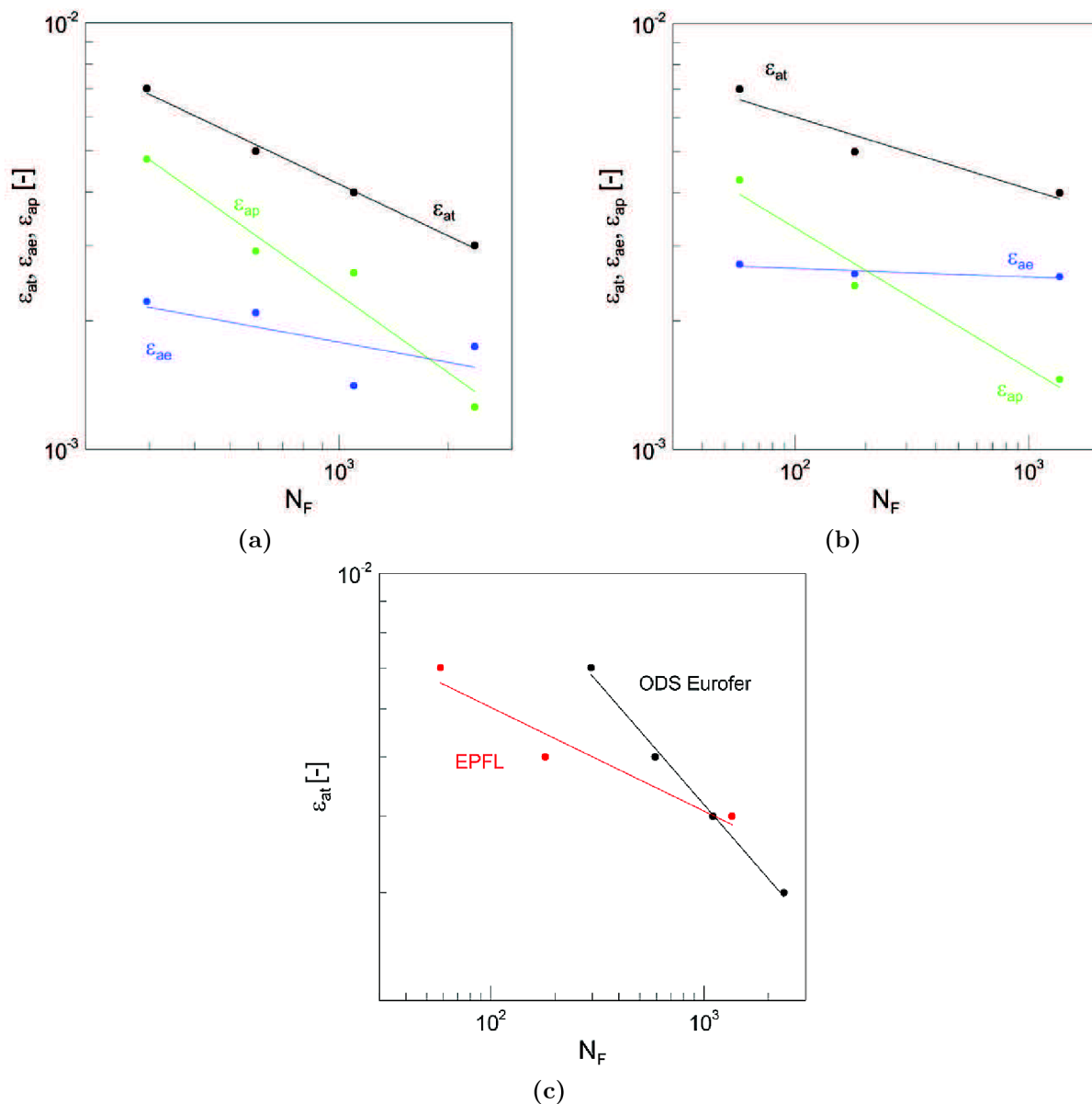
Figure 62: Combined curves at 750 °C: a) the ODS Eurofer steel; b) the EPFL steel; c) comparison of studied steels

4.5.2   Derived Wöhler curve

The derived[1] Wöhler plots of all materials are shown in figure 63. In figure 63a, the important improvement in cyclic strength in comparison with Eurofer 97 steel due to oxide dispersion is again documented. The stress amplitude at half-life is almost doubled for all studied ODS steels comparing with the Eurofer 97 steel. The ODS Eurofer steel and the EPFL steel curves have a similar slope, nevertheless the stress levels are higher for the EPFL steel than for the ODS Eurofer steel. On the other hand, fatigue life is longer for the ODS Eurofer steel than for the EPFL steel at the same stress amplitude σ_a. There is no visible difference in N_F of specimens with T and L axis direction in the ODS Eurofer steel. The CEA steel (2010) curve lie above all others curves meaning the longest fatigue life of all studied materials. The batch of the CEA steel obtained in year 2008 exhibits lower strength than batch from year 2010, which was also documented in cyclic deformation curves, see figure 59a.

At 650 ℃, the stress levels for all ODS materials are still relatively high, see the derived Wöhler plot in figure 63b. Both ferritic steels exhibits higher cyclic strength than the ODS Eurofer steel. The highest stress values are obtained for the EPFL steel in high stress amplitude region, whilst the best σ_a response in low strain amplitude region was found in the CEA steel. The ODS Eurofer steel and the EPFL steel keep quite high stress amplitudes even at 750 ℃.
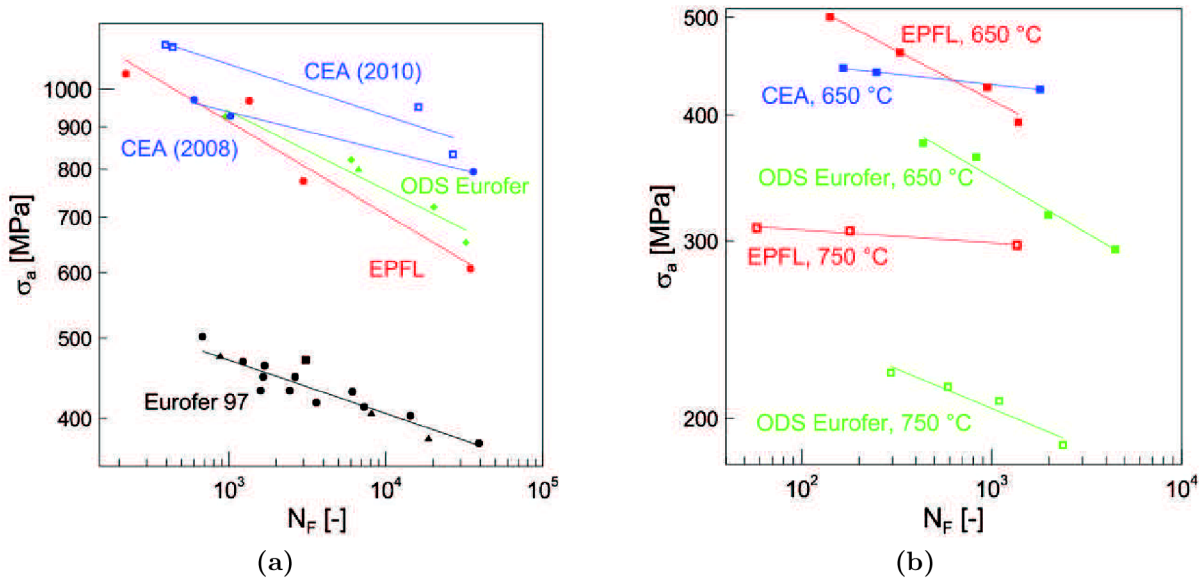
Figure 63: Derived Wöhler curves; a) RT; b) elevated temperatures: full symbols - 650 ℃; open symbols - 750 ℃

4.5.3   Derived Coffin–Manson curve

The resistance of the ODS steels and the Eurofer 97 steel to cyclic plastic strain at RT is shown in figure 64a as a Coffin-Manson plot. Apparently, the Eurofer 97 steel shows

---

[1]Since σ_a is not constant during the test and σ_a at the half life is used, the adjective "derived" is used.
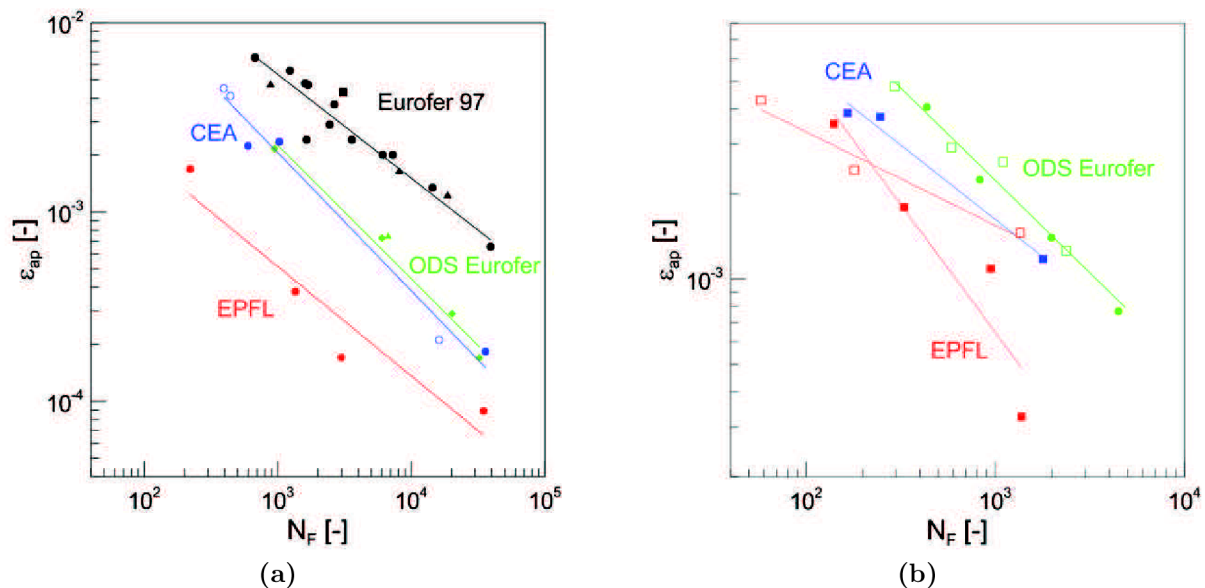
Figure 64: Coffin–Manson curves: a) RT; b) elevated temperatures: full symbols - 650 ℃; open symbols - 750 ℃

the best resistance to cyclic plastic deformation, on the contrary the EPFL steel exhibits the lowest resistance to cyclic straining. The ODS Eurofer steel and the CEA steel curves lie almost on the same curve and their resistance to cyclic straining is better in comparison with the EPFL steel. The data measured in the CEA steel 2008 and 2010 are distinguished in figure 64a (open symbols – year 2010; full symbols – 2008), and they were fitted adequately by one curve.

Coffin-Manson plots determined at elevated temperatures are shown in figure 64b.
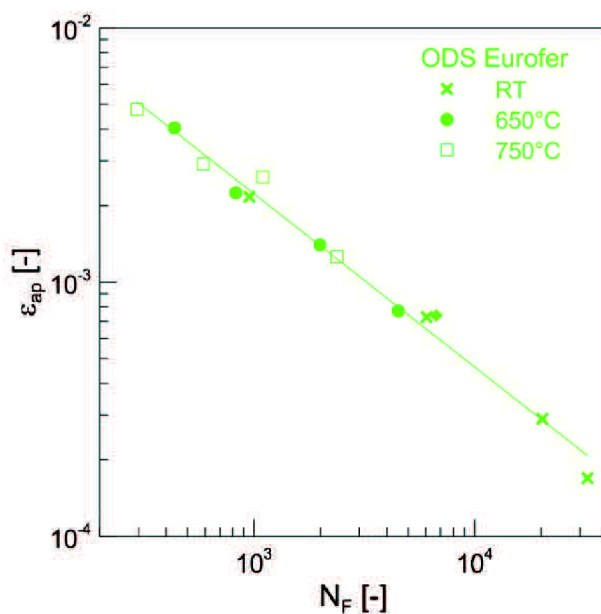
Figure 65: Coffin-Manson curve of ODS Eurofer steel for all tested temperatures

The resistance against cyclic plastic deformation is similar at elevated temperatures as at room temperature. The CEA steel exhibits a little lower cyclic plastic strain resistance than at room temperature. The slopes of curves for the EPFL steel are significantly different at 650 ℃ and 750 ℃.

Interestingly, it was observed that the Coffin-Manson data lie on one curve for the ODS Eurofer steel at all temperatures, see figure 65. It suggests that the mechanism of cyclic plastic deformation is identical at all tested temperatures.

4.5.4   Summary of chapters 4.4 and 4.5

- The strengthening effect of oxide particles results in high stress levels in cyclic stress–strain curves. Ferritic–martenistic microstructure is has lower strength than purely ferritic ones at all testing temperatures.

- The ODS Eurofer steel and the CEA steel exhibits similar resistance to cyclic plastic straining.

- The EPFL steel exhibits the shortest fatigue life among studied ODS steels, especially at RT, which is documented most clearly in Coffin–Manson plots.

- The elastic part of total strain amplitude is always higher than plastic one in specimens tested at RT even for the highest total strain amplitudes of 1 %. It is another type of confirmation of strong strengthening effect of oxide particles.

4.6 TEM observation after fatigue loading

4.6.1 The ODS Eurofer steel

The microstructure after fatigue loading at two different amplitudes at RT is shown in figure 66. Fatigue loading caused some changes in microstructure comparing with the as – received state: a) dislocation density decreased, most of grains are almost dislocation free. Individual dislocations in grains were observed sporadically. Low angle boundaries (LAB) consisting of dislocations were observed. b) Some grains increased the size to ~ 1 μm and ~ 1.3 μm after loading with $\varepsilon_a = 0.5$ % and $\varepsilon_{ap} = 0.7$ %, respectively. It means that cyclic plastic deformation can destroy some weak low angle boundaries also in
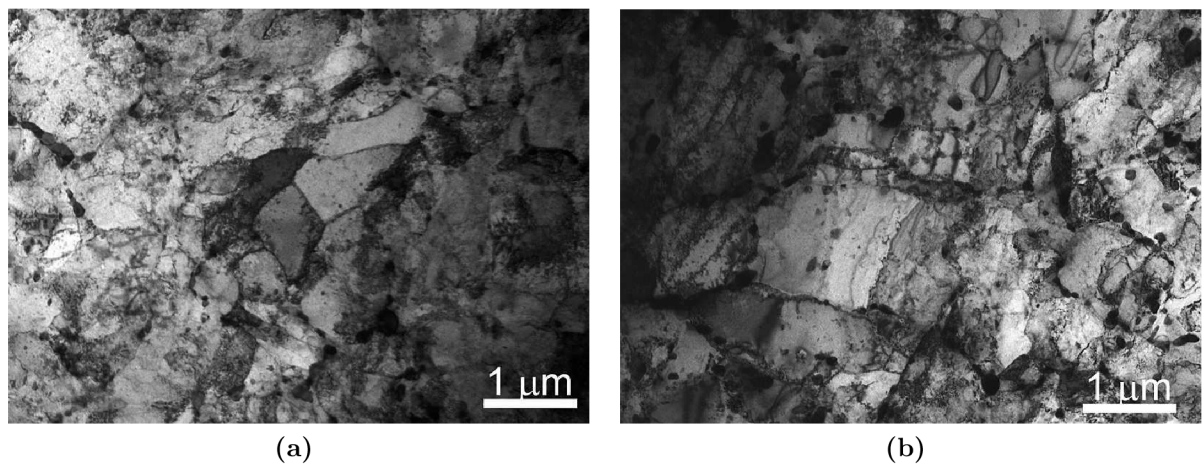
Figure 66: TEM micrographs of the ODS Eurofer steel in parallel section to the stress axis after fatigue loading at RT: a) $\varepsilon_a = 0.5$ %; b) $\varepsilon_a = 0.7$ %
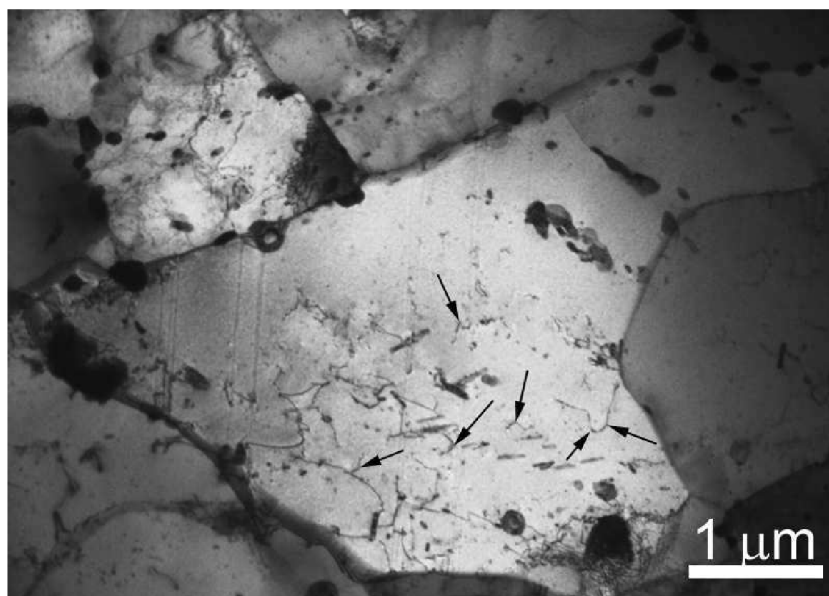
Figure 67: TEM micrographs of the ODS Eurofer steel in perpendicular section to the stress axis after fatigue loading at 650 ℃, $\varepsilon_a = 0.4$ %
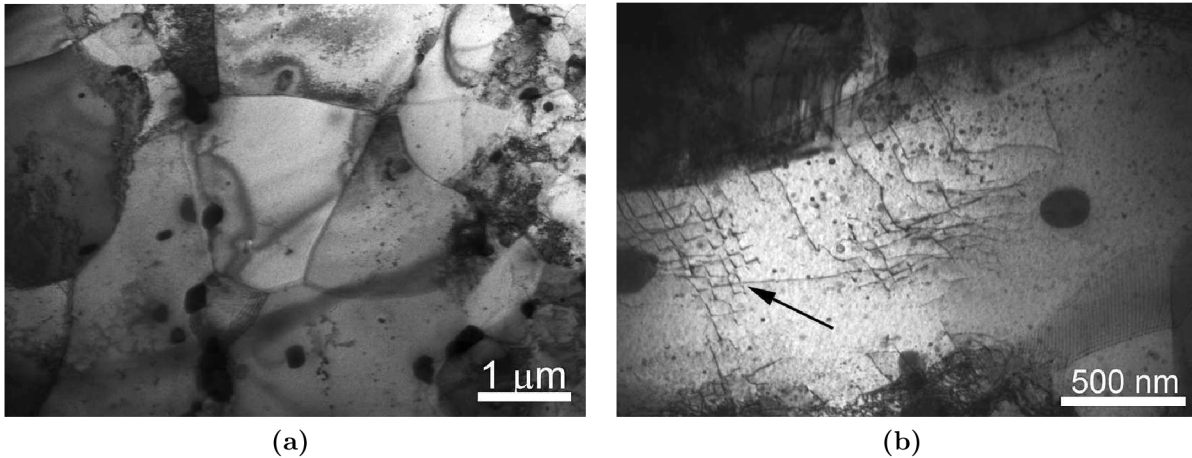
Figure 68: TEM micrographs of the ODS Eurofer steel after fatigue loading at 750 °C, $\varepsilon_a \cong 0.4$ %: a) bigger grains almost without dislocations; b) grain with high dislocation density

material strengthened by oxide dispersion. Carbides are situated at the grain boundaries, no changes in carbide distribution and in their size were observed.

An example of micrographs obtained after cyclic loading at 650 °C is shown in figure 67. Overall dislocation density decreased. Some low angle boundaries were destroyed by cyclic plastic deformation leading to the growth of grains size. The grain size varies from 1 μm to several micrometres. Two types of bigger grains were observed: dislocation free grains and grains with high dislocation density (figure 67). The effect of oxide dispersion (dislocations are pinned by oxides) is clearly visible and marked by arrows in figure 67). Nevertheless, no dislocation patterns were observed.

The grain size increased also in specimens cycled at 750 °C. Bigger grains with high dislocation density (figure 68b) and grains almost dislocation free (figure 68a) were observed as well as in specimens cycled at 650 °C. The grain size did not increase dramatically comparing with specimens cycled at 650 °C and some areas with initial grain size were
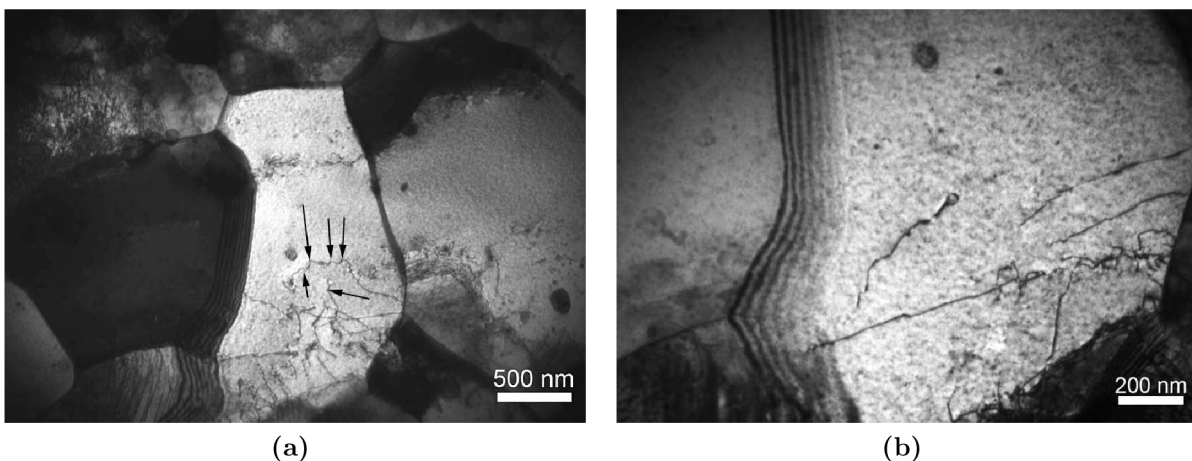
Figure 69: TEM micrographs of the ODS Eurofer steel after fatigue loading at 750 °C, $\varepsilon_a \cong 0.4$ %: a) bigger grain with higher dislocation density; b) detail of bottom part

found. The twist low angle boundary is marked by arrow in figure 68b. Another grain is shown in figure 69. One half of this grain is dislocation free and second half contains high dislocation density. The pinning of dislocation by oxides is marked by arrows. A detail of bottom part of grain (shown in figure 69a) is presented in figure 69b.

4.6.2 The CEA steel

The microstructure of the CEA steel cycled at RT is shown in figure 70. The dislocation density inside grains slightly decreased, but no differences were found in comparison with the as–received state. The statistical analysis revealed grain size of (0.5 ± 0.15) μm in section perpendicular to the extrusion axis, i.e. no difference with as–received state. This fact is consistent with stable fatigue behaviour of the CEA steel. The elongated microstructure in the section parallel to the extrusion axis is shown in figure 70b.

(a) (b)
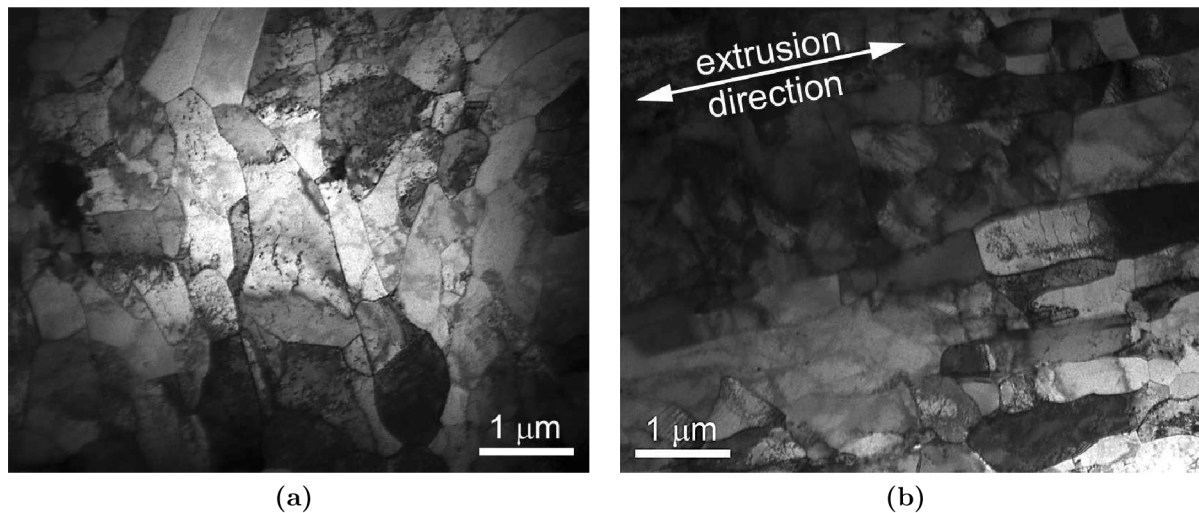
Figure 70: TEM micrographs of the CEA steel after fatigue loading at RT a) $\varepsilon_a = 0.7$ %, perpendicular section; b) $\varepsilon_a = 0.4$ %, parallel section

Some changes in microstructure due to fatigue loading were identified in specimens cycled at 650 ℃. An overview of microstructure in cross section is shown in figure 71a. Statistical analysis was carried out in order to determine grain size distribution. In spite of the fact that grains of size around 1 μm are present in the microstructure, the grain size was measured as (0.53 ± 0.23) μm in section perpendicular to the extrusion axis. It can be concluded that grain size increase is statistically negligible. The dislocation density inside grains is quite high.

A section parallel to the extrusion axis of grain with high dislocation density is shown in figure 72. Dislocation are pinned by oxides. An example of the tilt low angle boundary is marked by arrow in left part of figure 72 and the twist low angle boundary is marked right part of figure 72.

Figure 71: TEM micrographs of the CEA steel after fatigue loading at 650 ℃, $\varepsilon_a = 0.7$ %:
a) perpendicular section; b) parallel section

Figure 72: TEM micrographs of grain with high dislocation density in the CEA steel after
fatigue loading at 650 ℃, $\varepsilon_a = 0.7$ %, Tilt LAB (left arrow) and twist LAB (right arrow) are
visible

4.6.3   The EPFL steel

The overview of area with small grains in the EPFL steel after fatigue loading is shown in
figure 73a. Dislocation density in this area is lower then in areas of bigger grains, some of
them are dislocation free. Statistical analysis proved that the size of small grains was not
changed due to fatigue loading. The overview of area containing bigger grains is shown
in figure 73b. The grain size in regions of bigger grains varies from 1 μm to 3 μm.

Two types of bigger grains were found. The first type of grains possesses very high
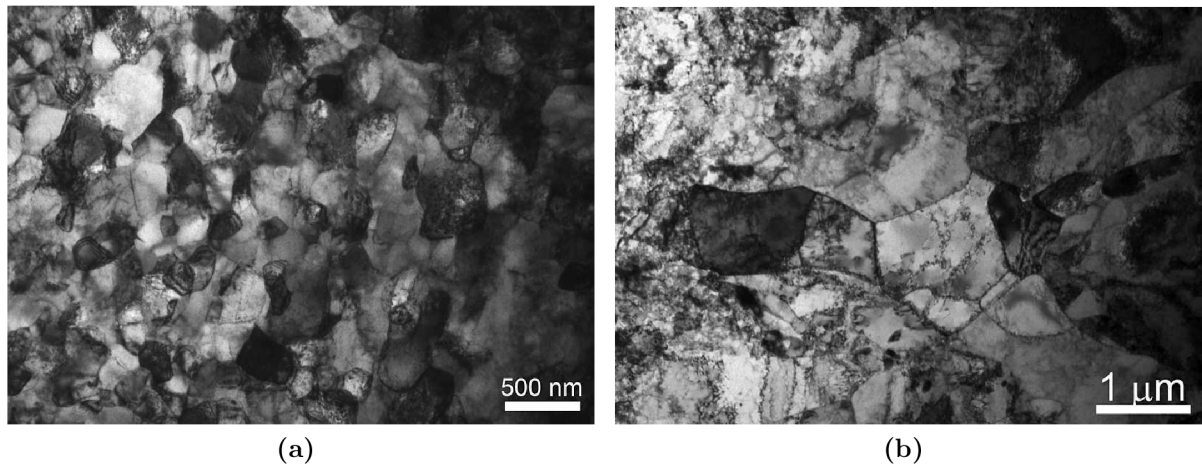
Figure 73: TEM micrographs of the EPFL steel after fatigue loading at RT, $\varepsilon_a = 0.7$ %, parallel section: a) areas of small grains; b) area of bigger grains
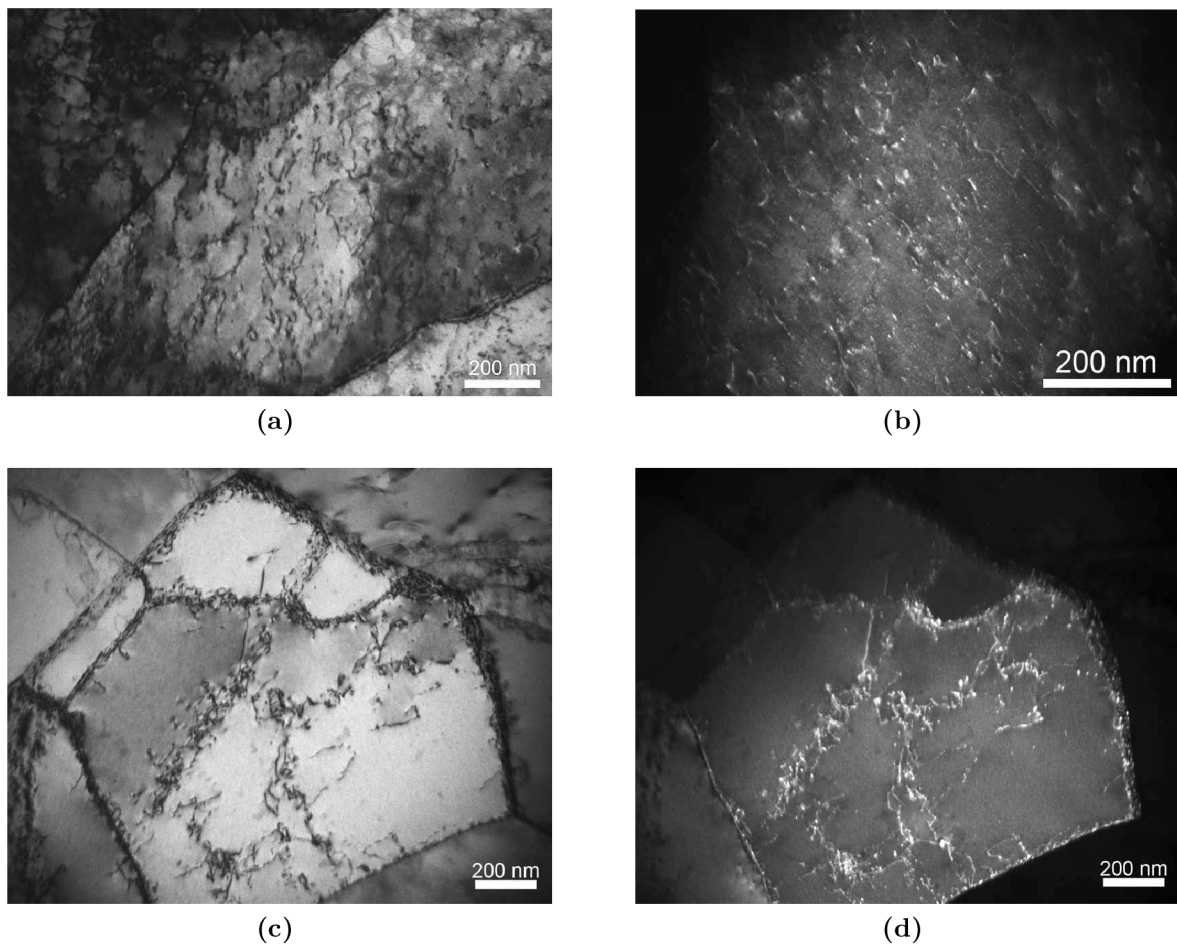
Figure 74: TEM micrographs of larger grain in the EPFL steel after fatigue loading at RT, $\varepsilon_a = 0.7$ %, parallel section. Grains with high dislocation density: a) bright field; b) dark field; Grains with low angle boundaries: c) bright field; d) dark field

dislocation density, see figure 74a. The dislocation density was estimated to be equal 1.1×10^{14} m^{-2} in figure 74a. The foil thickness was not measured for every micrograph. During the experiments with FIB foils of known thickness was observed that foils thicker than 100 nm are not well transparent. Therefore, the foil thickness of 75 nm was chosen for dislocation density estimation. The assumption that only projection of dislocation length is visible was adopted and results were corrected to average angle of 45 degree between dislocation line to the foil plane. Dislocations in such grains are pinned by oxide particles, which is visible better in TEM dark field mode, see figure 74b. The second type of bigger grains is shown in figure 74c. Presented grain is fractionated to small subgrains. Individual dislocations are also present in subgrains and are visible better in dark field mode, see figure 74d. The first type of grains is more frequent in microstructure.
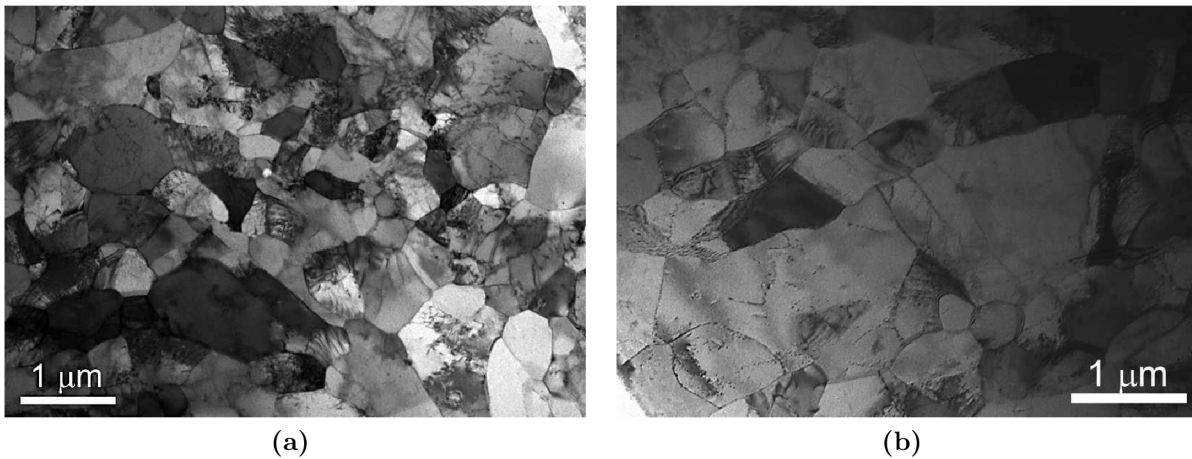

(a)   (b)

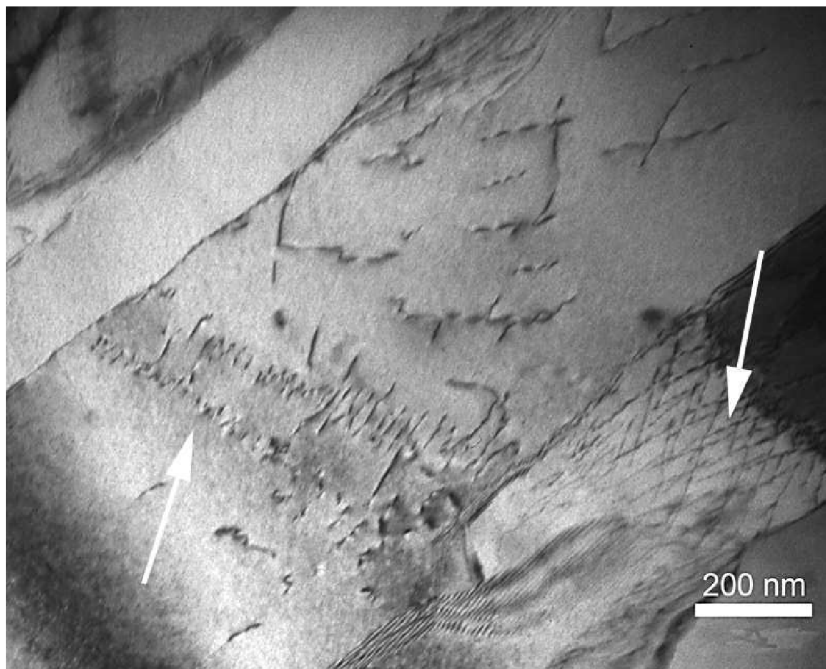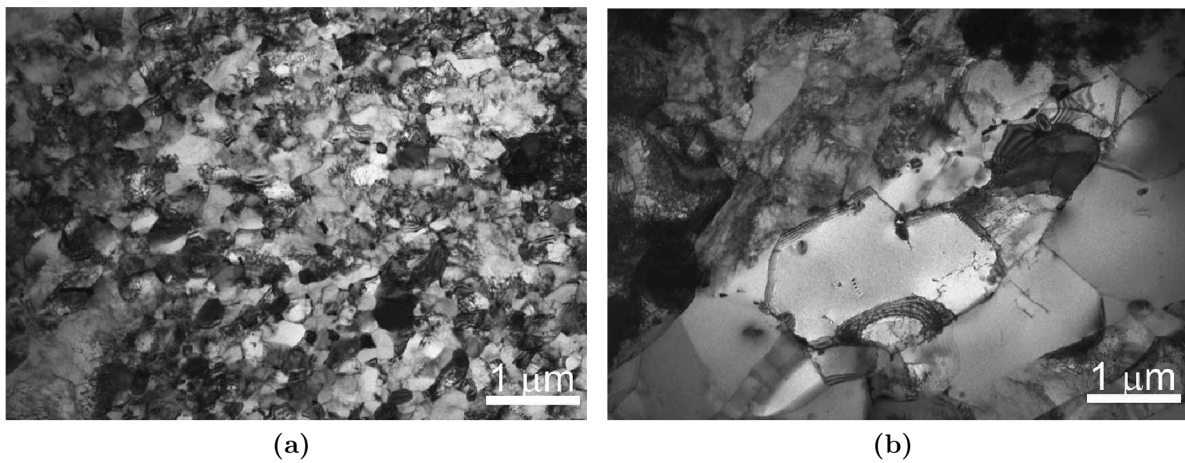**Figure 75:** TEM micrographs of the EPFL steel after fatigue loading at 650 ℃, $\varepsilon_a = 0.3$ %, perpendicular section to loading axis: a) areas of small grains; b) area of bigger grains
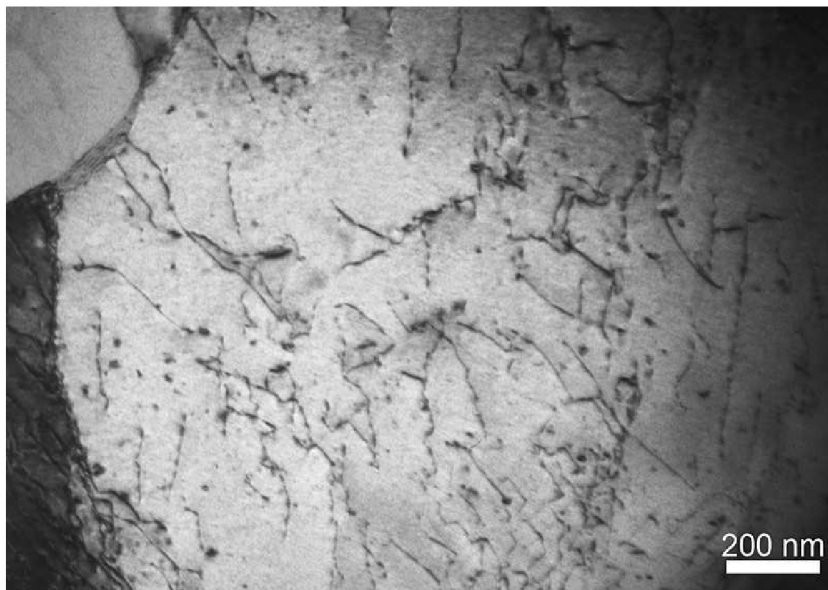
Figure 76: TEM micrographs 650 ℃, EPFL steel. Dislocations are pinned by fine dispersion

The bimodal grain size distribution after fatigue loading at 650 ℃ is shown in figure 75. The region of small grain is presented in figure 75a. According to results of statistical analysis, grain size of small grains did not changed during fatigue loading. Dislocation density inside small grains is lower in comparison with as – received state and specimens cycled at RT. Big grains with lower dislocation density (almost dislocation free) are shown in figure 75b. Large grain with very high dislocation occupancy ($\rho \doteq 1.7 \times 10^{14} \ m^{-2}$) in a grain shown in figure 76) are also present in microstructure, see figure 76. The dislocation are pinned by oxide dispersion which is clearly visible in dark field mode. There are no noticeable dislocation patterns.

Both areas of bimodal grain size distribution after fatigue loading at 750 ℃ are shown in figure 77a, the large grain in the middle of micrograph and area of small grains in right bottom corner. The area of small grains is shown using higher magnification in figure 77b. Obviously, grains are dislocation free or contain individual dislocations with

(a)   (b)
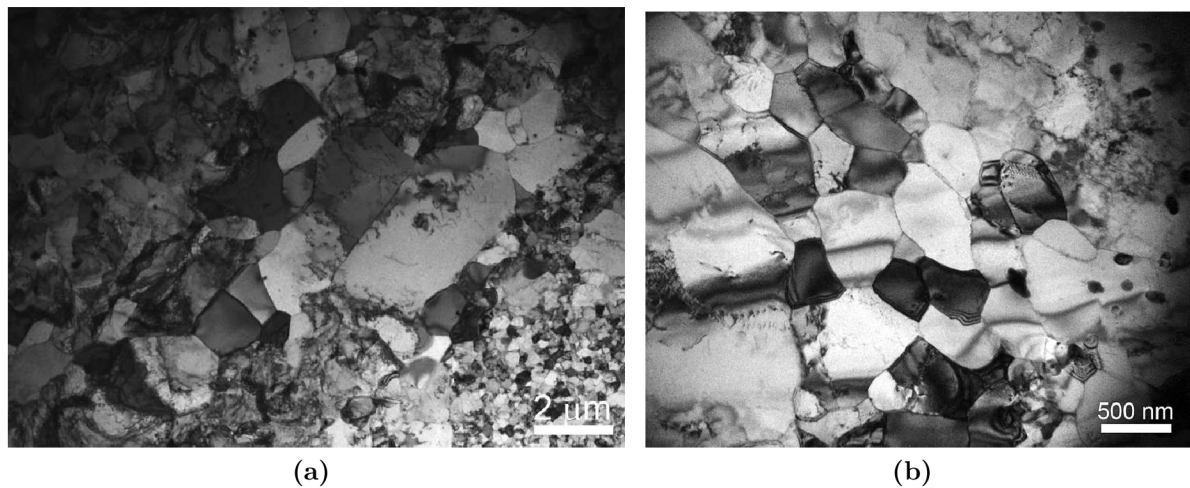
Figure 77: TEM micrographs 750 ℃, EPFL steel: a) parallel section to loading axis; b)parallel section to loading axis

(a)   (b)
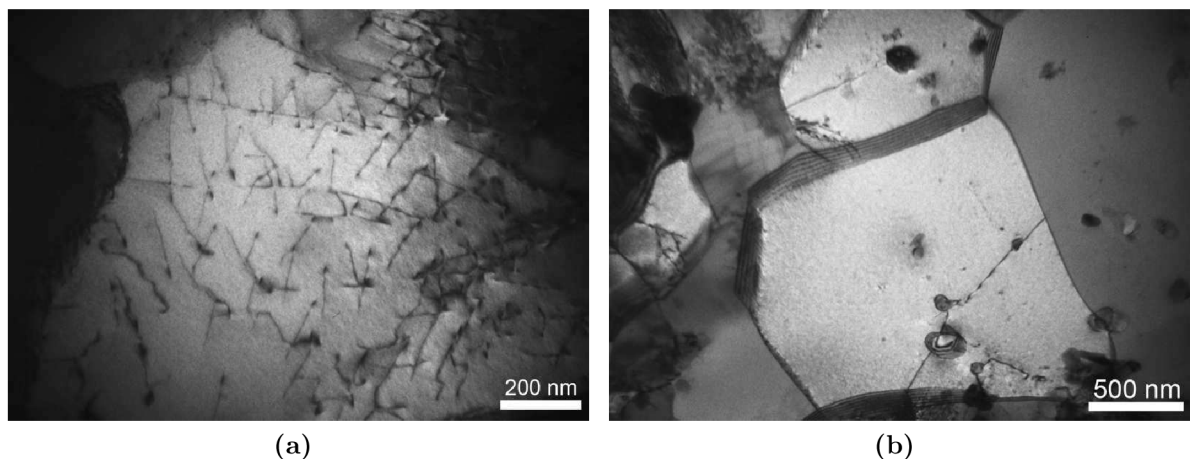
Figure 78: TEM micrographs 750 ℃, EPFL steel: a) parallel section to loading axis; b) parallel section to loading axis

sporadic occurrence and their size is comparable to the size of grains in as–received state. It means that main part of cyclic plastic deformation takes part in larger grains at all testing temperatures. The bigger grains are present in two types, with low and very high dislocation density inside such grains, as well as in specimens at RT and at 650 °C. Grain with very high dislocation density ($\rho \doteq 1.3 \times 10^{14}\ m^{-2}$) is shown in figure 78a. Dislocations are pinned by yttrium oxides and no dislocation pattern was observed as well as in specimens at RT or at 650 °C. An individual dislocation inside another big grain is shown in figure 78b. The dislocation density estimated in figure 78b is equal to $9.6 \times 10^{12}\ m^{-2}$.

4.6.4   Summary

Changes in microstructure owing to fatigue loading can be summarised in following points:

- The overall dislocation density decreased during fatigue loading of the ODS Eurofer steel at all testing temperatures. Grain size increased due to destruction of low angle boundaries by cyclic plastic straining. The mean grain size increases more rapidly at elevated temperatures: the higher temperature, the bigger grains were found in the microstructure, see Table 8. Two types of big grains (dislocation free and with high dislocation density) were distinguished after fatigue loading at elevated temperatures. No 3-D dislocation patterns were found.

- The microstructure of the CEA steel after fatigue loading at RT was almost identical with the as – received state. At 650 °C, some grains grew to the diameter of about 1 μm. Nevertheless, statistical analysis proved that this growth is not statistically important. Dislocation density slightly decreased at both testing temperatures.

- Dislocation density decreased at all testing temperatures in small grains in the EPFL steel. Two types of bigger grains were found in microstructure, the ones with very high dislocation density and the ones almost dislocation free. No 3-D dislocation patterns were found.

Table 8: Mean grain size measured in the ODS Eurofer steel cycled with different conditions, grain size of as–received state was measured as 0.72 μm

	$\varepsilon_a = 0.4\ \%$	$\varepsilon_a = 0.5\ \%$	$\varepsilon_a = 0.7\ \%$
RT	-	1 μm	1.3 μm
650 °C	1.8 μm	-	2.3 μm
750 °C	1.9 μm	-	-

4.7 Surface relief after fatigue loading and crack initiation

4.7.1 ODS Eurofer steel

Two examples of surface relief formed during fatigue loading are shown in figure 79. The surface relief is developed in large volumes of similar crystallographic orientations of several microns in size, i.e. into the blocks fractionated into the subgrains. Nevertheless, the relief is not formed in usual way of persistent slip markings of typically 1 μm in thickness but all the surface of such grain is covered by rough, mostly parallel, thin bands. The nucleation of the fatigue cracks takes place inside these surface rough zones or at the interface of these zones and seemingly non–deformed matrix. An example of crack initiated withing surface relief is shown and marked in figure 80a. Long crack

Figure 79: Surface relief formed after cyclic loading in the ODS Eurofer steel at RT a) $\varepsilon_a = 0.7$ %, b) $\varepsilon_a = 0.4$ %

Figure 80: Surface relief formed after cyclic loading in the ODS Eurofer steel at RT a) $\varepsilon_a = 0.7$ %, b) $\varepsilon_a = 0.4$ %

propagating also at interface between rough surface and non–deformed matrix is shown in figure 80b.

4.7.2   CEA steel

The specimen's surface was observed after failure. In the case of the CEA steel, SEM observation revealed relatively high density of fatigue cracks in specimens cycled with high strain amplitudes. No clear surface relief (e.g. extrusions, intrusions, roughened surface) formed due to the cyclic straining was observed. An example of a nucleated fatigue crack is shown in figure 81a.

Small shear bands inclined to 45 degrees to the stress axis are visible close to the crack tips and are marked in figure 82a. Detail of the shear band is shown in figure 82b.The elongated microstructure formed by the hot extrusion is clearly visible. Similar

(a)   (b)
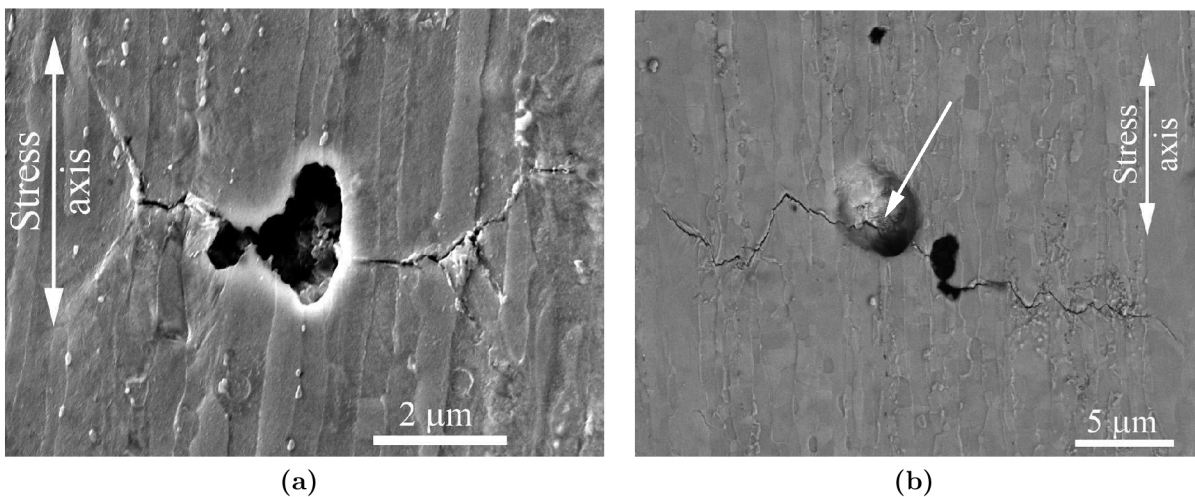
Figure 81: Fatigue cracks nucleated in voids in the CEA steel at RT: a) $\varepsilon_a = 0.7$ %, b) $\varepsilon_a = 0.4$ %.

(a)   (b)
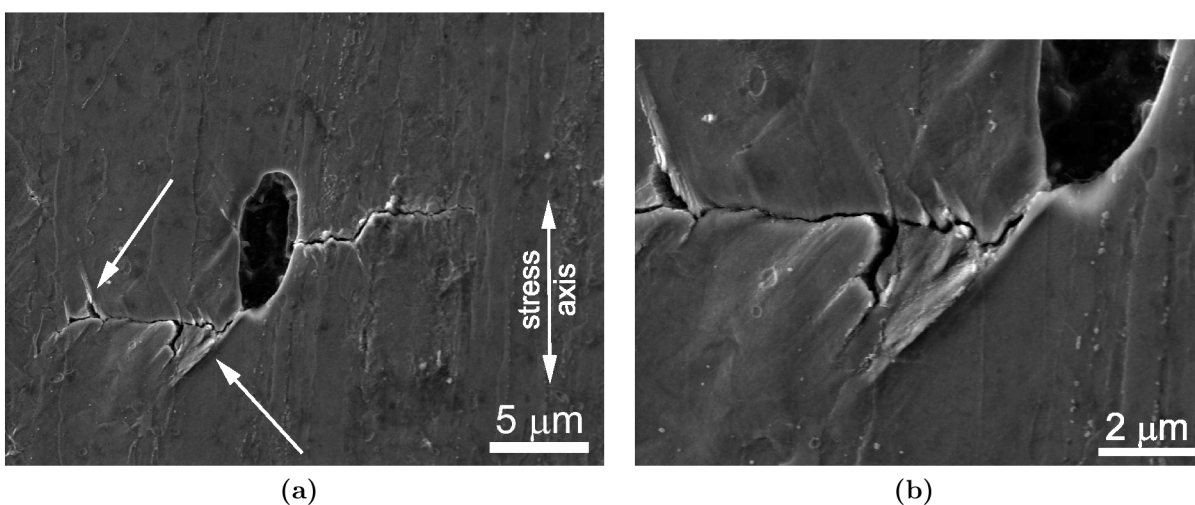
Figure 82: Fatigue cracks nucleated in voids in the CEA steel at RT: a) $\varepsilon_a = 0.7$ %.

observation was performed on specimens cycled using low strain amplitude, see figure 81b. In this case, the density of fatigue cracks is very low. All observed fatigued cracks initiated from microstructural defects (voids). Fatigue cracks grew mostly perpendicularly to the stress axis, the growth in "stage I" [35] common to materials having bigger grains was not found.

4.7.3   EPFL steel

In the EPFL steel, the situation is similar to that in the ODS Eurofer steel. The surface relief originated due to cyclic plastic loading is formed in some larger grains (figure 83).

The inspection of micrographs reveals that the preferential crack nucleation sites are small voids surrounded by grains with rough surface or just rough surface. Crack nucleation within the surface relief without a void was observed too (figure 83a). The crack

(a)   (b)
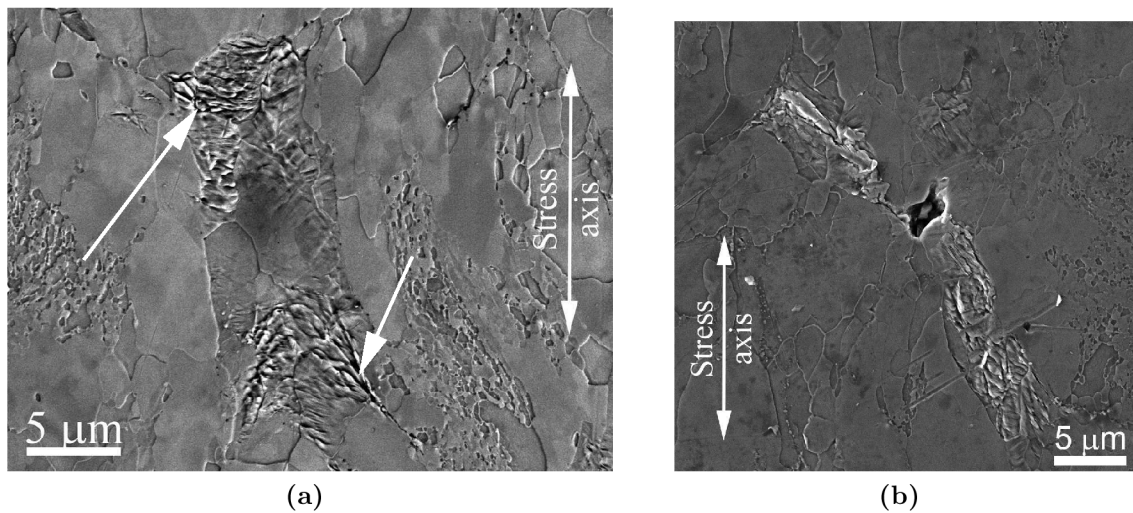
Figure 83: Surface relief formed after cyclic loading in the EPFL steel at RT a) $\varepsilon_a = 0.7$ %, b) $\varepsilon_a = 0.4$ %

(a)   (b)

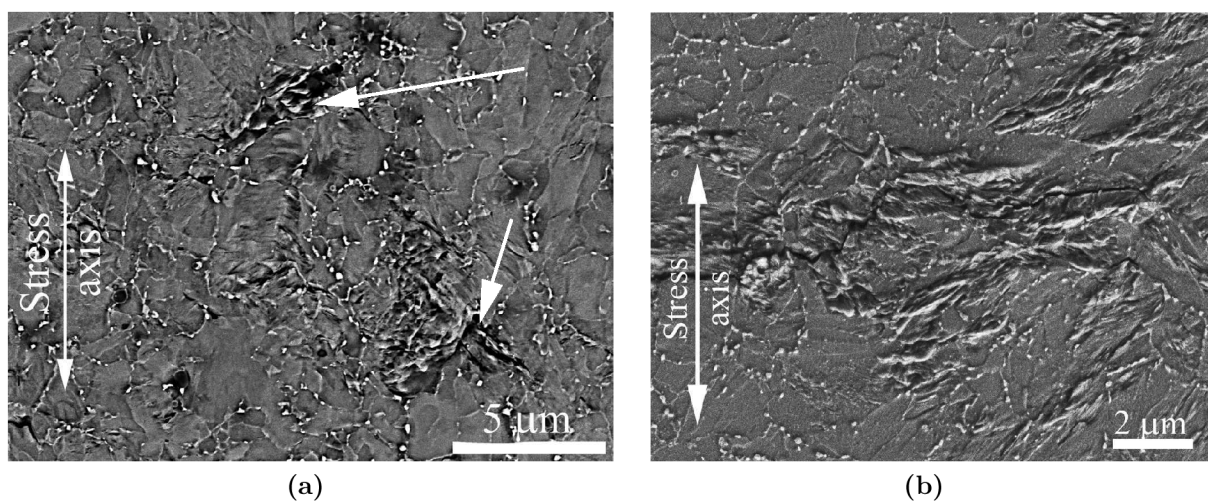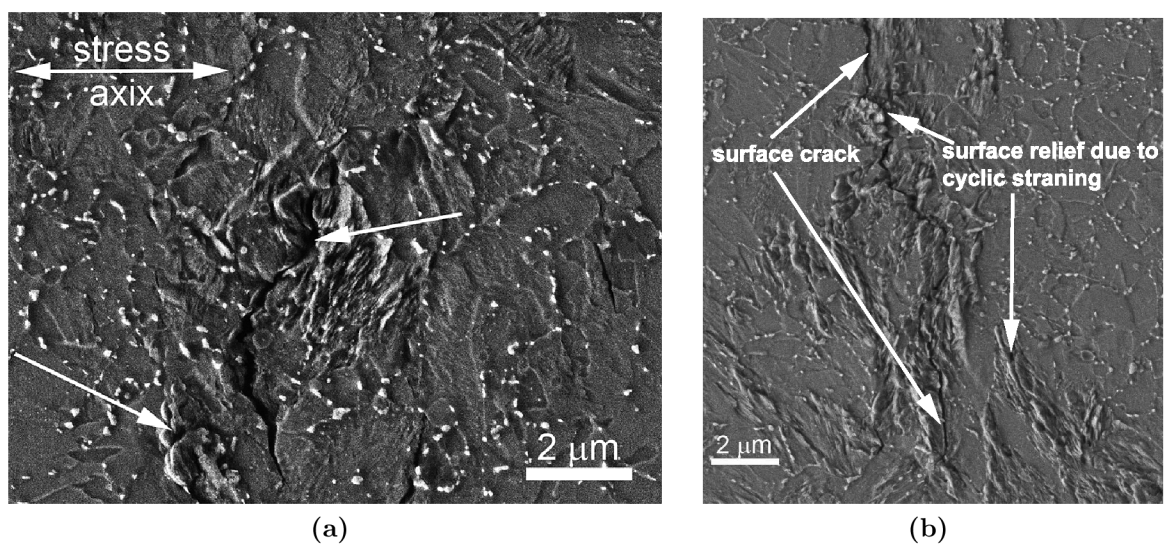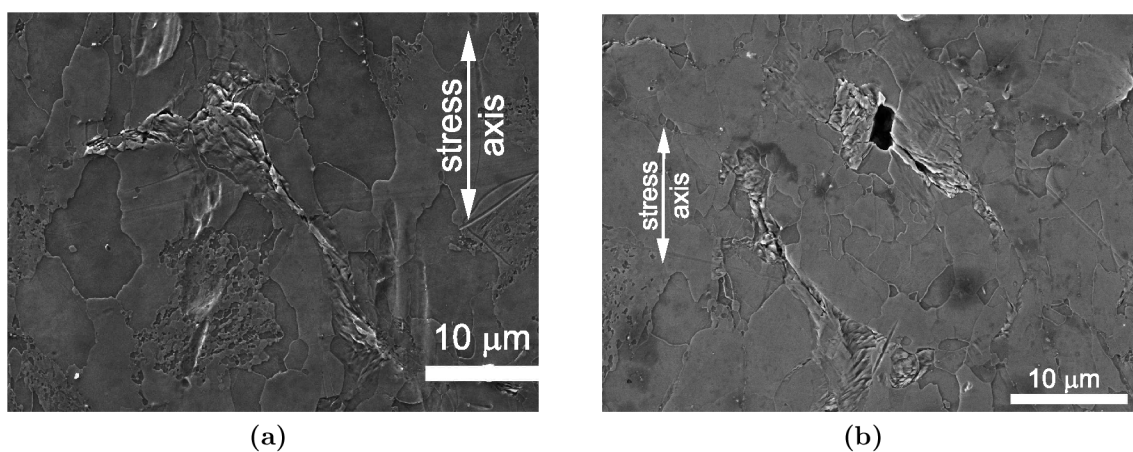**Figure 84:** Surface relief formed after cyclic loading in the EPFL steel at RT a) $\varepsilon_a = 0.7$ %, b) $\varepsilon_a = 0.4$ %

path is most often located along the interface between the rough area and seemingly non-deformed region. Intergranular crack growth is observed in some areas too in first stages of propagation. Another example of surface relief formation is shown in figure 84.

4.7.4   An attempt to reveal the microstructure under surface relief in the ODS Eurofer steel

Focus ion beam technique was used for preparation of thin lamella for TEM exactly from place where the surface relief was formed. The lamella preparation process is well described in the literature [64, 65, 66]. Briefly, the place of interest, in our case surface relief formed by cyclic straining, is protected by thin Pt layer. Two trenches at both sides of protective layer are prepared by current of ions of 15 nA. Subsequently, the TEM lamela is thinned to approximately 1 μm by current of ions of 1 nA. The lamella is lifted out from specimen in next step using micromanipulator and it is "welded" to TEM holder by Pt deposition. The final thinning is carried out using lower current of ions of 150 pA. Acceleration voltage of 30 kV was used for described steps of preparation. Nevertheless, it was observed that ions accelerated by 30 kV cause damage which prevents TEM observation. For this reason, last preparation steps were performed with acceleration voltage of 2 kV only. Typically, dimensions of FIB lamellas are 15 μm $\times$ 10 μm with thickness of about 75 nm. TEM lamellas were prepared from the ODS Eurofer steel specimen cycled at $\varepsilon_a = 0.7$ %. The TEM micrographs are shown in figure 85. Grains are visible very well and their size is in agreement with grain size measured in TEM micrographs taken from TEM foils prepared by standard procedure. The very bright layer covering and highlighting specimen surface relief is a Pt layer prepared by electron deposition. The surface relief is marked by arrows. Even though the specimen surface is clearly visible (see detail in figure 85b), no arranged dislocation structure was found neither under specimen surface relief nor in TEM foils prepared using standard technique. The typical FIB damage is present in form of small dislocation loops.

(a)   (b)
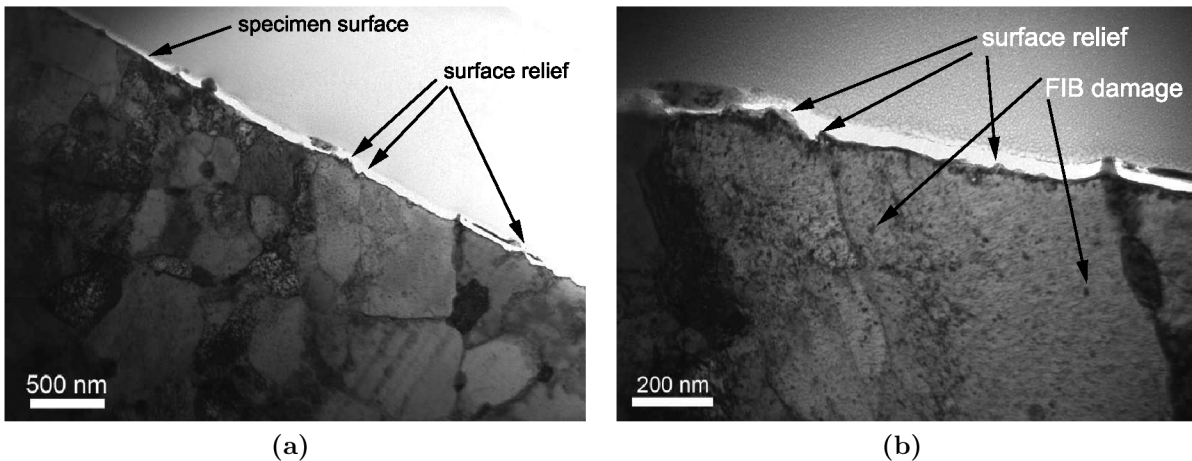
Figure 85: TEM micrographs of thin lamela prepared by FIB technique from surface relief, a) overview; b) detail of centre part

4.8   Small crack growth

4.8.1   Small crack growth path

The small crack growth path under the specimen surface was investigated by means of FIB – SEM 3D tomography in the ODS Eurofer steel. The principle of this methodology and examples of applications in the fatigue crack growth investigations can be found for example in [67, 68, 69, 70] and it is explained by figure 86a. Briefly, the area of interest, in our case rumpling surface containing crack, is protected by platinum layer prepared by ion beam deposition. Subsequently, two trenches at both sides of place of interest and material at the front of place of interest are prepared by ion beam. Then the parameters of focused ion beam are adjusted and high quality cross–section is prepared. Automatic procedure allows to slice material with very low step of the removed layer together with taking micrographs of high quality cross–section. This procedure results in a set of micrographs, which has to be cropped and aligned and consequently 3-D micrograph is obtained, see figure 86b. 3-D micrograph revealed short period of "stage I" propagation. The crack inclined 45 degree to the specimen surface only a few micrometeres in maximum, then crack becomes perpendicular direction to the specimen surface (stage II of crack propagation).

(a)   (b)
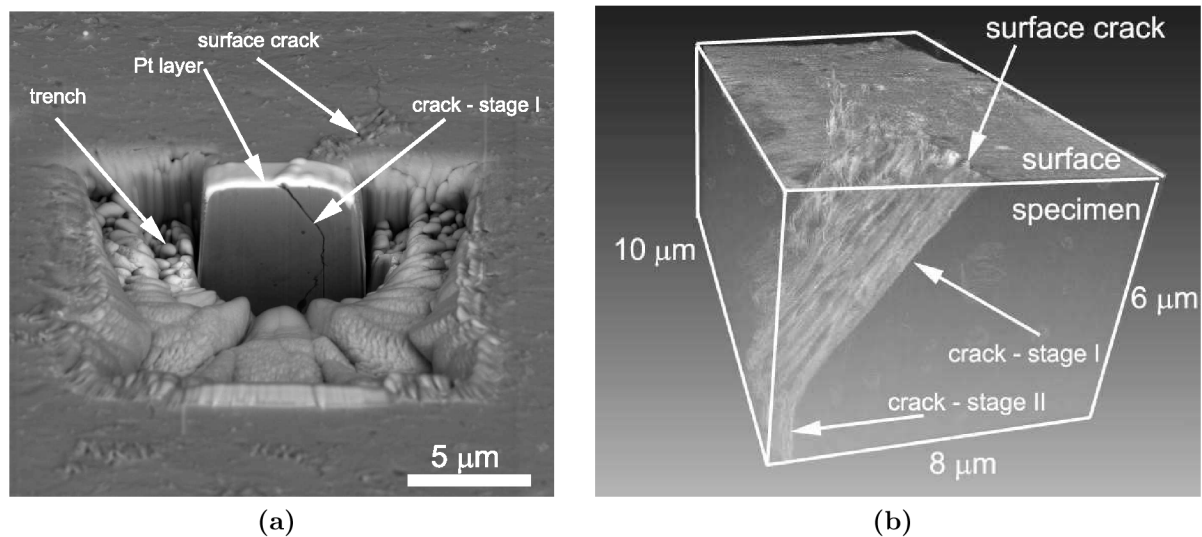
Figure 86: a) An example of the slice prepared using FIB with marked trenches, Pt protective layer and surface crack; b) 3-D image composed from particular slices with marked growing stages

4.8.2   Small crack growth rate

The small crack growth rate was measured in six specimens from the ODS Eurofer steel and in four specimens from the CEA steel at RT. The measurement was not performed in the EPFL steel, because of the lack of specimens. Examples of light microscopy micrographs are shown in figures 87 and 88. Both micrographs were taken in specimens loaded by strain amplitude equal to 0.5 %. Pre–cracks prepared by FIB technique are clearly visible in both cases. Crack started to grow after some initiation period which is obviously shorter in the CEA steel. The small fatigue crack growth rate is significantly higher in the CEA steel than in the ODS Eurofer steel. Compare number of cycles and crack length in right parts of figures 87 and 88. The crack length is marked in micrographs too.
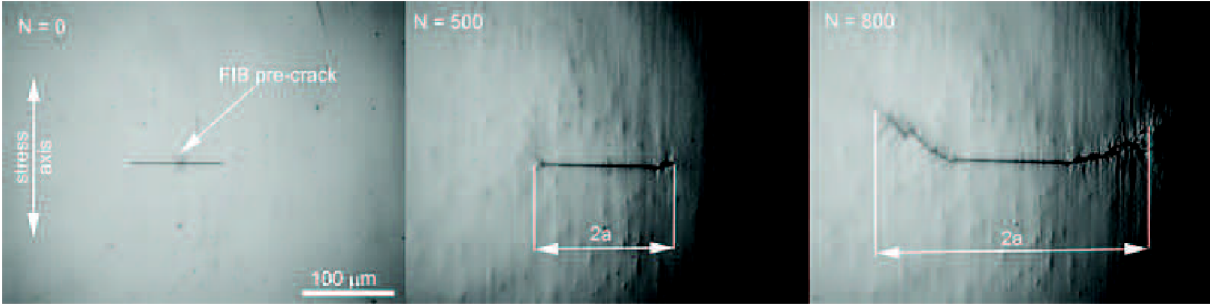
Figure 87: Three light microscopy micrographs taken in different number of cycles N in the CEA steel loading with $\varepsilon_a = 0.5$ %, length of pre–crack $a_{FIB} = 100$ μm
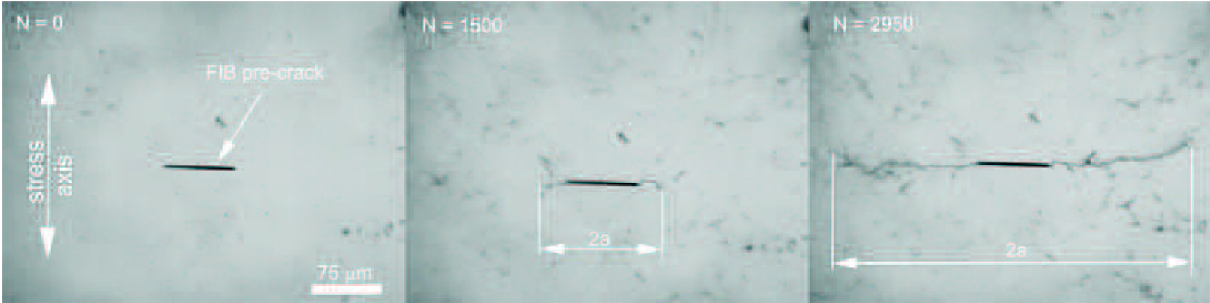
Figure 88: Three light microscopy micrographs taken in different number of cycles N in the ODS Eurofer steel loading with $\varepsilon_a = 0.5$ %, $a_{FIB} = 75$ μm

The crack length a was defined as half length of the surface length crack projection into the direction perpendicular to the specimen axis. Crack length was measured in particular intervals during cycling which were adjusted to the crack growth rate to obtain at least twenty pairs of crack length and number of cycles between the onset of cycling and the fracture. Examples of dependence of crack length on the number of cycles for total strain amplitude $\varepsilon_a = 0.5$ % and $\varepsilon_a = 0.6$ % are shown in figures 89 and 90, respectively. The exponential curve fits measured data very well in all cases, which was found for others materials too [55, 56, 71, 72, 73]. Experimental data were fitted by equation 13, (see section 2.3.6), where a_i and k_g are free parameters which were determined by regression analysis. Their values together with ε_a and ε_{ap} are given in Table 9. It is obvious that the

fatigue crack growth coefficient k_g increases with increasing ε_a and ε_{ap}. Theoretical value of pre-exponential parameter a_i should be equal to length of FIB notch, nevertheless it varies substantially, which is common in fitting of exponential functions.
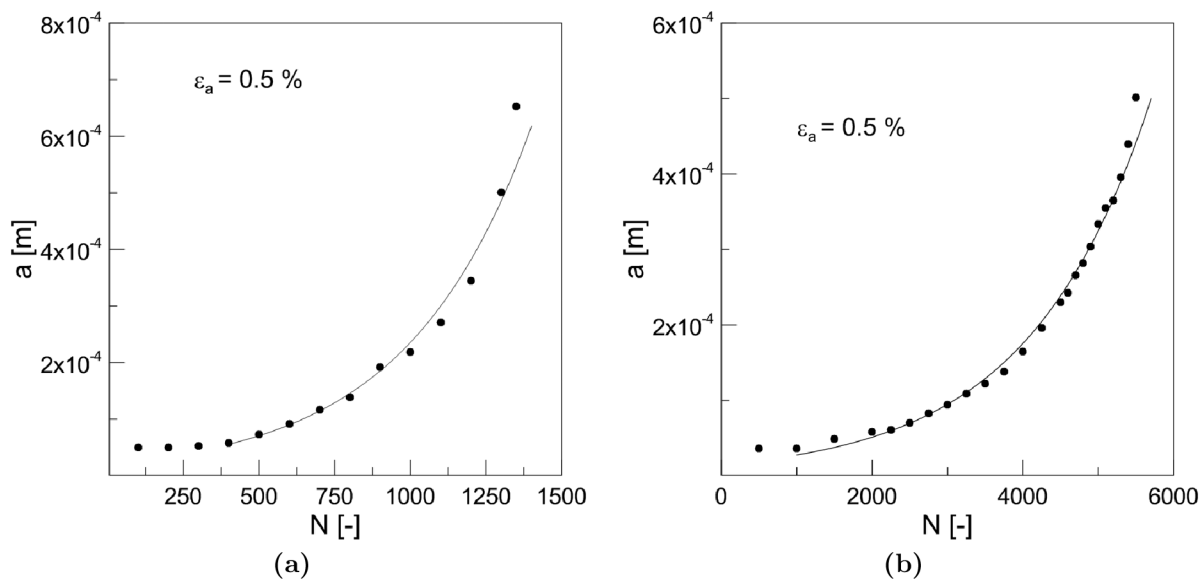
Figure 89: Crack length as a function of number of cycles with exponential fit for strain amplitude $\varepsilon_a = 0.5$ %. a) the CEA steel, b) the ODS Eurofer steel
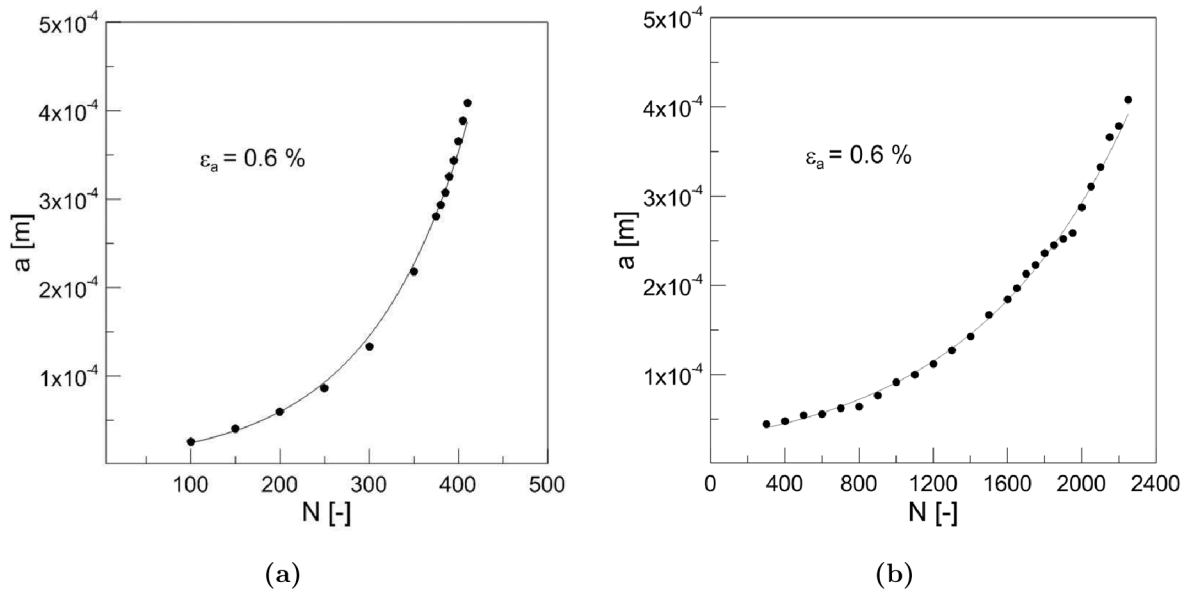
Figure 90: Crack length as a function of number of cycles with exponential fit for strain amplitude $\varepsilon_a = 0.6$ %. a) the CEA steel, b) the ODS Eurofer steel

Table 9: Small crack growth results

	ε_a [%]	ε_{ap} [-]	k_g [-]	a_i [m]
ODS Eurofer L	0.4	$2.5{\times}10^{-4}$	$4.3{\times}10^{-4}$	$3.65{\times}10^{-6}$
ODS Eurofer L	0.5	$5.5{\times}10^{-4}$	$7.0{\times}10^{-4}$	$2{\times}10^{-5}$
ODS Eurofer L	0.6	$9.6{\times}10^{-4}$	$9.0{\times}10^{-4}$	$2{\times}10^{-5}$
ODS Eurofer T	0.37	$1.3{\times}10^{-4}$	$2.2{\times}10^{-4}$	$1.67{\times}10^{-5}$
ODS Eurofer T	0.5	$5.6{\times}10^{-4}$	$5.9{\times}10^{-4}$	$1.64{\times}10^{-5}$
ODS Eurofer T	0.6	$1.1{\times}10^{-3}$	$9.1{\times}10^{-4}$	$2{\times}10^{-5}$
CEA steel	0.37	$4.36{\times}10^{-5}$	$3{\times}10^{-4}$	$1{\times}10^{-8}$
CEA steel	0.4	$1.1{\times}10^{-4}$	$1.2{\times}10^{-3}$	$8.8{\times}10^{-6}$
CEA steel	0.5	$5.16{\times}10^{-4}$	$3{\times}10^{-3}$	$2.1{\times}10^{-5}$
CEA steel	0.6	$1.68{\times}10^{-3}$	$1.3{\times}10^{-2}$	$1{\times}10^{-5}$

5 Discussion

5.1 Strengthening effect of oxide particles

The oxide particles are very small but represent strong obstacles for dislocations motion. The average diameter d of particles was measured as 2.1 nm and 2.3 nm by groups which produced materials in the EPFL and in the CEA, respectively. The mean distance between particles in glide plane x_g was estimated to be 30–40 nm from TEM micrographs as well as from simple geometrical model. This estimation can be done by following steps:

1. The specific weight of Y_2O_3 phase of 5.03×10^3 kgm^{-3} is known. 0.3 % of mass fraction of oxides corresponds to the volume fraction of 0.47 %.

2. Let's assume that the surface fraction of oxide particles in the slip plane is also 0.47 % and that the particles are arranged in square lattice and that their size is constant and equal to 2.5 nm.

3. Using these assumptions and known parameters, the distance between first neighbours is 32.3 nm.

These assumptions are not completely realistic, especially the information about the particle distribution is missing and also the real size distribution is not taken into account. Nevertheless, a value of x_g about 30–50 nm can be estimated and it corresponds with TEM observation. These two parameters, d and x_g, have the strongest influence on strengthening effect.

Several mechanism how dislocation can overcome a particle have been proposed. In the case of small and coherent precipitates dislocation can cut the precipitate. Stress necessary for this event $\Delta\tau_{cut}$ is given by Eq. 21 [74]. Otherwise, dislocation bows gradually between two precipitates until loops around particles are formed. Such mechanism is called Orowan bypassing [75]. The required stress $\Delta\tau_{Orowan}$ corresponds to the maximum line tension during bypassing, see Eq. 22 [74]. The Arzt–Rösler–Wilkinson mechanism (local climb of dislocation over obstacle) needs activation of diffusion. It was introduced as the strengthening mechanism for creep of ODS superalloys at high temperatures [76, 77, 78]. The idea is that local climb of the dislocation over obstacle is easy (at least at long creep exposition) and the increase of stress $\Delta\tau_{Arzt}$ equals to the stress necessary to separate dislocation from the obstacle, the attractive obstacle vs. dislocation interaction is assumed.

The increase of stress corresponding to individual mechanisms can be evaluated using following equations:

$$\Delta\tau_{cut} = \frac{\gamma\pi d}{2bx_g} \tag{21}$$

$$\Delta\tau_{Orowan} = \alpha\frac{Gb}{x_g - d} \tag{22}$$

$$\Delta\tau_{Arzt} = \frac{Gb}{x_g}\sqrt{1 - k^2} \tag{23}$$

where G is shear modulus, x_g is distance between particles, b is Burges vector, d is particle diameter, γ is surface energy of planar fault of oxide particle created by dislocation passing, α is a coefficient depending on the dislocation character and k is relaxation factor. Parameter k can be of the range between one if there is no attractive interaction between obstacle and dislocation (then the strengthening by Arzt–Rösler–Wilkinson mechanism is negligible due to easy diffusion) and zero when dislocation is inseparable from obstacle then the strengthening is the same as in the case of the Orowan mechanism.

Estimation of d and x_g was already presented. Burgers vector in iron bcc lattice is equal to 0.248 nm. The coefficient α has typical value between 0.5 and 1. It was chosen to be 1 in our case [74]. The surface energy γ of randomly cut of Y_2O_3 was calculated by atomistic simulation as 20 J/m^2 [79]. This value is very high and it is explained by the necessity of breaking strong covalent bonds between Y and O. Considering isotropic material, shear modulus G can be calculated using measured Young modulus E by formula $G = E/2(1 + \nu)$, where ν is a Possion ratio.

The increase of stress due to oxide particles in case of cutting particle was calculated (Eq. 21) as 10 GPa. This value is even higher than theoretical shear stress for iron computed using ab initio calculations as 7.2 GPa [80] or 7.5 GPa [81]. This result together with general knowledge that particle cutting usually occurs only in case of small coherent particles lead to the conclusion that cutting of oxide particles by dislocations is not possible in studied steels.

In spite of the fact that the Orowan and Arzt–Rösler–Wilkinson mechanism are based on different physical ideas, Eqs. 22 and 23 are mathematically similar. The particle diameter d is missing in Eq. 23 but it can be neglected due to its small size. It means that strengthening effect of both mechanism is similar. To distinguish which mechanism participates on plastic deformation or if they work simultaneously is a question for TEM analysis. At RT, the probability of local dislocation climb or dislocation climb generally is very low, almost negligible. For this reason, the Arzt–Rösler–Wilkinson mechanism is not probable at RT. Then small dislocation loops around particles generated during deformation by Orowan mechanism should be found in microstructure. Unfortunately, size of dislocations loops in case of such small particles is under resolution of our transmission electron microscope, so we are not able to confirm or disprove their existence. Nevertheless, the Orowan mechanism most likely plays the main role during dislocation motion at RT.

If theoretical increase of stress due to oxide dispersion is calculated using Eqs. 22 and 23, the value of about 650 MPa in both cases is found. This value should be multiplied by the Taylor factor $M = 3.06$ to obtain theoretical tensile stress increase at RT, $\Delta\sigma_{Orowan} \approx$ 2 GPa. This theoretical value is about four times higher then measured value (about 450 MPa). It can be explained either by inhomogeneous distribution of oxide particles so volumes with lower particles density can be deformed at lower stress, or by variation of particle size so the number of particles can be lower if bigger particles are present leading to additional inaccuracy in x_g and d estimation. Paul et al. [82] showed in the ODS Eurofer steel the inhomogeneity of particle distribution without quantitative analysis. Moreover, there is some uncertainty in estimation of parameters α and k too.

Other authors have tried to evaluate Orowan stress at RT in the MA957 steel strengthened with 0.25 wt. % of yttria oxide particles with slightly different formulations. Mala–

plate et al. [83] calculated $\Delta\tau_{Orowan} = 376$ MPa while Sakasegawa et al. [84] considered the statistical distribution of particle size and mean distances among particles and give values of $\Delta\tau_{Orowan}$ from 200 to 300 MPa. It can be thus concluded that:

- difference of stress levels of ODS and non–ODS steels can be explained by oxide particles strengthening. Other differences in microstructure as grain size or dislocation density may participate on strengthening effect, but they are not necessary to explain the observed strengthening.

- cutting of particle is impossible so the Orowan mechanismus of overcoming obstacles is expected at RT.

At elevated temperatures, the two ODS ferritic steels show higher strength than the ODS Eurofer steel. The stress necessary for Orowan mechanisms differs from the RT value only due to changes of G with temperature. Therefore, we can calculate:
at RT: $\Delta\tau_{Orowan} = 450$ MPa (as measured)
at 650 ℃: $\Delta\tau_{Orowan} = 308; 273$ MPa (ferritic; ferritic/martensitic matrix)
at 750 ℃: $\Delta\tau_{Orowan} = 251; 220$ MPa (ferritic; ferritic/martensitic matrix)
It can be compared with the $R_{p0.2}$ of the ODS steels given in table 4. $R_{p0.2}$ of the Eurofer 97 steel at 650 ℃ was estimated as 220 MPa [19]. It is less than the expected value of the Orowan mechanism above. It seems that this mechanism is no longer active at 650 and 750 ℃.

The question if the Arzt–Rösler–Wilkinson mechanism operates at elevated temperatures, or what is the minimum temperature for activation of this mechanism in condition of low cycle fatigue has been investigated by several authors. Steckmeyer et al. [30] estimated the transition from Orowan to Arzt–Rösler–Wilkinson mechanism for the ODS 14Cr ferritic steel at 500-600 ℃, based on the comparison of calculated and observed stresses. By the same method, Reppich [85] determined this transition for ODS MA 754 Ni- based superalloy at 750 ℃. For the material studied in this work, the Arzt–Rösler–Wilkinson mechanism is likely the decisive strengthening mechanism for the deformation at 650 and 750 ℃. HRTEM is necessary to confirm or reject this possibility.

5.2 Cyclic properties

5.2.1 Cyclic hardening/softening curves, comparison with literature

The cyclic softening of ferritic/martensitic (FM) steels were documented by many authors. The 9Cr FM steel called P91 was cycled at 600 ℃ by Saad et al. [86]. They confirmed cyclic softening and fatigue life was divided into three parts. Rapid decrease of stress amplitude in first cycles followed by "stable" continuous softening. Moreover, they tried to apply the Chaboche unified viscoplasticity [87] model for the description of second stage of fatigue life. The fatigue properties of the P92 (P92 and P91 differ only in W content) steel was studied by Giroux et al. [88]. The continuous softening was observed at 550 ℃. The P91 and P92 steels were compared in the Manson–Coffin plot, no big influence of W content was observed, in spite of the fact that P92 exhibits higher strength. The higher cyclic strength of P92 in comparison with P91 at 550 ℃ was confirmed also by

Fournier et al. [89]. The effect of W content on cyclic behaviour of 9Cr FM steels was studied by Park et al. [90]. The continuous softening was observed in all materials studied by Park at all testing temperatures. Moreover, the cyclic softening rate increased with increasing temperature. The increasing W content results in higher strength at all testing temperatures (RT and 600 ℃). On the other hand, the higher W content did not mean the longer fatigue life. It was observed that the longest fatigue life exhibits material with content of W 1.8 % at all studied temperatures. The material with 2.7 % of W exhibits only slightly higher strength but significantly shorter fatigue life. It can be summarised that significant cyclic softening is general feature for all FM steel under all testing conditions.

RAFM steels were widely studied [89, 91, 92]. The development of RAFM steels resulted in two most promising variant of 9Cr, namely Eurofer 97 and F82H. These two steel differ slightly in chemical composition. Unfortunately, the cyclic softening persists in these steels [14, 16] with the same three stages as described by Saad et al. [86]. The attempt to reduce cyclic softening by higher Cr content was carried out. It resulted in higher strength of materials, but the influence on cyclic softening was not as big as it was expected. Moreover, the undesirable delta ferrite appeared in microstructure in steels with high content of Cr [12].

Recently, RAFM and RAF steels strengthened by dispersion of fine oxides were produced. Contrary to the RAFM and RAF, the information about cyclic behaviour of ODS steels are rare in literature. It was expected that oxide dispersion will improve cyclic strength and also it will suppress or even remove undesirable cyclic softening of ferritic/martensitic steels. The 9Cr martensitic ODS steel (equivalent to Eurofer ODS steel) and 12Cr ferritic steel were studied by Ukai [26]. Stable cyclic behaviour was documented in both steels. Their steels exhibit slightly lower strength than steels studied in this work. Nevertheless, Ukai's observation of stable cyclic response in the 9Cr martensitic steel are in the contradiction with results given in this work. Unfortunately, microstructural description is missing in [26]. On the other hand, stable behaviour of either 12Cr or 14Cr ferritic steels was confirmed as well as the fact that ferritic matrix has higher strength than the martensitic one.

The strengthening effect of oxide dispersion was documented in this work. The stress amplitudes are almost doubled in comparison with most non ODS RAFM steels which were mentioned in previous paragraph. It was proved in this work that oxide dispersion does not guarantee the stable cyclic behaviour, see softening curves measured in the ODS Eurofer steel in figures 48a and 50a. On the other hand, both ferritic steels exhibit stable behaviour or even slight cyclic hardening. This significant difference can be explained by the role of matrix.

5.2.2   Hysteresis loops analysis

The detailed analysis of the hysteresis loops offers an opportunity to reach additional information of fatigue behaviour of all materials. One possibility is to calculate so called V_H parameter proposed by Mughrabi [37], which describes the shape of the hysteresis loops during cycling (Eq. 7) and section 2.3.2. It was documented that in case of single crystals V_H reaches its minimum when the plastic strain localisation occurs and first PSBs

are formed [37, 93]. Another possibility is to use statistical approach proposed by Polák [35, 54, 94]. This approach divides crystalline material into microvolumes which under equal strain carry different stresses. Sum of particular stresses represents overall behaviour of material. The stress distribution is characterised by the probability density function which can be determined from the first and the second derivative of the hysteresis half loop. It is possible also to separate effective and internal stresses [35, 54, 94].

The V_H parameter was calculated for all studied materials and all testing condition, nevertheless, only the highest and the lowest amplitudes at RT and at 650 ℃ are presented in figures 91a, 93a and 95a to keep these plots uncluttered.

The V_H parameter evolution measured in the **CEA steel** is shown in figure 91a. The V_H parameter continuously decreased for all testing conditions with exception of specimen cycled at RT with $\varepsilon_a = 0.7$ %. The slight decrease of the V_H parameter at 650 ℃ corresponds with slight hardening which is documented in figure 53a. The hardening rate as well as the decrease of the V_H parameter is relatively small at 650 ℃. The surprising difference was revealed at RT. Specimens cycled with the highest total strain amplitude $\varepsilon_a = 0.7$ % exhibit the increase of the V_H parameter during first 100 cycles, then it seems to saturate. This feature can be explained by following facts. Two hysteresis loops are shown in figure 91b, for $N = 4$ cycles and for $N = 400$ cycles. Obviously, the stress amplitude is almost identical for both loops, as well as the plastic strain amplitude. The main differences between presented loops are marked by arrows. The applied stress increases with number of cycles in marked region. This feature can be explained by statistical analysis proposed by Polák [94]. Changes in marked region can be connected with the changes of both stress components. The effective stress is possible to measure from either the first or the second derivative, see figure 92. With respect to the shape of the second derivative, it can be said that effective stress increased during cycling, see
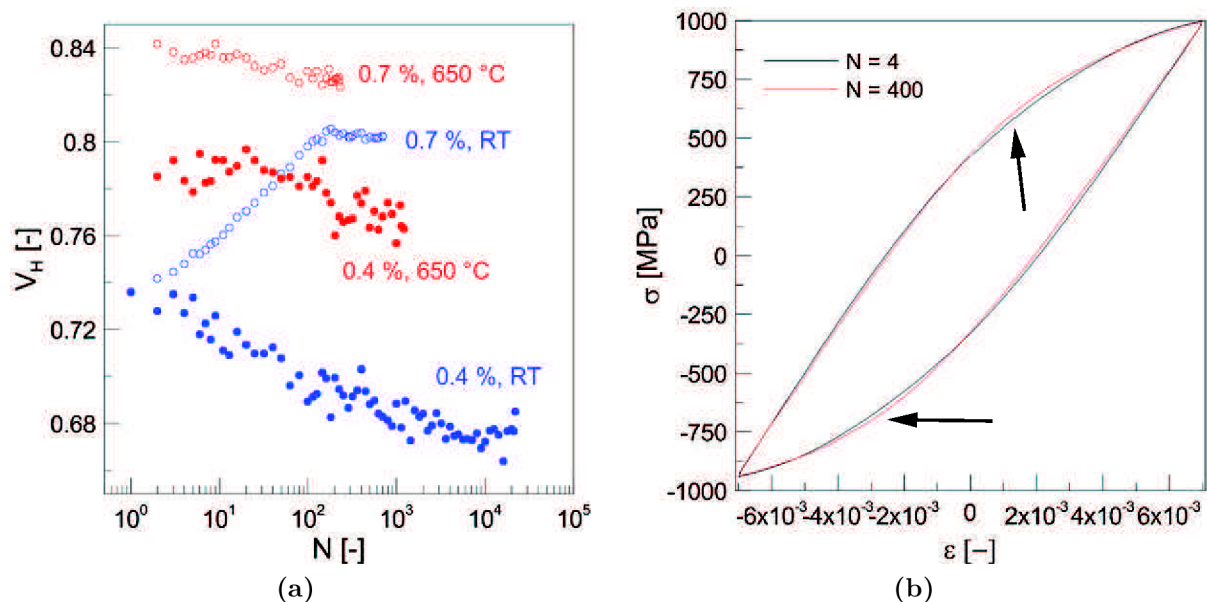
Figure 91: a) V_H parameter as a function of number of cycles in the CEA steel; b) hysteresis loops for $N = 4$ and $N = 400$ obtained at RT in the CEA steel

the first minimum in figure 92b. Moreover, the first maximum of the second derivative is shifted to the right for higher number of cycles. It means that less microvolumes are deformed plastically under given stress, in other words, some microvolumes became more strength during cycling. This feature was observed only in specimens cycled by the amplitude of 0.7 %.
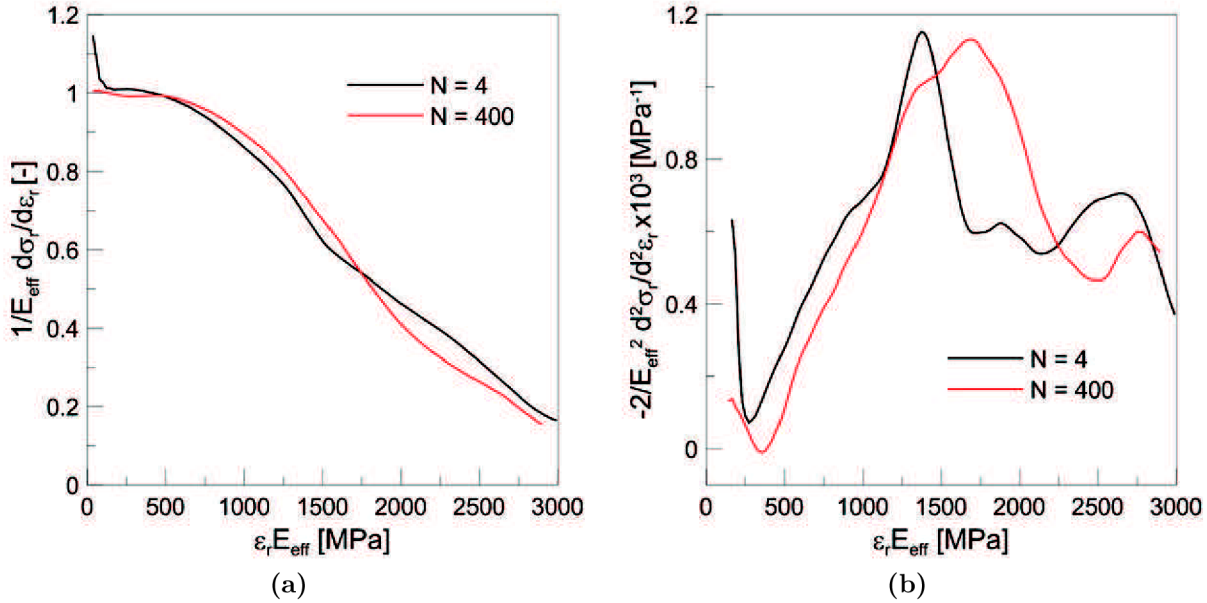
Figure 92: a) The first derivative for tensile part of hysteresis loop in the CEA steel; b) The second derivative for tensile part of hysteresis loop in the CEA steel

It should be emphasised that basic testing control software was used resulting in lower number of point per hysteresis loop than it would be necessary. It means that the trend (whether effective stress increasing or decreasing during cycling) can be estimated, but advanced control software allowing sufficient number of points per hysteresis loop should be used for the determination of accurate values of effective stress.

The V_H parameter evolution in specimens cycled with low amplitudes at RT exhibits similar trend as in specimens cycled at 650 ℃, in spite of the fact that this specimen exhibits stable cyclic behaviour and specimens cycled at 650 ℃ cyclically harden. The V_H parameter was very useful in this case because slight and not obvious changes in hysteresis loops shape would stay hidden.

The V_H parameter evolution measured in the **EPFL steel** is shown in figure 93a. The V_H parameter continuously decreased for all testing conditions with exception of specimen cycled at RT with $\varepsilon_a = 0.7$ % as well as in the CEA steel. Nevertheless, the explanation of this anomaly is not so obvious as in the case of the CEA steel. The cyclic softening under this testing conditions is documented in figures 54a and 93b. The first and the second derivative measured in specimen cycled with $\varepsilon_a = 0.7$ % is shown in figure 94. Plato is present in the first derivative (figure 94a, which allows to estimate effective Young modulus E_{eff} and both stress components can be separated. It was estimated that effective stress under this testing conditions continuously decreases with number of cycles. Contrary, the effective stress was found to be rather constant in specimen cycled
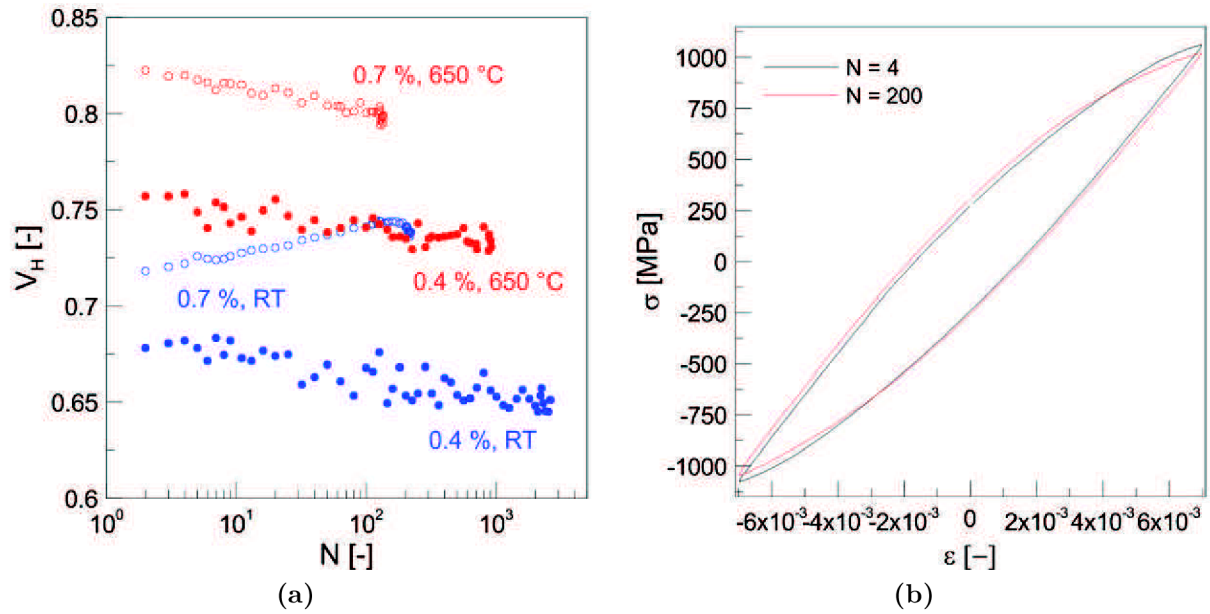
Figure 93: a) V_H parameter as a function of number of cycles in the EPFL steel; b) two hysteresis loops for $N = 4$ and $N = 200$ obtained at RT in the EPFL steel
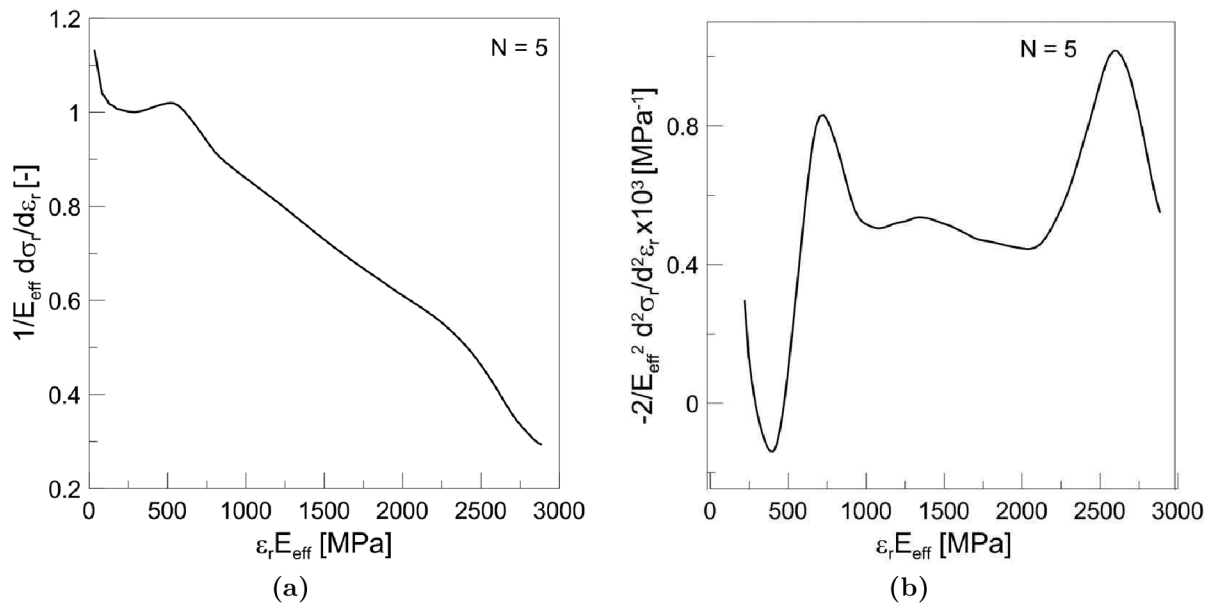
Figure 94: a) First derivative measured in the EPFL steel with $\varepsilon_a = 0.7$ %; b) second derivative in the EPFL steel

at RT with $\varepsilon_a = 0.4$ %.

The V_H parameter as a function of number of cycles measured in the **ODS Eurofer steel** is shown in figure 95a. The significant difference between low strain and high strain amplitude region at RT is present as well as others studied steels. For $\varepsilon_a = 0.7$ %, the V_H parameter is constant with number of cycles, whilst it decrease more rapidly for the $\varepsilon_a = 0.4$ % than in case of ferritic steel. Statistical analysis revealed that effective

stress continuously decreased with the number of cycles at RT. The decrease in strength of some microvolumes which is caused by both, destroying of low angle boundaries in the microstructure and by surface relief formation due to cyclic straining (microvolumes containing surface relief are considered to be less strength than matrix). An example of the first and second derivative measured with $\varepsilon_a = 0.7$ % is shown in figure 95.

(a)

(b)

(c)
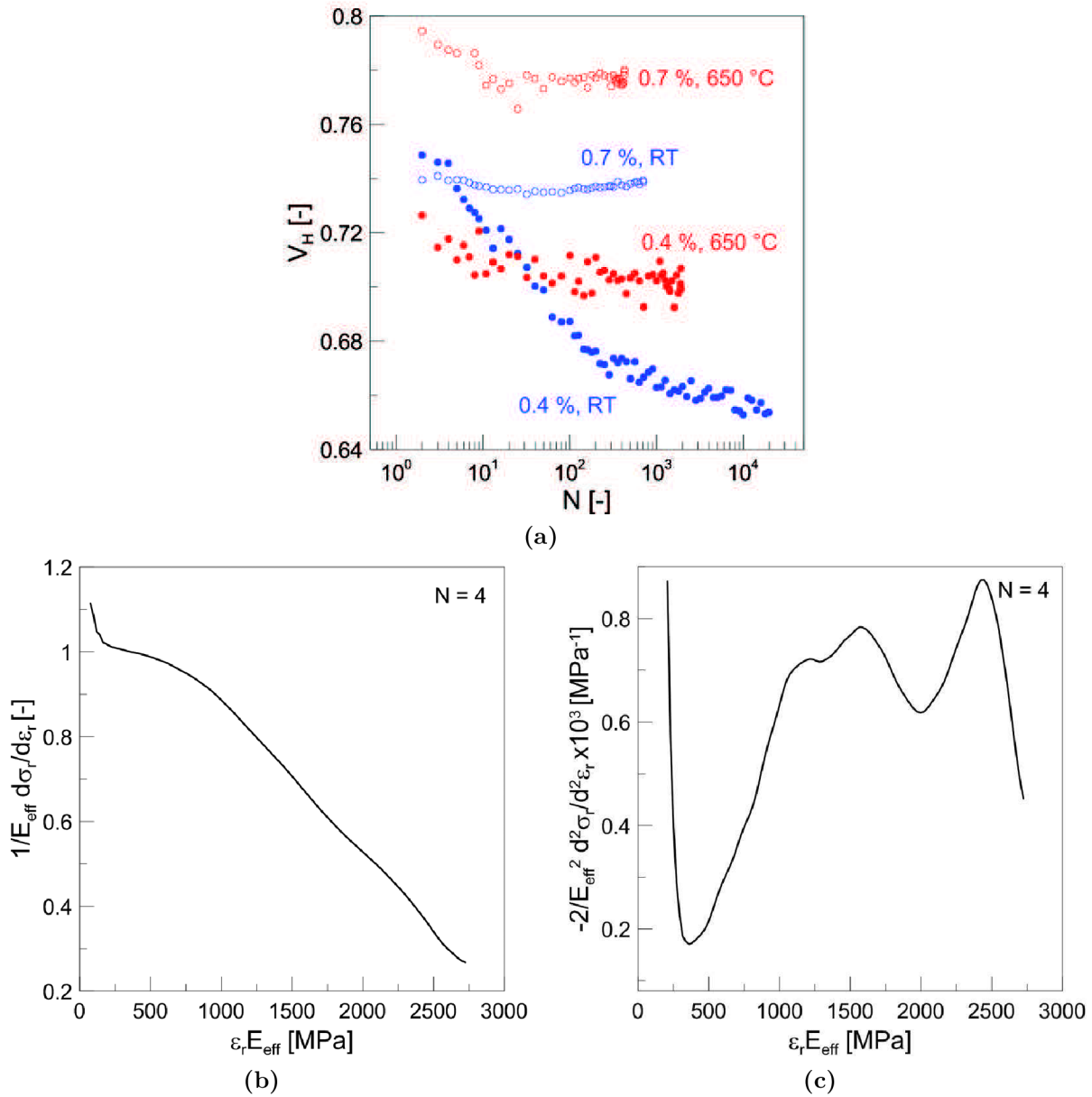
Figure 95: a) V_H parameter as a function of number of cycles in the ODS Eurofer steel; b) First derivative ODS Eurofer steel; c) second derivative in the ODS Eurofer steel

Comparison with literature

The statistical analysis was performed on both ferritic and austenitic steels, nevertheless, these steels consisted grains of conventional size [95, 46, 96]. Such analysis have not been performed on UFG material yet.

In all studied materials, the second derivation contained two local positive peaks at RT. The first one is correlated with E_{eff} and the second one was explained by Polak et al. [96]. It was documented that the second peak represents magnetoelastic effect and this peak can be suppress if external magnetic field is changed.

5.3 Changes in microstructure due to fatigue loading

5.3.1 As–received state

The microstructure of studied steels is described in section 4.2.1. The microstructure of the ODS Eurofer steel consists of small grain/subgrain of size of 0.72 μm. This value is in agreement with subgrain size measured by other authors in the Eurofer 97 steel [15, 16, 17, 97]. Most of the microstructure of the Eurofer 97 is composed of equiaxed subgrains having a size around 0.7 μm, the grain size of the prior austenitic grain was measured as 12 μm. This value is relatively small in comparison with another RAFM steel F82H (80 μm). Mutual microstructural properties of the ODS Eurofer steel and the Eurofer 97: carbides are present and decorates grain/subgrain boundaries, the dislocation density is comparable, areas with similar crystallographic orientation exceeding grain size were found. These steels differ most importantly in presence of oxide dispersion.

On the other hand, only high angle boundaries were found in both ferritic steels. The microstructure of the CEA steel in as–received state was studied by Steckmeyer [30] too. The microstructural description of the ferritic steels given in this work and given in [30] is almost identical. The elongated grains were found too, the grain size in direction perpendicular to the extrusion axis was measured to be 0.55 μm. The as–received state of similar bimodal ferritic ODS steel was studied by Baluc [98]. The grain size of larger grains was estimated as 3 μm and the smaller grains as 0.5 μm. This is in agreement with results presented in this work, only the grain size of small grains was lower, 0.34 μm, in this work. Dislocation density in both ferritic steels is high.

5.3.2 Microstructural changes due to fatigue loading

The ODS Eurofer steel

According to the literature, the microstructural changes in RAFM steels due to fatigue loading can be summarised as follows: the martensitic laths are decomposed into subgrains, which are dislocation free and size of subgrains are better defined, some individual dislocations can be found in smaller subgrains which seems not to be deformed plastically, overall dislocation density decreased, mean size of subgrains may change during cycling in relation to te stress amplitude [15, 16, 97].

The oxide dispersion was added to RAFM steels to stabilise microstructure during (fatigue) loading with the consequence of removal undesirable cyclic softening. Oxides obviously present strong obstacles for dislocation glide. Contrary to the non–strengthened RAFM steel, dislocations pinned by oxides were found inside grains after fatigue loading,

it means that dislocation density does not decrease as dramatically as in case of the e.g. Eurofer 97 steel. The coarsening of some grains was observed in this work, figure 67. The final grain size depends on the applied plastic strain amplitude (or stress amplitude) and temperature as well as in case of the Eurofer 97 steel [97]. Nevertheless, final grain size is smaller in the ODS Eurofer steel than it the Eurofer 97 steel and their occurrence in microstructure is less frequent under given testing conditions. Since the surface relief was formed due to fatigue loading, an attempt to study the microstructure directly under surface relief was performed, figure 85b. 3-D dislocation structures such as ladder, vein or labyrinth are usually formed in materials with conventional grain size in areas of cyclic plastic strain localisation [27, 99]. The minimum grain size necessary for formation of these dislocation structures was estimated as 0.5 - 1 μm by Holste [100]. Grain size measured in the ODS Eurofer steel is in this interval. It leads to the conclusion that no 3-D dislocation patterns should be formed. This assumption was confirmed in figure 85b. No arranged dislocation patterns were found in the microstructure after fatigue loading. The area with surface relief was of about 3 μm in this case which means that it was formed in more than one grain (grain boundary is clearly visible) with similar crystallographic orientation. The detailed dislocation analysis was not possible because of the FIB damage.

The grain size increases during cycling at elevated temperatures more rapidly in both variants of the Eurofer steel, but faster in the Eurofer 97 steel. The grain size of the Eurofer 97 steel cycled at 550 ℃ [16] is similar as the mean grain size of the ODS Eurofer steel cycled at 650 ℃. Moreover, the grain size does not increase dramatically even in the ODS Eurofer steel specimen cycled at 750 ℃. Note that the stress levels are similar in specimen prepared from the Eurofer 97 steel cycled at 550 ℃ and in specimens cycled prepared from the ODS Eurofer steel at 650 ℃. This observation suggests that the Hall–Petch component of the strength of the ODS Eurofer steel is important at high temperatures. It can be noticed that the decrease of strength in the ODS Eurofer steel cycled at 750 ℃ is significant and unacceptable for real constructions. The overall dislocation density decreases less rapidly in the ODS Eurofer steel than in the Eurofer 97 steel [16] due to oxide dispersion. Dislocation pinned by oxide particles are documented in figures 67 or 69a. Some grains were found to be dislocation free. It is likely a question of homogeneity of oxide particles distribution.

These facts confirm the expectation that oxide particles in the RAFM steels could increase operating temperature of the RAFM steels of about 100 ℃.

The CEA steel
No significant changes in microstructure (grain size, dislocation density, . . .) due to fatigue loading at RT were found in the CEA steel. Considering the fact that no surface relief formation was found on specimen surface, it seems that deformation in the CEA steel occurred rather homogeneously and it might be partially reversible. No low angle boundaries were formed at RT due to cyclic plastic straining. Contrary to the ferritic steels with conventional grain size [101, 102] where ordered dislocation structures were formed, no 3-D dislocation arrangements were detected, only some individual dislocations were caught by oxide dispersion. These fact caused high cyclic strength and cyclic stable behaviour of the CEA steel at RT.

At 650 ℃, size of some grains increased as well as the dislocation density in some

grains. Tilt and twist low angle boundaries (LAB) were found in microstructure (figure 72) and their formation is explained in figures 96 and 97. The tilt LAB is formed quite simply by a wall of edge dislocations with the same $\vec{b}$. Attractive and repulsive forces among dislocation result in stable arrangement which is shown in figure 96b and it create a tilt rotation of angle ω. The formation of a twist LAB is shown in figure 97b. Dislocation segments with Burgers vector $[\bar{1}11]$ and $[1\bar{1}1]$ reacts and dislocation with Burgers vector $[001]$ is formed (dashed line in figure 97b). This reaction is energetically advantageous and it happens in (110) plane. Hexagonal net is created by one family of <001> and two families of <111>dislocations and it caused twist rotation of vector ω, see figure 97a. Both LAB boundaries represent additional obstacle for dislocations and can contribute to strengthening effect if such boundaries were created during cycling.

In spite of the fact that some high angle boundaries disappeared, it seems that number of obstacles for dislocations increased resulting in slight cyclic hardening. The high angle boundaries are substituted by dislocation pinned by oxides and also by both types of low angle boundaries. The dislocation slip seems not to be reversible anymore, diffusion and thermally activated processes have to be taken into account.

(a)   (b)

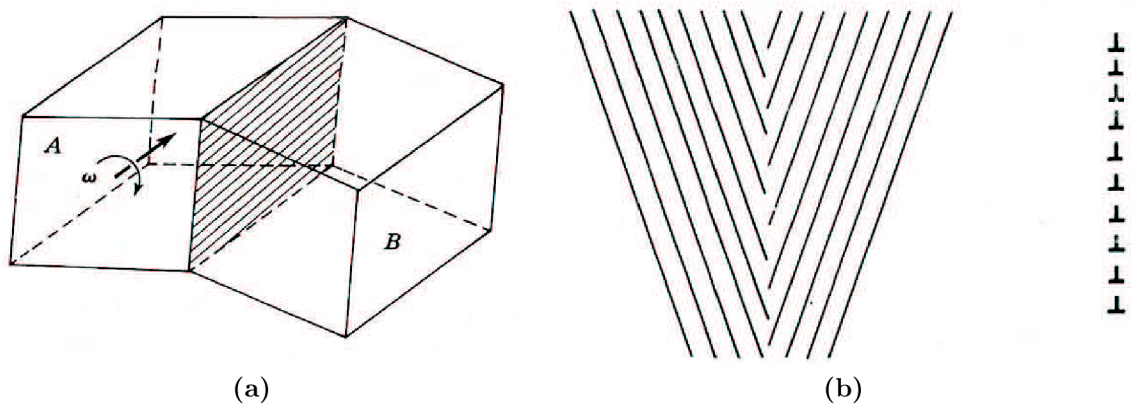**Figure 96:** a) Tilt LAB; b) dislocation scheme of twist boundary on (110) plane in bbc crystal [74]

(a)   (b)
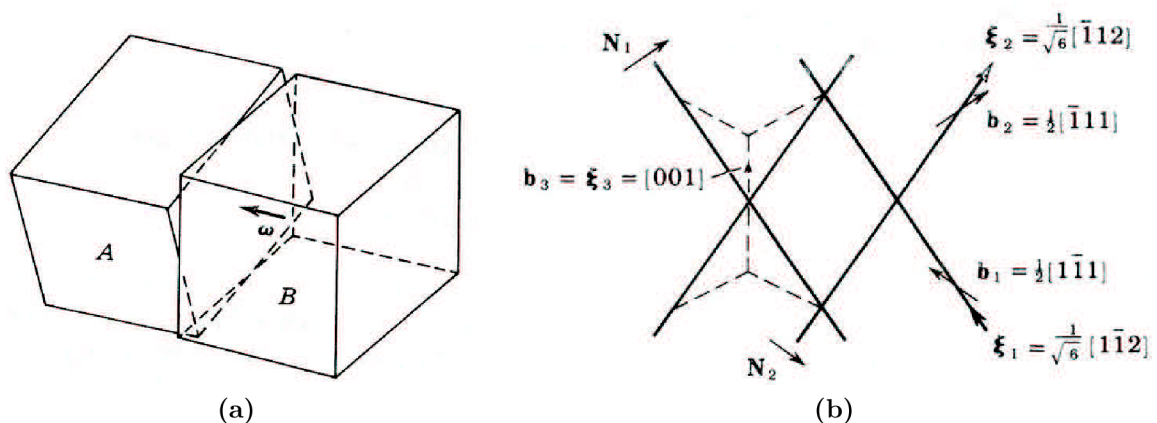
Figure 97: a) Twist LAB; b) dislocation scheme of twist boundary on (110) plane in bbc crystal [74]

The EPFL steel

Particular parts of the bimodal structure were deformed in different ways. Areas of small grains seem not to be affected by cyclic plastic strain deformation. Statistical analysis revealed that the grain size of smaller grains did not change due to fatigue loading at all testing temperatures. It means that the deformation took place preferably in bigger grains. The grain size of bigger grains did not increased during cycling. Moreover, the dislocation arrangement in interior of the grains was slightly changed. Bigger grains were almost dislocation free before fatigue loading. In fact, three types of grains were found in microstructure after fatigue loading. The first one which remained almost dislocation free (figure 75b), the second one which were full of dislocations (figure 76) and the third one where tilt LAB were found (figure 74c). No ordered 3–D dislocation patterns were detected. Even though some changes were found in microstructure due to fatigue loading, their influence on fatigue behaviour is not strong, which is consistent with stable cyclic behaviour described in section 4.3.3.

5.4   Surface relief formation and fatigue crack initiation

The three materials prepared by powder metallurgy differ substantially in the microstructure, which influences crack initiation too. The surface observation revealed a striking difference in the fatigue crack nucleation and early fatigue crack growth for the studied materials which are clearly related to the grain size and geometry. The grains in the CEA steel are elongated and have a quite uniform diameter in the transverse plane (mean value of 0.49 μm). No surface relief formation due to the cyclic loading was observed. Indeed, it was reported that in grains under 1 μm, the low-energy 3D dislocation arrangements in the form of e.g. walls and channels are not formed [100, 103] because the characteristic dimensions of such structures are comparable or bigger than the grain size. No weak zones (as persistent slip bands in coarse grained materials) inside the grains are therefore formed, see figures 81a or 82a. The nucleation of the fatigue crack is difficult; the length of initiated crack is short and the early growth of cracks is slowed by frequent high angle boundaries.

In the bimodal EPFL steel, equiaxed grains reach even smaller grain size (0.34 μm) than in the case of the CEA steel, but regions with grains about 3 μm in diameter were documented. The surface of some of the largest grains roughened during cycling, causing local stress concentration. The fatigue cracks nucleate as a rule within the large grain regions, preferentially along the interface between highly plastically deformed grains and the surrounding material, see figure 83a. The nucleation period is therefore shortened and the size of nucleated crack is longer than in case of the CEA steel. Also, the small crack growth through the large grains and along the grain boundaries is easier (both inter- and transgranular growth was observed). These factors shorten the fatigue life of the material with bimodal grain size distribution of one order of magnitude in comparison with the material having uniform elongated grains.

The microstructure of the ODS Eurofer steel is characterised, in variance with the two ferritic steels, by a high number of low angle grain boundaries. The surface relief is formed (figure 80b) in a similar way as in the EPFL steel. The fatigue crack nucleation occurred within surface relief. It is supposed that since this material has lower strength than the

EPFL steel, the small crack growth rate is lower. It was confirmed in section 5.5.1 that small fatigue cracks grow faster in ferritic matrix than in the ferritic/martensitic one.

The surface relief observations of bcc steels with grains under 1 μm are missing in literature. Let's try to compare studied steels with materials which have something in common with studied steels. Surface relief due to fatigue loading in bcc high Cr steels with conventional grain is formed by thin persistent slip markings containing extrusions and intrusions [102]. In the case of two phase duplex steel, it was clearly documented that the localisation of cyclic plastic deformation is stronger and faster in the bcc phase which results into higher and more distinct PSM in the α phase then in the γ phase [104, 105]. The extrusions grow and the intrusions get deeper into material and represent suitable place for fatigue crack initiation. Nevertheless, this is a result of microstructural changes caused by cyclic plastic strain leading to particular dislocation arrangement. It was documented that no dislocation patterns are formed in studied steels. For this reason, it was not expected that PSM would appear on the specimen surfaces.

Another possibility how to prepare material with ultra fine grain (UFG) structure is severe plastic deformation (SPD) method. The surface relief formation was also observed in UFG copper prepared by ECAP [106]. Even though the shape of PSM is closer to the one which was observed in this work, there are sill significant differences. The height of PSM is higher than in studied steels in this work and the PSMs in UFG copper are thinner than that studied in this work. Moreover, PSMs in the UFG Cu exceed size of one grain where the PSMs are formed. It means that cyclic plastic strain localisation occurs in regions with similar crystallographic orientation. This situation can be compared with situation it the ODS Eurofer steel. The PSMs are not as much developed in the ODS Eurofer steel as PSMs in UFG copper. There are two reasons: i) the areas with similar crystallographic orientation are bigger in the Cu than in the ODS Eurofer steel; ii) the main difference lies in crystallographic lattice, Cu possesses the fcc lattice while studied steels bcc lattice.

5.5 Small crack growth

5.5.1 Polák's approach

The validity of exponential law (Eq. 13) proposed by Polák [73] implies that the fatigue crack growth rate is a linear function of the crack length, see Eq. 14. A dependence of fatigue crack growth rate on crack length and its linear fit is plotted in figure 98 for the specimens cycled with $\varepsilon_a = 0.6$ %.

It was proposed by Polák [73] that coefficient k_g is a function of plastic deformation only, for more details see section 2.3.6 and Eq. 15. Coefficients k_{g0} and d in Eq. 15 are material constants allowing easy description of growing crack. These coefficient were calculated as $k_{g0} = 5.66$ and $d = 0.96$ for the CEA steel and as $k_{g0} = 0.175$ and $d = 0.75$ for the ODS Eurofer steel. According to published data for other steels [54, 55, 56, 73] the value of exponent d was expected to be close to 1. This is consistent with results measured in the CEA steel.

The comparison of crack growth rate coefficient of both studied ODS steels and of non – ODS variant of Eurofer steel is plotted in figure 99. Obviously, the influence of

oxide particles on the crack growth rate generally and on coefficient k_g in particular is not strong. In spite of the fact that coefficient d varies, values of k_g are similar for both variants of Eurofer steels in studied interval of ε_{ap}. It seems that fatigue cracks grow faster in the ODS Eurofer steel under lower plastic strain amplitudes than in the Eurofer 97 steel. The crack growth rate coefficient is higher in the CEA steel in order of magnitude than in both variant of the Eurofer steel. Growth of fatigue cracks is faster in the pure ferritic matrix than in the tempered martensitic matrix. On the other hand, fatigue life
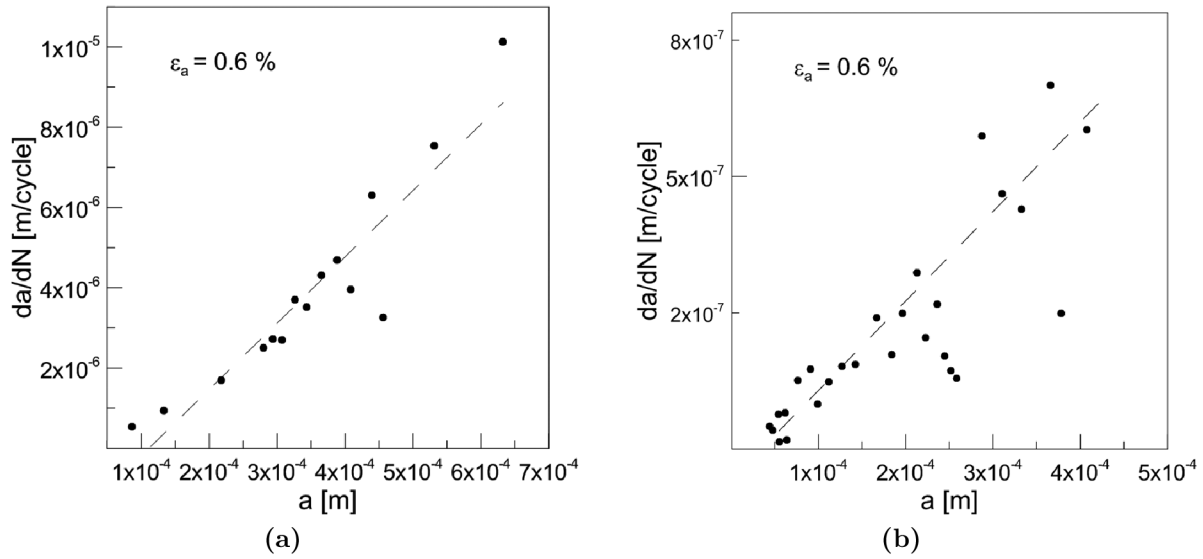

Figure 98: Fatigue crack growth rate as a function of crack length with linear fit for strain amplitude $\varepsilon_a = 0.6$ %. a) the CEA steel, b) the ODS Eurofer steel
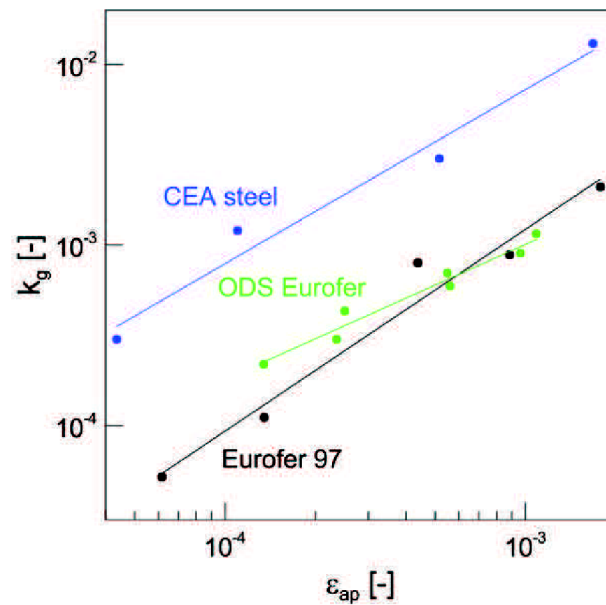
Figure 99: The comparison of fatigue crack growth coefficient measured in the CEA steel, the ODS Eurofer steel and in the Eurofer 97 steel

of the ODS Eurofer steel and CEA steel is similar under loading with the same plastic strain amplitude ε_{ap}, see 64a. This feature is discussed in section 5.6.

5.5.2 Validity of Tomkins law

Tomkins [107] in 1968 proposed a famous relation between parameters of cyclic stress-strain curve (σ_a and ε_{ap}) and the small fatigue crack growth rate. It is interesting that the Tomkins law (Eq. 24) predicts linear function between da/dN and the crack length a, as was observed in this work:

$$\frac{da}{dN} = \pi^2 \varepsilon_{ap} \left(\frac{\sigma_a}{2\overline{T}}\right)^2 \times a \left(1 + \frac{\pi^2}{2}\left(\frac{\sigma_a}{2\overline{T}}\right)^2\right) \tag{24}$$

where $\overline{T}$ is a parameter which norms the stress level for different materials. Combining this equation with the description of the cyclic stress-strain curve (Eq. 16), da/dN can be written as a function of σ_a or ε_{ap} only:

$$\frac{da}{dN} = f(\sigma_a) = \pi^2 \frac{\sigma_a^{2+1/n_b'}}{K_b'^{1/n_b'} 4\overline{T}} \times a \left(1 + \frac{\pi^2}{2}\left(\frac{\sigma_a}{2\overline{T}}\right)^2\right) \tag{25}$$

$$\frac{da}{dN} = f(\varepsilon_{ap}) = \pi^2 \left(\frac{K_b'}{2\overline{T}}\right)^2 \varepsilon_{ap}^{2n_b'+1} \times a \left(1 + \frac{\pi^2}{2}\left(\frac{K_b'}{2\overline{T}}\right)^2 \varepsilon_{ap}^{2n_b'}\right) \tag{26}$$

The dependence of fatigue crack growth rate on applied stress is stronger than on applied plastic strain, compare power $(2 + 1/n_b')$ and power $(2n_b' + 1)$. Except of $\overline{T}$, there is no other unknown free parameter in Eqs. 24, 25 and 26. For example, n_b' in the ODS Eurofer steel is 0.136 which implies that the small fatigue crack growth rate predicted according to Tomkins is $da/dN = f\left(\sigma_a^{9.4}\right)$ and as $da/dN = f\left(\varepsilon_{ap}^{1.14}\right)$.

This law has often been cited, however, it is not accepted by all scientific community. The law implies that, if $\overline{T}$ is known, it is possible to predict fatigue crack growth kinetics only from the cyclic stress–strain curve which does not seem realistic. On the other hand, the main characteristic of small fatigue crack growth are correctly described by Eq. 24:
– fatigue crack growth rate is a linear function of the crack length
– stress dependence of crack growth rate is stronger than the plastic strain dependence.
The meaning of the parameter $\overline{T}$ and how it can be measured is not entirely clear. According to Tomkins, $\overline{T}$ should be the stress level in the regions where the crack is growing, it means the tensile stress in the slip bands. Tomkins supposed that $\overline{T}$ could compare and normalise materials with different strength. However, other propositions for $\overline{T}$ can be found, e.g. equal $\overline{T}$ to the residual stress of the material after cyclic deformation [108] or to identify $\overline{T}$ with the cyclic yield stress $\sigma_{0.2}$.

In this work, da/dN was measured for number of specimens which gives an unique opportunity to to test the Tomkins law, because $\overline{T}$ can be evaluated in every case. The comparison of Eq. 14 and Eq. 24 implies Eq. 27:

$$k_g = \pi^2 \varepsilon_{ap} \left(\frac{\sigma_a}{2\overline{T}}\right)^2 \times \left(1 + \frac{\pi^2}{2}\left(\frac{\sigma_a}{2\overline{T}}\right)^2\right) \tag{27}$$

leading to equation of quadratic type:

$$\frac{\pi^4}{2}\varepsilon_{ap}\left(\frac{\sigma_a}{2\overline{T}}\right)^4 + \pi^2\varepsilon_{ap}\left(\frac{\sigma_a}{2\overline{T}}\right)^2 - k_g = 0 \tag{28}$$

Two roots of Eq. 28 can be found easily using appropriate substitution. The Eq. 28 was solved for all measured pairs of ε_{ap} and da/dN. In all cases, only one physically meaningful solution was uncovered. It was found that the parameter $\overline{T}$ varies for all testing conditions and it is a function of plastic strain amplitude, see figure 101. The
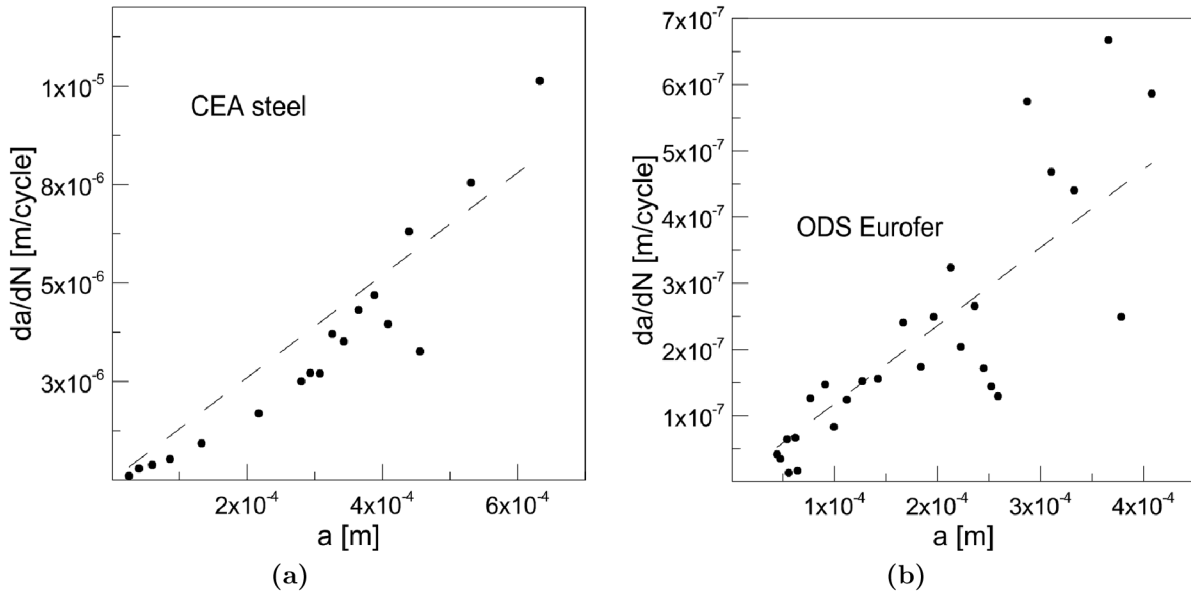
Figure 100: Fatigue crack growth rate as a function of crack length and linear fit using Tomkins law. a) the CEA steel, b) the ODS Eurofer steel
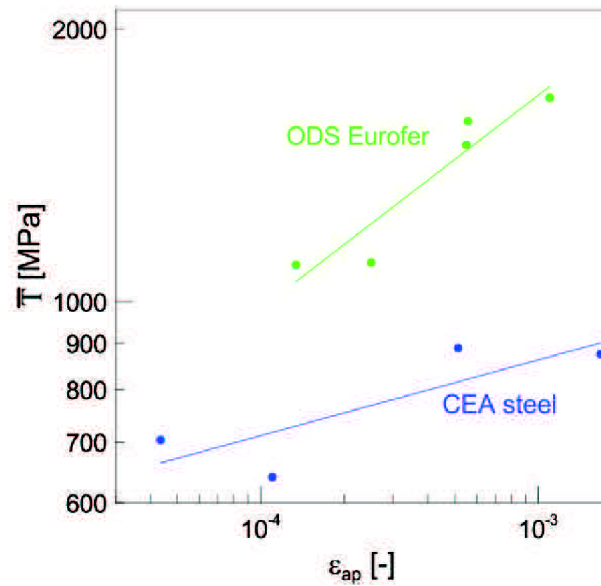
Figure 101: The parameter $\overline{T}$ as a function of ε_{ap}

trend in figure 101 is marked by lines, power law could be used for a fit. According to the presented plot, the dependence of $\overline{T}$ on ε_{ap} is strong in case of the ODS Eurofer steel. This was also declared by Tomkins himself [107], which leads to the conclusion that $\overline{T}$ could not be connected to any material characteristic. Experimental data of da/dN vs. a together with theoretical data calculated by Tomkins law (dashed line) are ploted in figure 100. The Tomkins law describes data in figure 100 quite well in this case, because the parameter $\overline{T}$ was the free parameter of the fit. For other amplitudes this particular value of the $\overline{T}$ is not valid at all. The usage of power function depending on plastic strain amplitude instead of simple value in Tomkins law would complicate Eq. 24 but it would make this law more general.

5.5.3   Fracture mechanics approach

The fracture mechanics is commonly used for residual fatigue life estimation of specimens containing crack. The linear elastic fracture mechanics (LEFM) was utilised in this work. This approach seems to be a bit more complicated than previous two, because the stress distribution in the vicinity of the crack tip has to be known. For purpose of this work, the one parameter LEFM was chosen and compared with above mentioned approaches for fatigue life estimation. The only parameter, the stress intensity factor K determines the stress field near the crack tip. The formula for calculation of stress intensity factor at the crack tip of a semicircular crack was derived by Broeck [109]

$$\Delta K = 1.12 \frac{2}{\pi} \Delta \sigma \sqrt{\pi a} \tag{29}$$

where ΔK is stress intensity factor range, $\Delta \sigma$ is stress range and a is crack length. Paris-Erdogan law [110] is used in the literature in several forms, see e.g. [111]. One
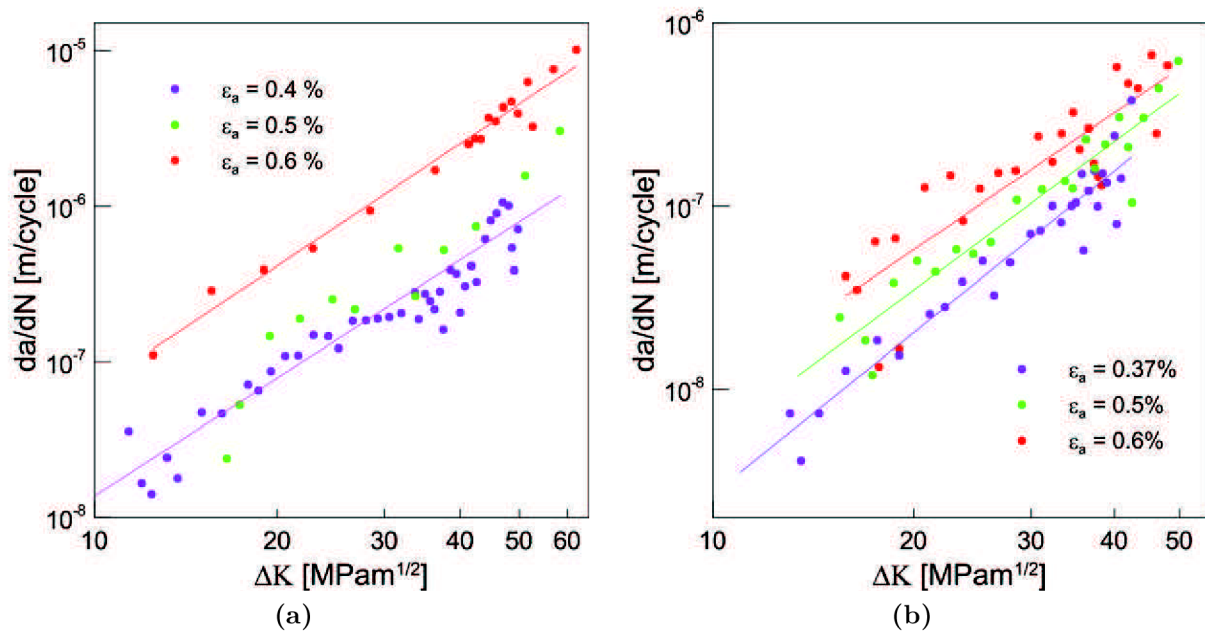
Figure 102: Paris - Erdogan plot a) the CEA steel, b) the ODS Eurofer steel

variant is given in Eq. 30. It can be used for the estimation of fatigue crack propagation kinetics:

$$\frac{da}{dN} = C \left(\frac{\Delta K}{\Delta K_0} \right)^m \tag{30}$$

where C and m are coefficients of Paris–Erdogan law and $\Delta K_0 = 1$ MPam$^{1/2}$ is introduced in order to keep constant C dimensionless. The dependences of experimental data da/dN on calculated ΔK of studied materials and for three different amplitudes are shown in figure 102. Coefficients $m = 2.5$ and $C = 4.1 \times 10^{-11}$ were determined from measured data for two lower amplitudes in the CEA steel, but $m = 2.6$ and $C = 1.7 \times 10^{-10}$ for the highest amplitude, respectively. The slope m is similar for all amplitudes and varies fromm 2.48 to 2.91 and parameter C varies from 3.1×10^{-12} to 3.4×10^{-11} in the ODS Eurofer steel. The range of values of m and C is relatively small, nevertheless it is statistically significant. According to LEFM definition, only one curve with unique parameters should be obtained for given material for test at all ε_a. Moreover, it was shown by Lardner [112] that coefficient m should be equal to 2 for exponentially growing crack. The measured values of m are not far from this predicted value. The most important fact visible in figure 102 is that the fatigue crack growth rate for different amplitudes is not the same for the same ΔK. It can be explained by the fact that the small scale yielding condition near crack tip is not fulfilled. This can be proved by plastic zone size estimation in case of plane strain condition, see Eq. 31 [113]:

$$R_y = \frac{1}{2\pi} \left(\frac{K_I}{R_{0.2}} \right)^2 \tag{31}$$

The condition for validity of linear elastic fracture mechanics is that the plastic zone size should be smaller than $1/10$ of the crack length a [114]. It was verified that the condition is not fulfilled for all measured cracks. Calculated plastic zone size is approximately equal to the with crack size. In spite of this facts, LEFM can be used for preliminary estimation of coefficient m in Paris – Erdogan law. The elasto – plastic fracture mechanics approach based on the J–integral concept should be used for higher accuracy of fatigue life estimation [113, 115, 116]. This approach was successfully used in [117], where the comparison of small and long crack growth in the Eurofer 97 steel is presented. It is planned to repeat such computations with steels studied in this work in the near future.

5.5.4   Comparison of discussed methods

It can be summarised that three models of fatigue crack growth are presented and discussed in terms of their usability and physical meaning for given analysis.

The Polák's model offers an opportunity to determine material constants describing the growth of small cracks. The validity of proposed law was confirmed in literature as well as in this work. This model does not need more or less complicated solution of the stress field at the fatigue crack tip, which is advantageous and it makes determination of material constants easier. This approach is purely phenomenological, based on i) experimental observation of exponential dependence of a on N and ii) hypothesis that k_g is a power

function of ε_{ap}. Nonetheless, it was proved in several works that this description agrees well with the reality.

The fatigue crack growth law proposed by Tomkins is a function of applied stress and plastic strain amplitudes, which seems to be more accurate. However, Tomkins law can be presented also as a function of either ε_{ap} or σ_a only using parameters of cyclic stress–strain curve, see Eq. 25 and 26.

It was shown that one parameter linear elastic fracture mechanics condition is not fulfilled, but this approach can be used for determination of starting point for more complicated elasto–plastic fracture mechanics approach.

5.6 Fatigue life

5.6.1 Estimation of number of cycles necessary for crack initiation

The fatigue life N_F can be divided into two important periods, the fatigue crack initiation period N_i and the fatigue crack growth period N_{cg}.

$$N_F = N_i + N_{cg} \tag{32}$$

The fatigue life is terminated either by final fracture or by state when specimen or component stops fulfilling its function (e.g. in strain controlled loading when the fatigue cracks exceed their critical length).

The ratio between this two periods can vary significantly depending on the material. Measurement of short fatigue crack growth rate offers an opportunity to measure exactly N_i. As a definition, based on the surface observation, N_i is defined as the number of cycles necessary for the major crack to grow to 50 or 100 μm. The model proposed by Tanaka and Mura can be used for estimation of number of cycles necessary to initiate a fatigue crack [118, 119]. They derived equation which determines the number of cycles necessary

Table 10: Small crack growth results, the first line in each measured amplitude represents ratio between N_i and N_{cg} for initiation crack length of 50 μm, the second line of 100 μm.

	ε_a [%]	ε_{ap} [-]	N_F	N_i	N_{cg}	$\frac{N_i}{N_F}$[%]	$\frac{N_{cg}}{N_F}$[%]	α [nm]
CEA steel	0.4	1.1×10^{-4}	27000	24503	2497	91	9	0.58
				25080	1920	92	8	0.6
CEA steel	0.5	5.16×10^{-4}	16200	15200	1000	95	5	7.9
				15432	768	95	5	8
ODS Eurofer	0.37	1.3×10^{-4}	32100	18421	13679	57	43	1.0
				21586	10514	67	33	1.2
ODS Eurofer	0.4	2.5×10^{-4}	20300	13333	6967	66	34	2.4
				14945	5355	73	27	2.7
ODS Eurofer	0.5	5.5×10^{-4}	6050	1770	4280	29	71	1.5
				2761	3289	46	54	2.4
ODS Eurofer	0.5	5.6×10^{-4}	6700	1622	1622	24	76	1.5
				2797	3903	41	59	2.5

to initiate fatigue crack. Their formula was modified [120] in order to take into account grain size and plastic strain range, see Eq. 33:

$$N_i = \frac{\alpha}{d}\frac{1}{\Delta\varepsilon_p^2} \tag{33}$$

where d is grain size, α is thermally dependent coefficient and $\Delta\varepsilon_p$ is plastic strain range. This formula contains two potential sources of inaccuracy. The first one lies in determination of coefficient α, its definition is not clear. The second one lies in the essence of Tanaka and Mura model. Tanaka and Mura theory is based on microstructural evolution due to cyclic plastic strain which results into persistent slip markings on the specimen surface. It was documented that surface relief in the ODS Eurofer steel and EPFL steel is formed in not common way of persistent slip markings. Contrary, the surface relief formation was not detected in the CEA steel. In spite of these uncertainties, we tried to use Eq. 33 for comparison of N_i of the studied materials. Considering the same plastic strain range and the same value of α, number of cycles necessary for fatigue crack initiation increases with decreasing grain size. It is in agreement with results obtained in this work. It is possible to estimate the number of cycles necessary for the crack to grow to 50 or 100 μm (N_i) from the knowledge of small crack growth rate. Practically, N_{cg} was defined as the number of cycles necessary for small fatigue crack growth from 50 or 100 μm to 1 mm of crack length. Then N_i was calculated as N_F - N_{cg}, where N_F is number of cycles to failure of smooth specimen. Subsequently, the coefficient α can be calculated from Eq. 33. Calculated values of N_i, N_{cg} their ratios and coefficient α are given in table 10. Surprising values of the coefficient α were found. While average value of $\alpha = 2$ were calculated for all strain amplitudes in the ODS Eurofer steel, very different values characterise the behaviour of the CEA steel. Because all parameters in Eq. 33 are measured with reasonable error or scatter, α values are calculated quite precisely. The differences of α for the two testing conditions of the CEA steel are therefore difficult to understand. It seems that Eq. 33 does not give consistent prediction in our case.

In spite of the fact that differences in grain size of the CEA steel and the ODS Eurofer steel are rather small, the initiation part is significantly longer in the CEA steel ($d =$ 0.49 μm) than in the ODS Eurofer steel ($d = 0.72$ μm) for both chosen length of initiating cracks, see table 10. It suggests that Eq. 33 is not suitable for UFG materials. The fact that small fatigue crack growth rate is significantly higher in the CEA steel than in the ODS Eurofer steel is documented in figure 99. It was found that initiation period in the CEA steel occupies more than 90 % of total fatigue life and this values seems to be independent of applied strain amplitude. Considering crack length of 100 μm, the initiation period in the ODS Eurofer steel occupies significantly smaller part of fatigue life, for example 45 % and 75 % of fatigue life under $\varepsilon_a = 0.5$ % and 0.4 %, respectively. The initiation period is even shorter if starting crack of 50 μm is considered. Contrary to the CEA steel, the stage of small crack growth occupies substantial part of fatigue life in the ODS Eurofer steel.

5.6.2 Comparison with fcc UFG materials

The current knowledge of the fatigue behavior of the UFG materials documents that development of bimodal microstructure by well designed heat treatment might lead to mild reduction of saturated stress level but important improvement of ductility which is reflected by longer fatigue lives in the Coffin-Manson plot. Most significant studies are in agreement in this point (see e.g. reviews [121] and [122]). In this work, bimodal structure si found to be clearly unfavourable Nevertheless, there are some important differences between case studies cited in [122] and the presented case:

- mostly fcc metals (Cu, Al) were studied but the ODS steels have bcc lattice

- UFG produced by severe plastic deformation (ECAP) were studied but the ODS steels are produced by powder metallurgy which implies differences e.g. in the grain boundary characteristics. Many low-angle boundaries are created by the ECAP procedure while almost uniquely high angle boundaries are a consequence of powder metallurgy technology

- main strengthening mechanism are different: reduction of the grain size in the ECAP materials and the presence of oxide particles in the ODS materials

- the surface relief due to cyclic loading is evolved in ECAP copper irrespective of the grain size distribution but it is developed only in the largest grains in the ODS materials.

The last point is apparently the reason of shorter fatigue life of the material with bimodal grain size distribution: the evolution of surface relief facilitates the crack nucleation which is the longest stage of the fatigue life of high–strength materials as was also found in the CEA steel, see table 10. Also, the small fatigue cracks grow preferentially along the interface between highly plastically deformed grains and the surrounding material in the EPFL steel. These two effects result in reduction of the fatigue life of one order of magnitude.

5.6.3 Understanding of fatigue life of studied steels

Detailed description of fatigue behaviour of studied steel was presented. Let's try to use obtained knowledge for explanation of fatigue life at RT of studied materials.

As it was written in previous section, fatigue life can be divided into two stages. It was documented that fatigue crack initiation is facilitated by surface relief formation. Such places were found in the ODS Eurofer steel and the EPFL steel, no surface relief formation was observed in the CEA steel. Together with theory of Tanaka and Mura, it leads to conclusion that initiation period should occupy the longest part in the CEA steel (no surface relief and the smallest grains), the shortest part in the EPFL steel (surface relief and the biggest grains) and of the mean part in the ODS Eurofer steel (surface relief in regions with similar crystallographic orientation, small grains). The small fatigue crack growth rate is significantly faster in the CEA steel than in the ODS Eurofer steel. Even though the small fatigue crack growth rate was not measured in the EPFL steel, it could

be estimated that this rate could be similar to the one measured in the CEA steel. This hypothesis is based on ferritic matrix of the CEA steel and the EPFL steel.

Taking into account these facts and hypothesis, differences in the fatigue life of studied steels can be explained. The shortest life time measured in the EPFL steel (see figure 103) is caused by combination of two "negative" aspects. Fast crack initiation period is expected due to surface relief formation (SEM observation) and also due to existence of big grain in microstructure (Tanaka and Mura). Together with fast fatigue crack growth rate, it causes the shortest fatigue life under given ε_{ap}. In spite of the fact that it was documented that stages of fatigue life in the ODS Eurofer steel and in the CEA steel are substantially different, both steels exhibit almost the same fatigue life in the Coffin–Manson plot. High fatigue crack growth rate in the CEA steel is compensated by the long crack initiation period when compared with the ODS Eurofer steel. This idea can be taken also from other side so the loss in fatigue life due to fast crack initiation in the ODS Eurofer steel is substituted by slow crack growth.

The knowledge of both parts of fatigue life allows the fatigue life prediction or, which is more interesting in running construction, the estimation of residual fatigue life. The description of the first part of fatigue life N_i and of the second part of fatigue life N_{cg} are discussed in details in this work. From the engineering or safety point of view, the ODS Eurofer steel is more beneficial, because slowly growing crack can be detected easier than fast crack growing in the CEA steel. It also means that service period could be longer in the ODS Eurofer steel than in the CEA steel with the same level of risk. On the other hand, the cyclic softening and lower strength are limitations of the ODS Eurofer steel. The best selection of the material depends on specific application, one could say that it is ever open question.
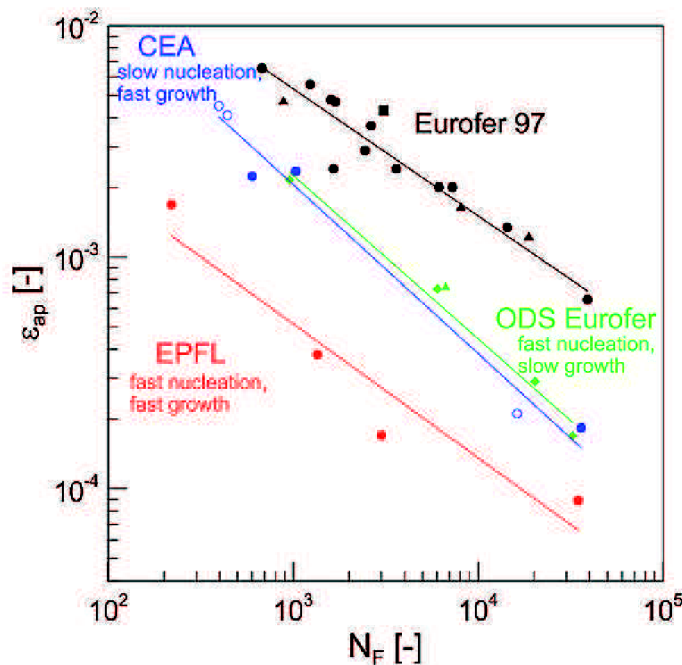
Figure 103: Coffin–Manson plot of studied steel at RT with fatigue life explanation

6 Conclusions

The main conclusions can be summarised in following points:

1. Microstructure of as–received state

   - Ultrafine–grained microstructure was revealed in all studied steels. The characteristics of microstructural unit and void size were measured.
   - The matrix of the tempered ferritic–martensitic ODS Eurofer steel consists of decomposed martensitic lath, which are decorated by carbides.
   - The pure ferritic matrix was found in the CEA steel. Equiaxed grains were found in section perpendicular to the extrusion axis, grains are elongated in section parallel to the extrusion axis.
   - The microstructure with bimodal grain size distribution is formed in the purely ferritic EPFL steel.

2. Hardening/softening curves

   - The oxide dispersion strengthens material significantly.
   - Cyclic softening was observed at all testing temperatures in the ODS Eurofer steel. Softening rate increases with increasing strain amplitude and decreasing temperature.
   - The CEA steel exhibits stable behaviour at all testing temperatures, slight cyclic hardening was observed at elevated temperatures.
   - Stable behaviour with exception of the highest amplitude at RT was observed in the EPFL steel.
   - Operating temperature of ODS steels can be increased of about 100 ℃ in comparison with the Eurofer 97 steel.

3. Fatigue behaviour

   - The strengthening effect of oxide particles results in high stress levels in cyclic stress–strain curves. Ferritic–martenistic microstructure is less strength than purely ferritic ones at all testing temperatures.
   - The ODS Eurofer steel and the CEA steel exhibits similar resistance to cyclic plastic straining.
   - The EPFL steel exhibits the highest cyclic strength but the shortest fatigue life among studied ODS steels, especially at RT.

4. Microstructure evolution due to fatigue loading

   - No 3-D dislocation arrangement were formed due to fatigue loading in all studied steels.

- The overall dislocation density decreased during fatigue loading of the ODS Eurofer steel at all testing temperatures. Grain size increased due to destruction of low angle boundaries by cyclic plastic straining. The mean grain size increases more rapidly at elevated temperatures: the higher temperature, the bigger grains were found in the microstructure. Two types of big grains (dislocation free and with high dislocation density) were distinguished after fatigue loading at elevated temperatures.

- No significant changes in microstructure were found in the CEA steel after fatigue loading at RT. At 650 °C, some grains grew to the diameter of about 1 μm. Nevertheless, statistical analysis proved that this growth is not statistically important. Dislocation density slightly decreased at both testing temperatures.

- Dislocation density decreased at all testing temperatures in small grains in the EPFL steel. Two types of bigger grains were found in microstructure, the ones with very high dislocation density and the one almost dislocation free.

5. Surface relief formation and fatigue crack initiation

- The surface relief formation was observed in areas with similar crystallographic orientation in the ODS Eurofer steel. Fatigue crack initiated within surface relief. The surface relief formation facilitates fatigue crack initiation.

- No surface relief was formed in the CEA steel during cycling. Fatigue crack initiated in voids. Some shear bands were observed at the fatigue crack tip.

- The surface of bigger grain were roughened in the EPFL steel. Crack usually initiated at the interface between regions of small and big grains.

6. Small crack growth rate measurement

- The small fatigue crack kinetics was measured in the ODS Eurofer steel and the CEA steel.

- Exponential growth of crack with number of cycles was observed in both steels. It implies fact that crack growth rate is a linear function of crack length.

- Parameters k_{g0} and d were determined.

- The small crack growth rate is the same in the Eurofer 97 steel and in the ODS Eurofer steel. The oxide particles have no influence on fatigue crack growth rate in this case. The fatigue crack growth rate is significantly faster in the CEA steel than in the ODS Eurofer steel.

- Tomkins law was analysed in order to test its validity.

- One parameter linear fracture mechanic was found insufficient for accurate description of growing fatigue crack in the studied steels.

7. Fatigue life in the Coffin–Manson plot

- The shortest fatigue life among studied steels was measured in the EPFL steel. The explanation lies in the surface relief formation which facilitated the fatigue crack initiation and in the fast fatigue crack growth rate in ferritic steels.

- The fatigue life of the CEA steel and the ODS Eurofer steel is almost the same. Nevertheless, the fatigue process is completely different. Fast fatigue crack growth rate is compensated by difficult crack initiation in the CEA steel while relatively short fatigue crack initiation period is compensated by slow rate of fatigue cracks in the ODS Eurofer steel.

7   Ivo Kuběna – list of selected publications

[I] KUBĚNA, I.; KRUML, T. Fatigue properties and crack growth in Eurofer steel. *Materials Engineering*, 2009, vol. 16, 3a, p. 32–36.

[II] KUBĚNA, I.; KRUML, T.; HUTAŘ, P.; NÁHLÍK, L.; SEITL, S.; POLÁK, J. Únavové vlastnosti oceli Eurofer vyvíjené pro fúzní energetiku. In *METAL 2009, Hradec nad Moravicí, CZ, 19-21 May 2010.* Paper no. 136. ISBN 978-80-87294-04-8.

[III] MAN, J.; WEIDNER, A.; KUBĚNA, I.; VYSTAVĚL, T.; SKROTZKI, W.; POLÁK, J.. Application of FIB technique to study of early fatigue damage in polycrystals. *Journal of Physics: Conference Series*, 2010, vol. 240, issue 1, p. 1–4.

[IV] KUBĚNA, I.; KRUML, T.; SPÄTIG, P.; BALUC, N.; OKSIUTA, Z.; PETRENEC, M.; OBRTLÍK, K.; POLÁK, J. Fatigue behaviour of ODS ferritic-martensitic Eurofer steel. *Procedia Engineering*, 2010, vol. 2, p. 717–724.

[V] KRUML, T.; KUBĚNA, I.; POLÁK, J. Fatigue behaviour and surface relief in ODS steels. *Procedia Engineering*, 2011, vol. 10, p. 1685–1690.

[VI] KUBĚNA, I.; KRUML, T.; FOURNIER, B.; POLÁK, J. Low cycle fatigue behaviour of ODS steels for nuclear application. *Key Engineering Materials*, 2011, vol. 465, p. 556–559.

[VII] KUBĚNA, I.; FOURNIER, B.; KRUML, T. Effect of microstructure on low cycle fatigue properties of ODS steels. *Journal of Nuclear Materials*, 2012, vol. 424, p. 101–108. IF = 2.052.

[VIII] MAN, J.; VYSTAVĚL, T.; WEIDNER, A.; KUBĚNA, I.; PETRENEC, M.; KRUML, T.; POLÁK, J. Study of cyclic strain localization and fatigue crack initiation using FIB technique. *International Journal of Fatigue*, 2012, vol. 39, p. 44–53. IF = 1.546.

[IX] KUBĚNA, I.; KRUML, T. Fatigue life and microstructure of ODS steels. *Engineering Fracture Mechanics*, Accepted manuscript, in print. IF = 1.353.

[X] ČERNÝ, M.; STRACHOTA, A.; CHLUP, z.; SUCHARDA, Z.; ŽALOUDKOVÁ, M.; GLOGAR, P.; KUBĚNA, I. Strength, Elasticity and Failure of Composites with Pyrolyzed Matrices Based on Polymethylsiloxane Resins with Optimized Ratio of D and T Components. *Journal of Composite Materials*, 2012, in print. IF = 1.068

References

[1] ITER – the way to new energy [online]. [quoted. 2012-10-01]. Accessible form WWW: http://www.iter.org/default.aspx

[2] KEILHACKE, M.; WATKINS, M. L.; JET-Team. D–T experiments in the JET tokamak. *Journal of Nuclear Materials*, 1999, vol. 266-269, p. 1–13.

[3] GIANCARLI, L.; et al. Breeding blanket modules testing in ITER: An international program on the way to DEMO. *Fusion Engineering and Design*, 2006, vol. 81, p. 393–405.

[4] LACKNER, K.; et al. Long–term fusion strategy in Europe. *Journal of Nuclear Materials*, 2002, vol. 307–311, p. 10–20.

[5] EHRLICH, K.; MÖSLANG, A. IFMIF – An international fusion materials irradiation facility. *Nuclear Instruments and Methods in Physics Research B*, 1998, vol. 139, p. 72–81.

[6] TIVEY, R.; et al. ITER divertor, design issues and research and development. *Fusion Engineering and design*, 1999, vol. 46, p. 207–220.

[7] PACHER, H.; et al. Erosion lifetime of ITER divertor plates. *Journal of Nuclear Materials*, 1997, vol. 241-243, p. 255–259.

[8] G.VIEIDER; et al. European development of the ITER divertor target. in *Proc. 20th SOFT, Marseille, 1998.*

[9] NORAJITRA, P.; et al. The EU advanced dual coolant blanket concept. *Fusion Engineering and Design*, 2002, vol. 61–62, p. 449–453.

[10] BUTTERWORTH, G. J.; JARVIS, N. O. Comparison of transmutation and activation effects in five ferritic alloys and AISI 316 Stainless steel in a fusion neutron spectrum. *Journal of Nuclear Materials*, 1984, vol. 122–123, p. 982–988.

[11] KASADA, R.; et al. Enhancement of irradiation hardening by nickel addition in the reduced-activation 9Cr2W martensitic steel. *Journal of Nuclear Materials*, 1998, vol. 256–263, p. 1199–1203.

[12] KLUEH, R. L. Reduced–activation bainitic and martensitic steels for nuclear fusion applications. *Current Opinion in Solid State and Materials Science*, 2004, vol. 8, p. 239–250.

[13] RENSMAN, J.; et al. Tensile properties and transition behaviour of RAFM steel plate and welds irradiated up to 10 dpa at 300 ℃. *Journal of Nuclear Materials*, 2002, vol. 307–311, p. 245–249.

[14] MARMY, P.; OLIVER, B. M. High strain fatigue properties of F82H ferritic–martensitic steel under proton irradiation. *Journal of Nuclear Materials*, 2003, vol. 318, p. 132–142.

[15] KRUML, T.; et al. Modelling of damage accumulation under cyclic loading. Study of nucleation and propagation of fatigue cracks. Comparison of physically short cracks against macroscopic cracks under cyclic fatigue. *Report on task TW6–TTMS–005 / Del. No. 7, December 2007, p. 43.*

[16] MARMY, P.; KRUML, T. Low cycle fatigue of Eurofer 97. *Journal of Nuclear Materials*, 2008, vol. 377, p. 52–58.

[17] SAUZAY, M.; et al. Cyclically induced softening due to low–angle boundary annihilation in a martensitic steel. *Materials Science and Engineering A*, 2005, vol. 400–401, p. 241–244.

[18] TONG, Z.; DAI, Y. The microstructure and tensile properties of ferritic/martensitic steels T91, Eurofer–97 and F82H irradiated up to 20 dpa in STIP–III. *Journal of Nuclear Materials*, 2010, vol. 398, p. 4348.

[19] LINDAU, R.; et al. Present development status of Eurofer and ODS–Eurofer for application in blanket concepts. *Fusion Engineering and design*, 2005, vol. 75–79, p. 989–996.

[20] LUCON, E.; et al. The European effort towards the development of a dome structural material: Irradiation behaviour of the European reference RAFM steel Eurofer. *Fusion Engineering and Design*, 2006, vol. 81, p. 917–923.

[21] KUBENA, I.; et al. Fatigue behaviour of ODS ferritic–martensitic Eurofer steel. *Procedia Engineering*, 2010 vol. 2, p. 717–724.

[22] YU, G.; NITA, N.; BALUC, N. Thermal creep behaviour of the Eurofer 97 RAFM steel and two European ODS Eurofer 97 steels. *Fusion Engineering and Design*, 2005, vol. 75–79, p. 1037–1041.

[23] FERNANDEZ, P.; et al. Creep strength of reduced activation ferritic/martensitic steel Eurofer 97. *Fusion Engineering and Design*, 2005, vol. 75–79, p. 1003–1008.

[24] SCHAEUBLIN, R.; et al. Microstructure and mechanical properties of two ODS ferritic/martensitic steels. *Journal of Nuclear Materials*, 2002, vol. 307–311, p. 778–782.

[25] LINDAU, R.; et al. Mechanical and microstructural properties of a hipped RAFM ODS–steel. *Journal of Nuclear Materials*, 2002, vol. 307–311, p. 769–772.

[26] UKAI, S.; OHTSUKA, S. Low cycle fatigue properties of ODS ferritic–martensitic steels at high temperatures. *Journal of Nuclear Materials*, 2007, vol. 367–370, p. 234–238.

[27] KLESNIL, M.; LUKAS, P. *Fatigue of metallic materials.* Amsterdam: Elsevier, 1992. 270 p.

[28] OKSIUTA, Z.; et al. Development and characterisation of a new ODS ferritic steel for fusion reactor aplications. *Journal of Nuclear Materials*, 2009, vol. 393, s. 114–119.

[29] McCLINTOCK, D.; et al. Mechanical properties of irradiated ODS–Eurofer and nanocluster strengthened 14YWT. *Journal of Nuclear Materials*, 2009, vol. 392, p. 353–359.

[30] STECKMEYER, A.; et al. Tensile properties and deformation mechanisms of 14Cr ODS ferritic steel. *Journal of Nuclear Materials*, 2010, vol. 405, p. 95–100.

[31] LÄSNER, R.; et al. Structural materials for DEMO: The EU development, strategy, testing and modelling. *Fusion Engineering and Design*, 2007, vol. 82, p. 511–520.

[32] KAUFMAN, M.; NEU, R. Tungsten as first wall material in fusion devices. *Fusion Engineering and Design*, 2007, vol. 82, p. 521–527.

[33] TAYLOR, N. P.; PAMPIN, R. Activation properties of tungsten as a first wall protection in fusion power plants. *Fusion Engineering and Design*, 2006, vol. 81, p. 1333–1338.

[34] RICCARDI, B.; et al. Characterisation of commercial grade Tyranno SA/CVI-SiC composites. *Journal of Nuclear Materials*, 2007, vol. 367–370, p. 672–676.

[35] POLÁK, J. *Cyclic plasticity and low cycle fatigue life of metal.* Prague: Academia, 1991, 315 s.

[36] POLÁK, J. *Cyclic deformation, crack initiation and low-cycle fatigue.* Oxford: Elsevier, 2003, 39 s.

[37] MUGHRABI, H. The cyclic hardening and saturation behaviour of copper single crystal. *Materials Science and Engineering*, 1978, vol. 3, p. 207–223.

[38] MAN, J. Extrusion and intrusions in fatigued metals. Part 2. AMF and EBSD study of early growth of extrusion and intrusion in 316L steel fatigued at room temperature. *Philosophical Magazine*, 2009, vol. 89, p. 1337–1372.

[39] MAN, J. Study of surface relief evolution in fatigued 316L austenitic stainless steel by AFM. *Materials Science and Engineering A*, 2003, vol. 351, p. 123–132.

[40] CAILLARD, D.; MARTIN, J. *Thermally activated mechanisms in crystal plasticity.* Pergamon Materials Series vol. 8, Elsevier, Oxford, 2003.

[41] MILICKA, K. Creep behaviour of long range ordered Cu50Zn alloy. *Acta Materialia*, 1999, vol. 47, p. 1831–1843.

[42] BLUM, W.; et al. Two mechanisms of dislocation motion during creep. *Acta Materialia*, 1989, vol. 37, p. 2439–2453.

[43] KRUML, T.; et al. Stress reduction experiments during constant–strain–rate tests in Cu and Ge. *Philosophical Magazine Letters*, 2003, vol. 83, p. 651–658.

[44] MUGHRABI, H. Dislocation wall and cell structures and long-range internal stresses in deformed metal crystals. *Acta Metallurgica*, 1983, vol. 31, p. 1367–1379.

[45] SAADA, G.; KRUML, T. Removal of plastic instabilities by reversal of the applied stress. *Philosophical Magazine*, 2012, , in press.

[46] POLAK, J.; FARDOUN, F.; DEGALLAIX, S. Analysis of the hysteresis loop in stainless steels II. Austeniticferritic duplex steel and the effect of nitrogen. *Materials Science and Engineering: A*, 2001, vol. 297, p. 154–161.

[47] EWING, J. A.; HUMFREY, J. C. W. The fracture of metals under repeated alternations of stress. *Phil. Trans. Roy. Soc. London A*, 1903, vol. 200, p. 241–250.

[48] SURESH, S. *Fatigue of material.* Cambridge, 1998, 680 s.

[49] ANTONOPOULOS, J. G.; BROWN, L. M.; WITNER, A. T. Vacancy dipoles in fatigued copper. *Philosophical Magazine*, 1976, vol. 34, p. 549–563.

[50] ZHAI, T.; MARTIN, J. W.; BRIGSS, G. A. D. Fatigue damage in aluminum single crystalsI. On the surface containing the slip burgers vector. *Acta Metallurgica Materialia*, 1995, vol. 43, p. 3813–3825.

[51] ESSMANN, U.; GÖSSELE, U.; MUGHRABI, H. A model of extrusion and intrusion in fatigued metals: I. Point defect production and growth of extrusion. *Philosophical Magazine*, 1981, vol. 44, p. 405–426.

[52] LIN, T. H.; LIN, S. R. Micromechanical theory of fatigue crack initiation applied to timedependent fatigue in *Fatigue mechanisms, Philadelphia, 1979, p. 707.*

[53] WITMER, D. E.; FARRINGTON, G. C.; LAIRD, C. Changes in strain localization behavior induced by fatigue in inert environments. *Acta Mettalurgica*, 1978, vol. 35, p. 1895–1909.

[54] POLÁK, J. *Damage accumulation and fatigue life of materials.* BRNO, 1998. Inaugural presentation, FSI VUT Brno.

[55] KRUML, T.; POLÁK, J. Fatigue cracks in Eurofer 97 steel: Part I. Nucleation and small crack growth kinetics. *Journal of Nuclear Materials*, 2011, vol. 412, p. 2–6.

[56] OBRTLÍK, K.; et al. Short fatigue crack behaviour in 316L stainless steel. *International Journal of Fatigue*, 1997, vol. 19, p. 471–475.

[57] OKSIUTA, Z.; et al. Effect of thermo–mechanical treatments on the microstructure and mechanical properties of an ODS ferritic steel. *Journal of Nuclear Materials*, 2011, vol. 412, p. 221–226.

[58] MÖSLANG, A. Development of creep fatigue specimen and related test technology. in *IFMIF User Meeting, Tokyo, 2000.*

[59] HIROSE, T.; et al. Effect of specimen size on fatigue properties of reducedactivation ferritic/martensitic steels. *Journal of Nuclear Material*, 2000, vol. 283–287, p. 1018–1022.

[60] AKTAA, J.; SCHMITT, R. High temperature deformation and damage behavior of RAFM steels under low cycle fatigue loading: Experiments and modeling. *Fusion Engineering and Design*, 2006, vol. 81, p. 2221–2231.

[61] BASQIN, O. H. The exponential law of endurance tests. *Proceedings of the American Society for Testing and Materials*, 1910, vol. 10, p. 625–630.

[62] COFFIN, L. F. A study of the effects of cyclic thermal stresses on a ductile metal. *Trans. ASME*, 1954, vol. 76, p. 931–950.

[63] MANSON, S. S. Behaviour of materials under conditions of thermal stress in *Heat Transfers Symposium, University Michigan, 1953, p. 9-75.*

[64] GANNUZZI, L.; STEVIE, F. A review of focused ion beam milling techniques for TEM specimen preparation. *Micron*, 1999, vol. 30, p. 197–204.

[65] LI, J.; MALIS, T.; DIONNE, S. Recent advances in FIBTEM specimen preparation techniques. *Materials Characterization*, 2006, vol. 57, p. 64–70.

[66] CLANCY, M.; POMEROY, M. J.; BELOCHAPKINE, S. Improved FIB milling process for TEM preparation of NiAlPt bulk alloy samples containing residual stress. *Micron*, 2012, vol. 43, p. 627–630.

[67] KUBIS, A.; et al. Focused Ion-beam tomography. *Metallurgical and Materials Transactions*, 2004, vol. 35A, p. 1935–1943.

[68] HOLZAPFEL, C.; et al. Interaction of crack with precipitates and grain boundaries: Understanding crack growth mechanisms through focused ion beam tomography. *Scripta Materialia*, 2007, vol. 56, p. 697–700.

[69] MARX, M.; et al. Interaction of microcracks with selected interfacec: Focused ion beam for systematic crack initiation. *Materials Science and Engineering A*, 2006, vol. 435–436, p. 595–601

[70] MAN, J.; et al. Study of cyclic strain localization and fatigue crack initiation using FIB technique. *International Journal of Fatigue*, 2012, vol. 39, p. 44–53.

[71] POLÁK, J. Mechanisms and kinetics of the early fatigue damage in crystalline materials. *Materials Science and Engineering: A*, 2007, vol. 468–470, p. 33–39.

[72] JISA, D.; et al. Small fatigue crack growth in aluminium alloy EN-AW 6082/T6. *International Journal of Fatigue*, 2010, vol. 32, p. 1913–1920.

[73] POLÁK, J.; ZEZULKA, P. Short crack growth and fatigue life in austenitic-ferritic duplex stainless steel. *Fatigue and Fracture of Engineering Materialsand Structures*, 2005, vol. 28, p. 923–935.

[74] HIRTH, J. P.; LOHTE, J. *Theory of Dislocations* Wiley, New York, 1982,

[75] OROWAN, E. Discussion on Internal Stresses in *Symp. Internal Stresses in Metals and Alloys, London, The Institute of Metals, p. 451–453.*

[76] ARZT, E.; WILKINSON, D. Threshold stresses for dislocation climb over hard particles: The effect of an attractive interaction. *Acta Metallurgica*, 1986, vol. 34, p. 1893–1898.

[77] ARZT, E.; ROSLER, J. The kinetics of dislocation climb over hard particles – II. Effects of an attractive particle–dislocation interaction. *Acta Metallurgica*, 1988, vol. 36, p. 1053–1060.

[78] ROSLER, J.; ARZT, E. The kinetics of dislocation climb over hard particles–I. Climb without attractive particle – dislocation interaction. *Acta Metallurgica*, 1988, vol. 36, p. 1043–1051.

[79] TAKAHASHI, A.; et al. Atomistic-continuum modeling of dislocation interaction with Y_2O_3 particles in iron. *Journal of Nuclear Materials*, 2011, vol. 417, p. 1098 – 1101.

[80] CLATTERBUCK, D.; CHRZAN, D.; MORRIS, J. The ideal strength of iron in tension and shear. *Acta Materialia*, 2003, vol. 51, p. 2271–2283

[81] OGATA, S.; et al. Ab initio study of ideal shear strength. *Physical Review B*, 2004, vol. 70, p. 1041104.

[82] PAUL, A.; et al. Microstructural characterization of Eurofer-ODS RAFM steel in the normalized and tempered condition and after thermal aging in simulated fusion conditions. *Fusion Engineering and Design*, 2005, vol. 75–79, p. 1061–1065.

[83] MALAPLATE, J.; et al. Creep behavior of ODS materials: A study of dislocations/precipitates interactions. *Journal of Nuclear Material*, 2011, vol. 417, p. 205–208.

[84] SAKASEGAWA, H.; et al. Evaluation of threshold stress of the MA957 ODS ferrtic alloy. *Journal of Nuclear Material*, 2009, vol. 386–688, p. 511–514.

[85] REPPICH, B. On the attractive particle – dislocation interaction in dispersion – strengthened material. *Acta Materialia*, 1998, vol. 46, p. 61–67.

[86] SAAD, A.; et al. Cyclic softening behaviour of a P91 steel under low cycle fatigue at high temperature. *Procedia Engineering*, 2011, vol. 10, p. 1103–1108.

[87] CHABOCHE, J.; ROUSSELIER, G. On the Plastic and Viscoplastic Constitutive Equations – Part 1: Rules Developed With Internal Variable Concept. *Journal of Pressure Vessel Technology*, 1983, vol. 105, p. 153–159.

[88] GIROUX, P.; et al. Influence of strain rate on P92 microstructural stability during fatigue tests at high temperature. *Procedia Engineering*, 2010, vol. 2, p. 2141–2150

[89] FOURNIER, B.; et al. Creepfatigueoxidation interactions in a 9Cr1Mo martensitic steel. PartI: Effect of tensile holding period on fatigue lifetime. *International Journal of Fatigue*, 2008, vol. 30, p. 649–662.

[90] PARK, J. S.; KIM, S.; LEE, C. S. Effect of W addition on the low cycle fatigue behavior of high Cr ferritic steels. *Materials Science and Engineering: A*, 2001, vol. 298, p. 127–136.

[91] NAGESHA, A.; et al. Isothermal and thermomechanical fatigue studies on a modified 9Cr1Mo ferritic martensitic steel. *Materials Science and Engineering: A*, 2012, vol. 554, p. 95–104

[92] FOURNIER, B.; et al. Comparison of various 912 % Cr steels under fatigue and creep–fatigue loadings at high temperature. *Materials Science and Engineering: A*, 2011, vol. 528, p. 6943–6945.

[93] POLAK, J.; HELESIC, J.; OBRTLIK, K. Nucleation stress for persistent slip bands in fatigued copper single crystals. *Materials Science and Engineering: A*, 1988, vol. 101, p. 7–12.

[94] POLAK, J.; KLESNIL, M. The Hysteresis Loop 1. A Statistical Theory. *Fatigue Engineering Material Structure*, 1982, vol. 5, p. 19–32

[95] POLAK, J.; FARDOUN, F.; DEGALLAIX, S. Effective and internal stresses in cyclic straining of 316 stainless steel. *Materials Science and Engineering: A*, 1998, vol. 215, p. 104–112.

[96] POLAK, J.; PETRENEC, M.; DEGALLAIX, S. On the analysis of the hysteresis loop of ferritic steel in cyclic straining. *Scripta Materialia*, 2002, vol. 47, p. 731–739.

[97] GIORDANA, M.; et al. Microstructure evolution during cyclic tests on EUROFER 97 at room temperature. TEM observation and modelling. *Materials Science and Engineering A*, 2012, vol. 550, p. 103–111.

[98] OKSIUTA, Z.; BALUC, N. Microstructure and Charpy impact properties of 12–14Cr oxide dispersion–strengthened ferritic steels. *Journal of Nuclear Materials*, 2008, vol. 374, p. 178–184.

[99] LUKÁS, P.; Kunz, L.; KREJCI, J. Dislocation and P.S.B.s in copper single crystals fatigued at low strain amplitude. *Physica Status Solidi*, 1968, vol. 27, p. 545–558.

[100] HOLSTE, C. Cyclic plasticity of nickel, from single crystals to submicrocrystalline polycrystals. *Philosophical Magazine*, 2004, vol. 84, p. 299–315.

[101] PETRENEC, M.; et al. Dislocation structures in cyclically strained X10CrAl24 ferritic steel. *Acta Materialia*, 2006, vol. 54, p. 3429–3443.

[102] MAN, J.; et al. AFM and TEM study of cyclic slip localization in fatigued ferritic X10CrAl24 stainless steel. *Acta Materialia*, 2004, vol. 52, p. 5551–5561.

[103] THIELE, E.; HOLSTE, C.; KLEMM, R. Influence of size effect on microstructural changes in cyclically deformed polycrystalline nickel. *Zeitschrift Fur Metallkunde*, 2002, vol. 730–736, p. 730–736.

[104] KRUML, T.; et al. Dislocation structures in the bands of localised cyclic plastic strain in austenitic 316L and austenitic–ferritic duplex stainless steels. *Acta Materialia*, 1997, vol. 45, p. 5145–5151.

[105] DEGALLAIX, S.; et al. Fatigue damage in austenitic–ferritic duplex stainless steels. *Fatigue and Fracture of Engineering Materialsand Structures*, 1995, vol. 18, p. 65–77.

[106] LUKAS, P.; et al. Fatigue damage of ultrafine-grain copper in very–high cycle fatigue region. *Materials Science and Engineering A*, 2011, vol. 528, p. 7036–7040.

[107] TOMKINSON, B. Fatigue crack propagation – an analysis. *Philosophical Magazine*, 1968, vol. 18, p. 1041–1066.

[108] FOURNIER, B.; et al. Creep–fatigue–oxidation interactions in a 9Cr-1Mo martensitic steel. Part III. Lifetime prediction. *International Journal of Fatigue*, 2008, vol. 30, p. 1797–1812.

[109] BROECK, D. *The practical use of fracture mechanics*. Springer, 1989.

[110] PARIS, P. C.; ERDOGAN, F. Critical analysis of crack propagation laws. *Journal of Basic Engineering*, 1960, vol. 85, p. 9–14.

[111] KLESNIL, M.; LUKáS, P. Influence of strength and stress history on growth and stabilisation of fatigue cracks. *Engineering fracture Mechanics*, 1972, vol. 4, p. 77–92.

[112] LARDNER, R. W. A dislocation model for fatigue crack growth in metals. *Philosophical Magazine*, 1968 vol. 17, p. 71–82.

[113] ANDERSON, T. L. *Fracture Mechanics – Fundamentals and Applications* CRC Press Inc, 1995.

[114] POOK, L. P. *Linear elastic fracture mechanics for engineers* WIT Press, Southampton, 2000.

[115] HUTCHINSON, W. Singular behaviour at the end of a tensile crack in hardening material. *Journal of Mechanics and Physics of Solids*, 1968, vol. 16, p. 13–kr31.

[116] RICE, J. R.; ROSENGREN, G. F. Plain strain deformation near a crack tip in power–law hardening material. *Journal of Mechanics and Physics of Solids*, 1968, vol. 16, p. 1–12.

[117] KRUML, T.; POLÁK, J. Fatigue cracks in Eurofer 97 steel: Part II. Comparison of small and long fatigue crack growth. *Journal of Nuclear Material*, 2011, vol. 412, p. 7–12.

[118] TANAKA, K.; MURA, T. A dislocation model for fatigue crack initiation. *Journal of Applied Mechanics*, 1981, vol. 48, p. 97–103.

[119] MURA, T. A theory of fatigue crack initiation. *Materials Science and Engineering A*, 1994, vol. 174, p. 61–70.

[120] ALEXANDRE, F.; DEYBER, S.; PINEAU, A. Modelling the optimum grain size on the low cycle fatigue life of a Ni based superalloy in the presence of two possible crack initiation sites. *Scripta Materialia*, 2004, vol. 50, p. 25–30.

[121] MUGHRABI, H.; HOPPEL, H. Cyclic deformation and fatigue properties of very fine–grained metals and alloys. *International Journal of Fatigue*, 2010, vol. 32, p. 1413–1427.

[122] OPPEL, H.; et al. An overview: Fatigue behaviour of ultrafine-grained metals and alloys. *International Journal of Fatigue*, 2006, vol. 28, p. 1001–1010.

List of abbreviations

A–DC	advanced dual cooling system
CEA	Commissariat à L'énergie Atomique
CFC	carbon fibre composite
CRPP	centre of research in plasma physics
D	deuterium
DBTT	ductile brittle transition temperature
dpa	displacement per atom
EBSD	electron back scattered diffraction
ECAP	equal channel angular pressing
EFDA	European Fusion Development Agreement
EMG	Essmann Gössele Mughrabi model
EPFL	École Polytechnique Fédérale de Laussane
FIB	focused ion beam
FM	ferritic–martensitic
HIP	hot isostatic pressing
HRTEM	high resolution transmission electron microscopy
HTP	high pressure torsion
IFMIF	International Fusion Materials Irradiation Facility
ISS	International Space Station
ITER	International Thermonuclear Experimental Reactor
L	Longitudinal direction
LAB	low angle boundary
LEFM	linear elastic fracture mechanics
ODS	Oxide Dispersion Strengthened
PFC	plasma face components
PSB	Persistent Slip Band
PSM	Persistent Slip Marking
PPCS	power plant conceptual study
RAF	reduce activation ferritic steel
RAFM	Reduced Activation Ferritic/martensitic steel
RT	room temperature
SEM	scanning electron microscopy
SOL	scrape of layer
SPD	severe plastic deformation
T	tritium
TBM	Test Blanket Modules
TCWS	tokamak cooling water system
TEM	transmission electron microscopy
TOKAMAK	Toroidalnaja Kamera i Magnitnyje Katuški
UFG	ultra fine grain

List of symbols

a crack length
a_i fictive crack length
b fatigue strength exponent
b Burges vector
c fatigue ductility exponent
d, D grain size
f_w volume walls in the PSB
h_e height of the static extrusion
k relaxation factor
k_g crack growth coefficient
m exponent in Paris–Erdogan law
n free neutron
n'_b fatigue hardening exponent
p vacancy production rate
w width of PSB
x_g distance between oxide particles
A vacancy annihilation rate
C_v^{sat} saturated vacancy concentration in walls
D_v diffusivity of vacancies
E Young modulus
G shear modulus
K_i stress intensity factor
K'_b fatigue hardening coefficient
L depth of the PSB below surface
M Taylor factor
N number of cycles
N_i number of cycles necessary to initiate a crack
N_{cg} number of cycles necessary to grow a crack to its critical length
N_F number of cycles to failure
P Larson-Miller parameter
Q performance of fusion
R_y plastic zone size at the crack tip
Sv Sieverts
$\overline{T}$ parameter in Tomkins law
V_H parameter of hysteresis loop shape
W area of hysteresis loop

α	coefficient in Orowan and Tanaka and Mura law
γ	surface energy
ε_a	total strain amplitude
ε_{ap}	plastic strain amplitude
ε'_f	fatigue ductility coefficient
ρ	dislocation density
σ_a	stress amplitude
σ'_f	fatigue strength coefficient
ΔK	stress intensity factor range
$\Delta \mathrm{K}_{th}$	threshold of stress intensity factor range
$\Delta \varepsilon_{ap}$	plastic strain range
$\Delta \sigma$	stress range